Three papers on electromagnetics:

Development of Wirelessly Controlled and Powered Space-Fed Phased Array Antenna, Temperature Rise in Objects Due to Optical Focused Beam Through Atmospheric Turbulence Near Ground and Ocean Surface, and A Steerable 60GHz Array Antenna Using a Continuously Variable Dielectric Phase Shifter

Matthew Stoneback

A dissertation submitted in partial fulfillment of the requirements for the degree of

Doctor of Philosophy

University of Washington

2013

Reading Committee:

Yasuo Kuga, Chair

Akira Ishimaru

Jacques Chris Rudell

Program Authorized to Offer Degree:

Electrical Engineering

University of Washington

Abstract

Three papers on electromagnetics:

Development of Wirelessly Controlled and Powered Space-Fed Phased Array Antenna, Temperature Rise in Objects Due to Optical Focused Beam Through Atmospheric Turbulence Near Ground and Ocean Surface, and A Steerable 60GHz Array Antenna Using a Continuously Variable Dielectric Phase Shifter.

Matthew Stoneback

Chair of the Supervisory Committee:
Professor Yasuo Kuga
Department of Electrical Engineering

The results of research done in three areas of electromagnetics are presented in a three part document. Part I discusses the development of a wirelessly controlled and wirelessly powered space-fed phased array antenna (WiPAA). The WiPAA is presented as a viable solution to the problem of deploying and operating large area phased array antennas in space. Chapters 1 through 7 describe the development, construction, and testing activities that were completed to this end over the course of several years. Part II is a report on the work done in developing a model for laser heating of solid objects through a turbulent medium. This work details a method for estimating the temperature rise in various types of materials due to a laser beam whose intensity has been reduced to some degree by atmospheric turbulence. Chapters 8 through 12 contain the details of this work which is particularly relevant to operators of high power laser systems operating near the ground or ocean surface. Part III is a report on the development of a steerable 60GHz phased array using a continuously variable dielectric phase shifting technique. Chapters 13 through 16 contain the results of this project including measured results from a prototype dielectric phase shifter and beam steering measurements from a 60GHz phased array.

INTRODUCTION

This document is a compilation of publishable work done in three areas of electromagnetics. Part I is a full report on the work done in developing a wirelessly controlled and wirelessly powered space-fed phased array antenna (WiPAA). In recent years there has been renewed interest in large apertures for space-based applications including space-based radar systems and for microwave transmission from solar power satellites. The aim of the WiPAA project is to present a viable solution to the problem of deploying and operating large area phased array antennas in space. Chapter 1 presents a case for the use of lightweight foldable antennas for space-based arrays and introduces the concept of the WiPAA. Chapter 2 outlines the basic requirements imposed on the WiPAA development which are intended to model real-world performance criteria for a typical space-based array system. Chapters 3 and 4 describe component technologies well-suited for the construction of a WiPAA system. Through detailed simulation and prototyping, an X-Band unit-cell with C-Band wireless power and control is developed. Chapters 5 and 6 present the design, fabrication, and testing results for WiPAA hardware prototypes which were constructed to explore the fabrication and operation of a functioning WiPAA system. Chapter 7 provides a summary of the project and guidance towards future activities to improve the WiPAA technology.

Part II is a report on the work done developing a model for laser heating of solid objects through a turbulent medium. This work details a method for estimating the temperature rise in various types of materials due to a laser beam whose intensity has been reduced to some degree by atmospheric turbulence. Chapter 8 explains the motivation for the project and describes some of the previous work done in the area of laser propagation and heating. The unique problem of focused beam propagation near the ground or ocean surface is described and the reasons for the

development of a new model are explained. Chapter 9 contains the mathematical description of a focused laser beam through turbulence as well as a brief discussion of the possibility of non-linear effects from thermal blooming. Chapter 10 describes how laser energy is transferred into solid objects via absorption and how the resulting heat diffuses through objects subjected to various time/thickness dependent boundary conditions. Using the formulations in Chapters 9 and 10 we constructed a computational code to model the net heating caused by a laser beam through turbulence incident on a solid object target. Chapter 11 presents numerical examples for 4 different solid targets: solid water, copper, polyimide, and glass fiber reinforced polymer. For each case the minimum laser dwell time required to reach the melting point or boiling point is computed for a range of laser transmit powers.

Part III is a report on the development of a steerable 60GHz phased array using a continuously variable dielectric phase shifting technique. The motivation for a low cost 60GHz steerable array is established through a review of technologies for 60GHz communication. Chapter 14 provides the theory of dielectric slab phase shifting using a transmission line model of the structure. The dielectric slab phase shifting technique is applied to a 60GHz transmission line and slabs of various materials and lengths are tested for phase delay and insertion loss characteristics. The results of the slab tests are used to construct a prototype phased array to demonstrate beam steering with the use of dielectric slabs. Chapter 15 describes the design of a 3x8 60GHz array and the use of dielectric slabs to obtain beam steering. Chapter 16 summarizes the results of the project and ideas for constructing a fieldable 60GHz array using dielectric slab phase shifters are presented.

TABLE OF CONTENTS

Part I. Development of Wirelessly Controlled and Powered Space-Fed Phased Array Antenna

Chapter 1: INTRODUCTION

1.1. Large array antennas in space

Phased array antennas are a critical component in many radar and communications systems. The increased collector area and directivity of a large area phased array antenna is particularly attractive to long range or high sensitivity applications. Space-based radar antenna systems, for example, typically require a large total aperture area to achieve the directivity needed to provide accurate target location information. The TechSat 21 experiment put forward by the Air Force Research Laboratory (AFRL) was premised on the idea that a number of autonomous antennas operating as one could provide a large "virtual aperture" and be useful for interferometric imaging, geolocation, and ground moving target indication (GMTI) [1]. A 2005 investigation identified apertures in the range of $40 - 100m^2$ as the minimum required to achieve desirable performance for an x-band space-based radar antenna [2].

Another application for large area RF apertures in space is in the transmission and focusing of space solar power to locations on the Earth's surface. Since at least the 1970's the idea of conveying harvested solar power from space to the Earth with a microwave link has been considered [3]. An early report describes a notional reference –system antenna comprised of 7220 subarrays, each $10x10m$ generating and transmitting a total of 5 GW of power to the Earth [4]. In 1981 the congressional Office of Technology Assessment (OTA) produced a report on the merits and feasibility of Solar Power Satellites (SPS) [5]. Included in the OTA report was a discussion of a reference system for microwave transmission of power from an SPS to a ground-

based rectifying antenna array. Work in the 1980's by W. C. Brown explored the idea of using space-based arrays of rectennas on a roll-up flexible material for the deployment of apertures of up to $50{,}000m^2$ [6]. The 1994 PowerSat report estimates a rectangular array $32x18m$ would be sufficient to overcome propagation losses and achieve efficient power transfer from a satellite-based power station producing 102kW [7]. The PowerSat project identified a phased array antenna construction technique that made use of inflatable technology to provide a lightweight, compactable, and easily deployable structure. A more recent report by NASA describes an array of 33,000 $16.5\ m$ dishes forming a large $3\ km$ diameter space-based transmitter for solar energy [8]. All of these designs have in common the technical challenge of transporting and deploying structures with large total surface area with launch vehicles that are volume, diameter, and payload limited cylinders.

1.2. Low mass density and foldable antennas

Space-based array antennas are generally large, especially if the frequency of operation is at X-Band or below. The increased array size provides the benefit of enhanced directivity and larger total power output however as the array size increases the weight and complexity of such a structure becomes a limiting factor. The MIT study projected a mass of 700-1500 kg (17.5 – 37.5 kg/m^2) for a 40m^2 X-Band aperture [2]. This projection was based on an assumption that an array is constructed using discrete transmit/receive (TR) modules assembled in 'brick' fashion. If a 'tile' architecture is used the expected mass of a 40m^2 array is 500-700 kg (12.5 – 17.5 kg/m^2). Although the utility of these phased array construction techniques has been proven, such antennas have limited application in very large (>100m^2) space-based communications or remote sensing systems. The inherent rigidity of 'brick' or 'tile' phased array apertures hinders their deployment in space-based systems. A 1991 article from the Rockwell Corporation describes a

unique "venetian blind" array which is compact enough to stow in an Atlas-Centaur payload faring but deploys to form a $23.5\ m$ diameter space-fed lens [9]. More recent efforts to develop large-area high-altitude phased array antennas have suggested that significant reduction in aperture mass density is possible. DARPA's ISIS program demonstrated a large X-Band aperture with a mass density of 2 kg/m^2 using a unique printed-paper antenna element [10].

1.3. Space-fed arrays

A 2003 study considering radar technology suitable for medium Earth orbit (MEO) (~10,000km) operation suggests that large space-fed arrays are a viable solution [11]. Space-feeding is a well-known technique to reduce the cost and complexity of large array systems [12]. Whereas an active phased array antenna has a full T/R module at each unit cell, a space-fed phased array acts as a passive lens and requires only a phase shifter at each unit cell. This is a technique first described by Miccioli in [13] and previously demonstrated in [14, 15]. As the patent by Miccioli describes, the array is fed with a smaller antenna at some distance from the array surface. The divergent nature of the transmitted beam is corrected by the phase shifters between feed side and space side of the array. The collimated and steered beam is propagated along some direction, dictated by the inputs to the phase shifters, shown in Figure 1.1, as coming from some generic device called a 'programmer.'

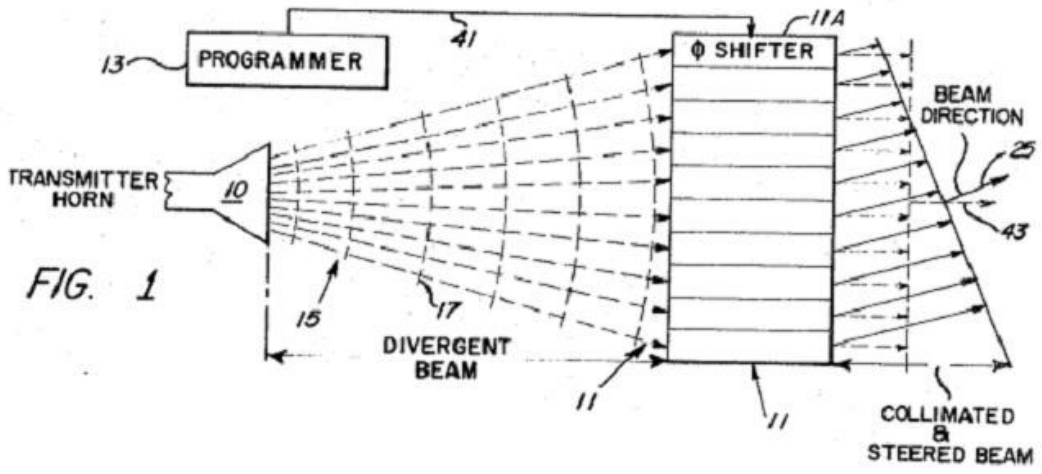

Figure 1.1: Conceptual space-fed array diagram [13].

1.4. Wireless phased array antenna concept

The challenge of putting large area phased array antennas in space has motivated this research effort and to demonstrate a potential solution to this problem we have developed a wireless space-fed phased array antenna (WiPAA).

The WiPAA is a patented concept developed by Boeing's Advanced Network and Space Systems (ANSS) describing "a system configured for radar or communications applications, comprising: a wireless, space-fed, phased array of antennas…" [16]. An overview of an example WiPAA system level block diagram is shown in Figure 1.2.

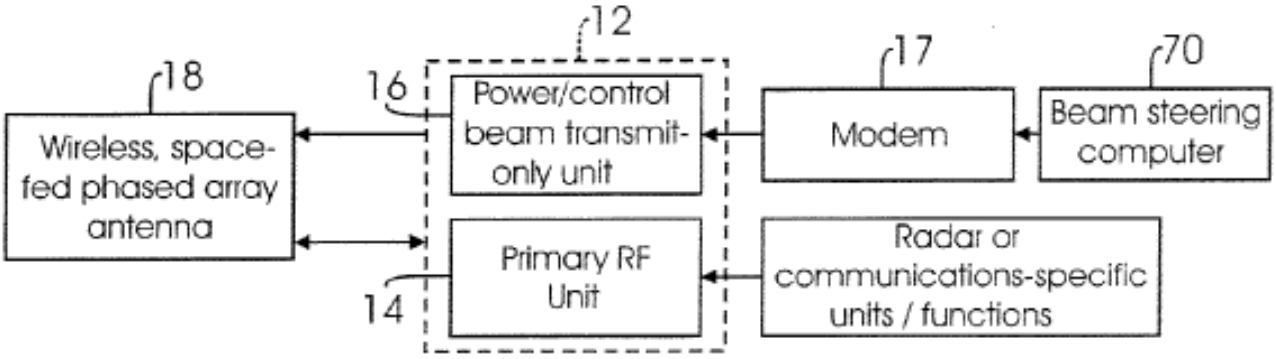

Figure 1.2: Block diagram of wireless space-fed phased array system [16].

In the patent by Sego, the wireless nature of the space-fed array concept is extended to the 'programmer'. Both the digital command for element-wise phasing, and the power needed to interpret and implement phase commands is propagated to the array elements wirelessly. The result is a phased array antenna free of wired power or control busses and without the constraints, both in rigidity and in mass density, of fixed analog power combining/dividing networks.

1.5. Scope of dissertation work

Many of today's state-of-the-art phased array antenna systems are structurally rigid due to the presence of a common distribution manifolds for power, control signals, and RF signals [17] [18] [19]. Some of the most innovative large area phased array antenna concepts have eliminated distribution manifolds for RF signals by utilizing space-fed radiating elements and have focused on structurally-integrated antenna designs the will bend, flex, and maintain rigidity as and when needed [9] [10]. In this work I will demonstrate a unique solution to the problem of creating large, compactable, phased array antennas that focuses on eliminating the distribution manifolds for power, control, and RF signals all together.

Chapter 2 will discuss the requirements I have imposed on the example WiPAA system to bound the problem to a finite endeavor while demonstrating the important and relevant technical merits of this novel approach. Section 2.1 describes how required RF performance of the PAA system simulates the aperture demands of common radar applications and the choice of primary RF frequency represents a trade between applications in remote sensing and applications for microwave power transmission from space power satellites. Section 2.2 establishes the desired functionality of a wireless link to convey power and control signals to the elements in a WiPAA antenna system. Section 2.3 provides rationale for implementation of the WiPAA concept through a discussion of the mechanical features of the array. Section 2.4 provides guidance for the choice of materials in space-based WiPAA systems with a focus proven RF materials for space applications.

Chapter 3 reports on the selection of and design of an RF radiator for use with the demonstrative WiPAA system. Section 3.1 presents the requirements imposed on the RF radiator extrapolated from the WiPAA system requirements. Section 3.2 provides the rationale for selection of a printed patch radiator for use with the space-fed array. A modified feeding structure is discussed and simulation results are presented. Section 3.3 details how the radiator can be integrated into a larger structure and replicated into an array of elements.

Chapter 4 describes the mechanism for conveying power and command information to the array unit cells in a wireless fashion. Section 4.1 provides evidence for the use of a slot antenna operating at a complementary RF frequency (in this case C-Band) for a secondary power and command signal harvesting aperture. The implications of the secondary aperture choice on the array unit cell are discussed and simulation results of the slot antenna are presented. Section 4.2 describes the implementation of a circuit for rectifying incident RF energy to provide power to

array components and a method for using this power signal to simultaneously convey beam-steering control information to the WiPAA. Methods for efficient RF-to-DC conversion, simulation data, and measurements of prototype circuits are included.

Chapter 5 includes the detailed description of the implementation of important constituent WiPAA technology in a passive 2D X-Band aperture array. This test proves the functionality of the X-Band apertures and interconnects independent of the RF phase shifters or wireless power and control circuitry. Section 5.1 provides the details of the 2D array design including CAD drawings and assembly procedures. Section 5.2 describes the test procedures to extract the RF performance of the space-fed 2D array. Section 5.3 presents the results of the test along with analysis and a discussion of potential sources of loss in the structure.

Chapter 6 presents the implementation of the WiPAA concept in a 4-element electronically scanned prototype array. Section 6.1 covers the design of the 1D array and presents a CAD drawing showing the layout of all of the apertures and components. Section 6.2 shows the communication protocol used for controlling the array with a wireless signal. Section 6.3 describes methods for the preliminary testing of the array. Section 6.4 describes the test procedures for demonstrating beam steering and presents antenna patterns to confirm beam mobility of the WiPAA prototype.

Chapter 7 provides conclusions and a brief discussion of the remaining technical challenges in implementing WiPAA technology. Section 7.1 is an overview of the WiPAA project and focuses on the work done to mature the idea from concept to functioning prototype. Section 7.2 looks ahead to the future of WiPAA technology. The possibilities and challenges of the technology are

explored through a discussion of electronics packaging, mitigation of inter-element coupling, and the efficiency of wireless power transfer in the context of WiPAA.

Chapter 2: WIPAA SYSTEM REQUIRMENTS

Figure 2.1 shows the WiPAA space-fed array architecture. The fundamental elements of the concept including space-fed primary RF, wireless control, and RF rectification to provide power are shown. The figure also shows the independent nature of the primary RF and power /control RF signals. The following sections establish the system requirements for a specific implementation of a WiPAA in an effort to exemplify the details of the space-fed array design.

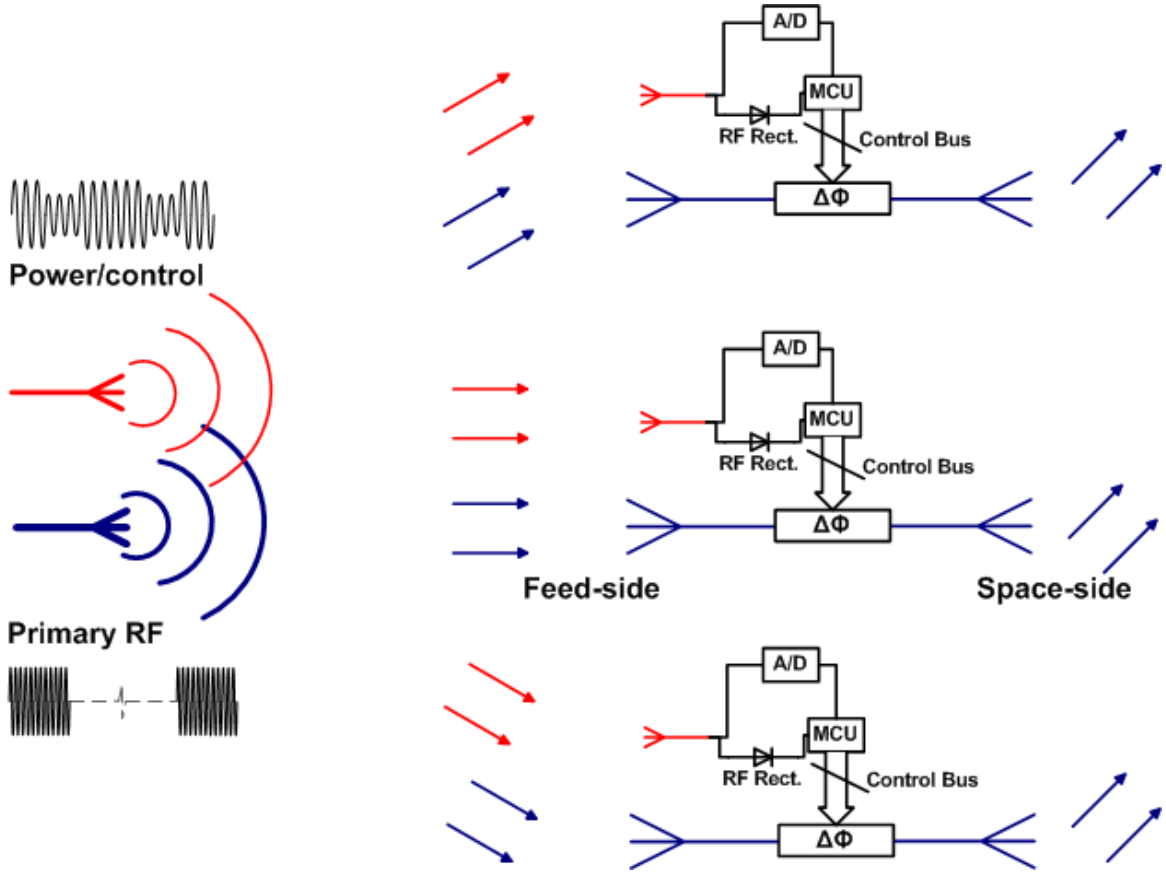

Figure 2.1: WiPAA space-fed array architecture.

2.1 RF performance of WiPAA

In principal the WiPAA design paradigm can be applied to arrays operating at any frequency. In practice, space-based arrays will encounter weight and size limitations at low frequencies and limitations in packaging and integration at high frequencies. The primary frequencies of interest for satellite antenna operators have historically been in the range of VHF to Ku-Band (130MHz to 18GHz). Because of size limitations, space-based phased arrays are most useful from about S-Band to Ku-Band (2GHz to 18GHz). Using the patented claims as a guide, the WiPAA concept has been matured via detailed simulations of compatible aperture technologies and implementation of multiple hardware prototypes. Throughout the exploratory and design phases, a few parameters are used to bound the resulting technology and maintain compatibility with notional space-based applications. Generally, the array should be: thin, lightweight, and flexible. For the prototype antenna systems we considered X-Band frequencies from 8-12GHz and Ku-Band frequencies from 12-18GHz for primary RF due to their usefulness for radar and/or communications. The Ku-Band range may have the benefit of a larger component market due to its heavy use in commercial satellite communications but the difference in required element to element spacing favored X-Band so the design of demonstrative prototypes was done at 9.5GHz. To maintain reasonable radar performance, specifically in regards to resolution, the instantaneous bandwidth target is 500MHz.

2.2 Wireless power and control of WiPAA

The WiPAA relies on a wireless signal propagated to each element of the array for both the power and control information required by the beam steering control. In this context, beam steering control includes a digital RF phase shifter with 4-bits of control and a processing unit to interpret beam steering commands and provide the voltage bias required to activate the correct

phase state in each RF phase shifter. A typical RF phase shifter draws very little current and does not contribute heavily to the DC power requirement of the unit cell. The processing unit must take in a packet of command information, for instance a scan angle, and interpret this signal based on its unique position within the array. The processing unit must provide the voltage bias required to activate the correct phase state in the phase shifter and the processing unit must continually monitor the incoming data for changes in the command information. These operations will require power and ultimately the efficiency and speed of the processing unit determines the power consumption of the unit cell.

2.3 Mechanical requirements of WiPAA

The WiPAA is unique in that it eliminates electrical connections between unit cells in the phased array. Eliminating electrical connections between the unit cells allows for the use of flexible and/or foldable materials to physically hold the array together. One major requirement imposed on a large space-based array system is that it can be transported to orbit using launch vehicles of limited storage capacity. The PowerSat study considered using a Taurus launch vehicle which has a cylindrical payload faring which is $279.4cm$ long and has a $137.2cm$ diameter [7]. In order to most efficiently use this space to transport a large area phased array aperture (eg.$10x10m$ antenna) the antenna will need to be folded or rolled.

2.4 Materials requirements of WiPAA

The antenna technologies developed for the WiPAA are planar PCB-based designs. Printed or etched structures are well suited for the construction of large-area arrays. Printed circuit boards require very little hand assembly and are relatively cheap to manufacture. In addition the cost per panel decreases significantly when producing a large volume of boards and the process is highly repeatable. Use of the X-band frequency regime requires a high-frequency PCB material. In addition the board materials must exhibit good performance in the presence of vacuum to be

useful in space-based antennas. NASA has defined outgassing specifications which limit maximum volatile condensable material (VCM) content and maximum total mass loss of polymers used in space applications to 0.1 percent and 1.0 percent respectively [20]. This guideline helps ensure that the release of VCMs does not contaminate or impede functionality of sensitive spacecraft components. Many commercial materials are available which are well suited for high-frequency space-based applications and meet the outgassing specifications established by NASA. PTFE/ceramic composite materials such RF-35TC from Taconic, RT/duroid 6002 from Rogers, or CLTE-AT from Arlon all satisfy the basic requirements for high-frequency use in space-environments [21] [22] [23]. Liquid crystal polymer (LCP) has also been shown to be useful in the fabrication of antennas and effective in high-frequency space-based applications [24] [25]. The advantage of LCP over PTFE/ceramic composite materials is that LCP can be fabricated in very thin sheets (0.05mm and 0.10mm are typical) which are strong yet flexible. LCP is very resistant to the effects of space including radiation, vacuum effects, and temperature extremes. LCP can also be processed using standard PCB etching/processing techniques making it attractive for large area circuits [26].

Chapter 3: RF RADIATOR FOR WIPAA

3.1 Constraints on radiator topology

The motivation behind developing WiPAA technology for space-based antennas is primarily to reduce the weight and rigidity of large phased array apertures. A good choice of a radiator for the WiPAA would be a radiator which is compatible with RF materials that are thin, lightweight, and flexible. Materials such as polyimides and glass/PTFE/ceramic composites are good candidates for space-based RF board materials due to their mechanical properties and their compatibility with common PCB etching processes. As the design calls for a thin, lightweight, and flexible antenna on a planar structure and the instantaneous bandwidth requirement is modest (5% at X-Band), printed patch antennas are investigated as elements for the space-fed array.

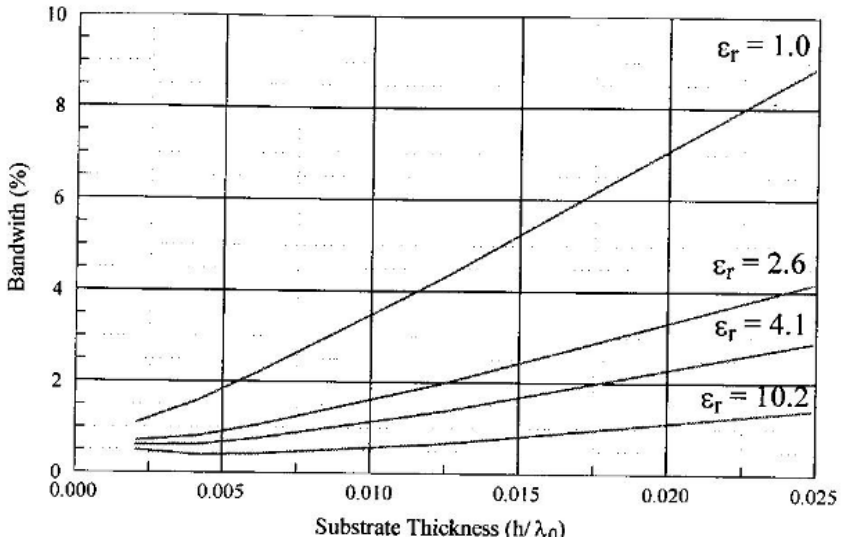

Figure 3.1: Normalized bandwidth of patch antenna vs. substrate thickness [27].

Figure 3.1 shows the normalized bandwidth for a square patch antenna as a function of substrate thickness for a range of substrate densities [27]. The curves come from an electromagnetic analysis of the patch structure using a cavity model. Based on these design curves, a standard 1.58mm (62mil) Duroid 5880 substrate is used in preliminary simulations. Figure 3.2 shows a probe fed patch antenna on a 1.58mm Duroid substrate.

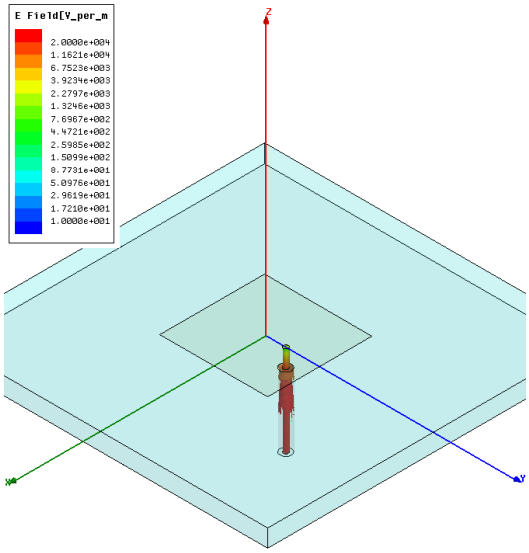

Figure 3.2: Probe-fed X-Band patch antenna on 1.58mm Duroid 5880.

The antenna dimensions are calculated using design equations in [27]. Ansoft HFSS is used to tune the antenna to the 9.5GHz center frequency. The simulated negative return loss of the probe-fed X-Band patch antenna is shown in Figure 3.3. The probe fed patch has an instantaneous bandwidth (VSWR< 2:1) of 500MHz, consistent with Figure 3.1.

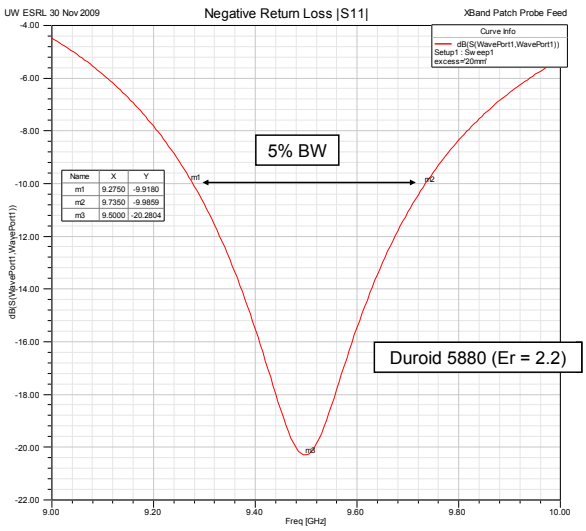

Figure 3.3: Negative return loss for probe-fed X-Band patch antenna.

Figure 3.3 shows the simulated radiation patterns over θ in primary planes (E-Plane: Φ = 90° and H-Plane: Φ = 0°). The pattern is consistent with expected microstrip directivity, though the tendency to radiate the cross-polarized mode is somewhat high. This is likely due to the square nature of the patch and the low reactance of the lowest order orthogonal resonant mode. A non-square patch should exhibit both greater bandwidth and a reduced sensitivity to cross-polarized modes.

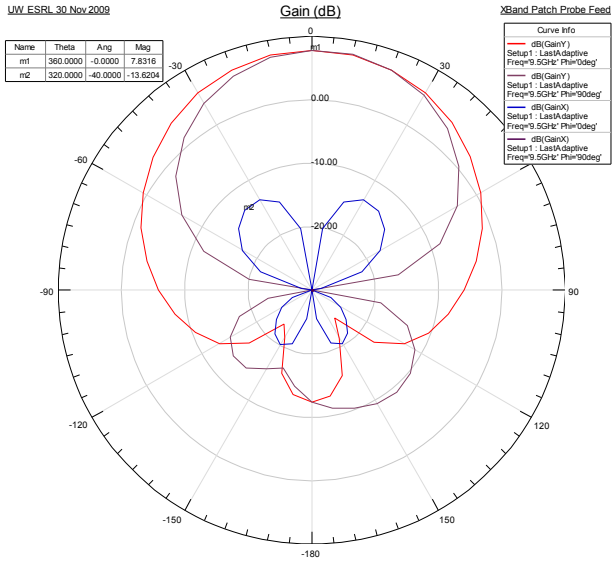

Figure 3.4: Directivity of probe-fed X-Band patch antenna in E-Plane and H-Plane.

$d_{max} = \lambda/(1+\sin\theta_{look})$

$F_{max} = 9.75GHz$:

$\Theta_{look} = 45° \rightarrow d_{max} = 18mm$

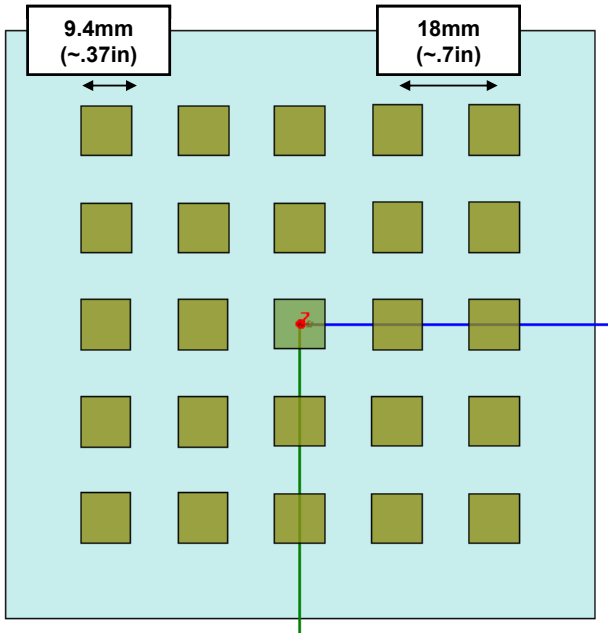

(a)

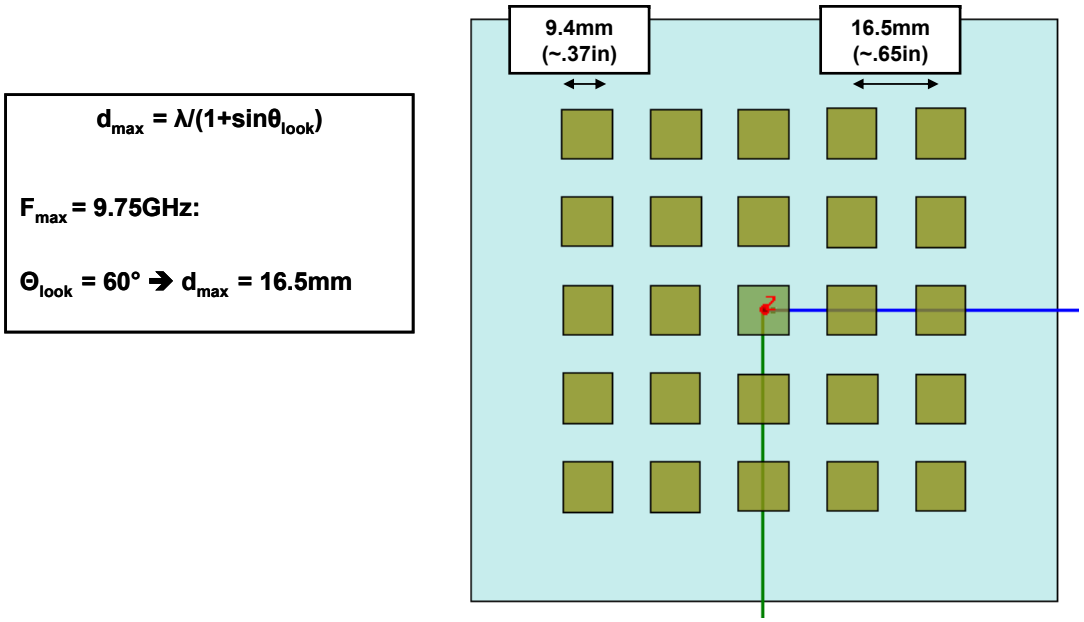

(b)

Figure 3.5: Diagram showing element spacing for 5x5 array with: (a) Max scan 45°; (b) Max scan 60°

Using the dimensions of the simulated square patch, example array configurations are generated to assess the available space for phase control, wireless receivers, and secondary apertures for wireless command and power harvesting. Using a rectangular lattice, the element to element spacing in X and Y is limited by the need to suppress grating lobes in the visible half-space ($-90° < \theta < 90°$). Figure 3.5 shows two examples of maximum array spacing corresponding to maximum look angles of 45° and 60°. The maximum element to element spacing for 45° and 60° are 18mm and 16.5mm respectively.

3.2 Proximity coupled patch radiator

In an effort to minimize the overall array thickness alternate radiator and feed geometries are investigated. The probe feed used to excite the square patch in the simulation above is useful for quickly finding good impedance match while the patch dimensions are varied but the substrate thickness could be reduced if a different feeding method is used.

History

Pozar describes, "an alternative method of obtaining enhanced bandwidth...using a microstrip feed line proximity-coupled to a patch antenna printed on a superstrate above the feed line," in a 1987 paper [28]. The key aspects of the feed geometry proposed by Pozar, including capacitively coupled open circuit feed line and parallel tuning stub, are shown in Figure 3.6.

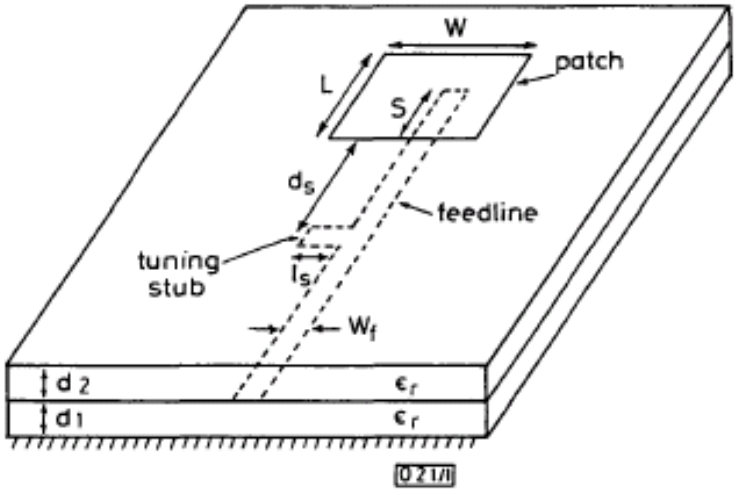

Fig. 1 *Geometry of proximity-coupled microstrip antenna*

Figure 3.6: Capacitively coupled feed proposed by Pozar [28].

Simulation results

The proximity-coupled feeding technique is implemented with a modified X-Band patch element in HFSS. The model, with feed line on .254mm substrate and patch on .762mm superstrate, is shown in Figure 3.7.

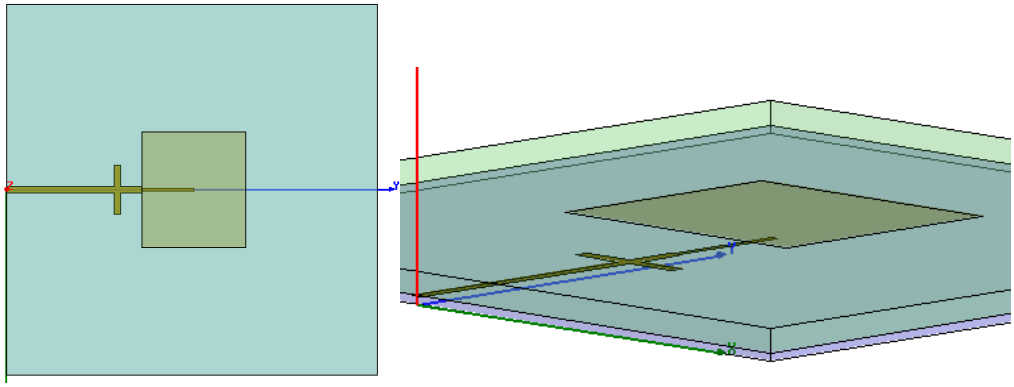

Figure 3.7: Capacitively coupled X-Band patch antenna model.

The simulated input impedance for the capacitively coupled X-Band patch is shown in Figure 3.8. The additional series capacitance due to the feed structure has caused the impedance locus to become more tightly wrapped and, as the plot in Figure 3.9 shows, the instantaneous bandwidth (VSWR< 2:1) has been improved. Based on the result of simulation, the capacitively coupled feed structure is preferable because it improves performance while reducing total thickness by more than 30%.

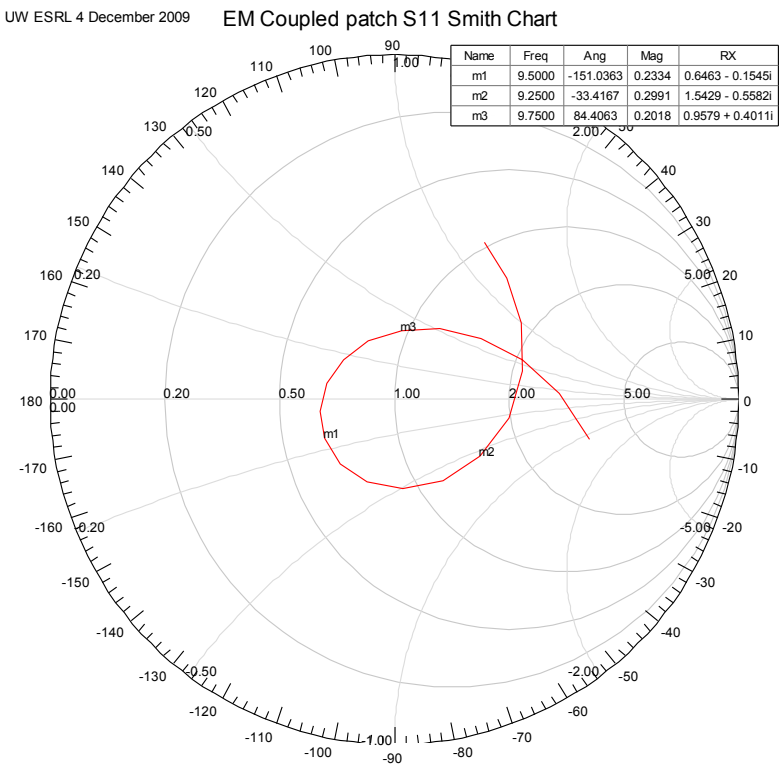

Figure 3.8: Input impedance of capacitively coupled X-Band patch antenna.

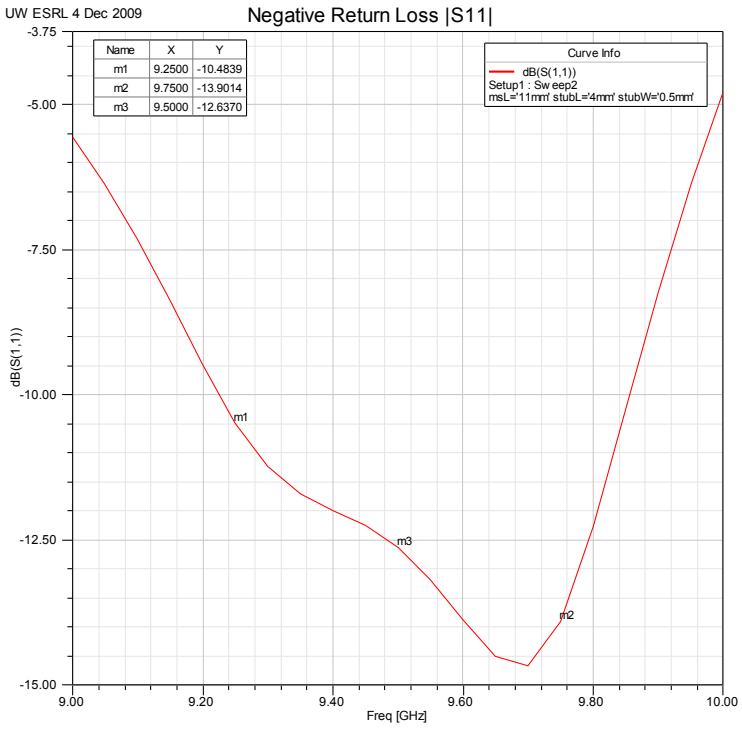

Figure 3.9: Negative return loss of capacitively coupled X-Band patch antenna.

Figure 3.10 shows the simulated directivity of capacitively coupled X-Band patch over **θ** in primary planes (E-Plane: **Φ = 90°** and H-Plane: **Φ = 0°**). Following the guidance of the original Pozar paper, a non-square patch is used and as a result the sensitivity to the cross-polarized mode is reduced compared to the probe-fed antenna shown previously.

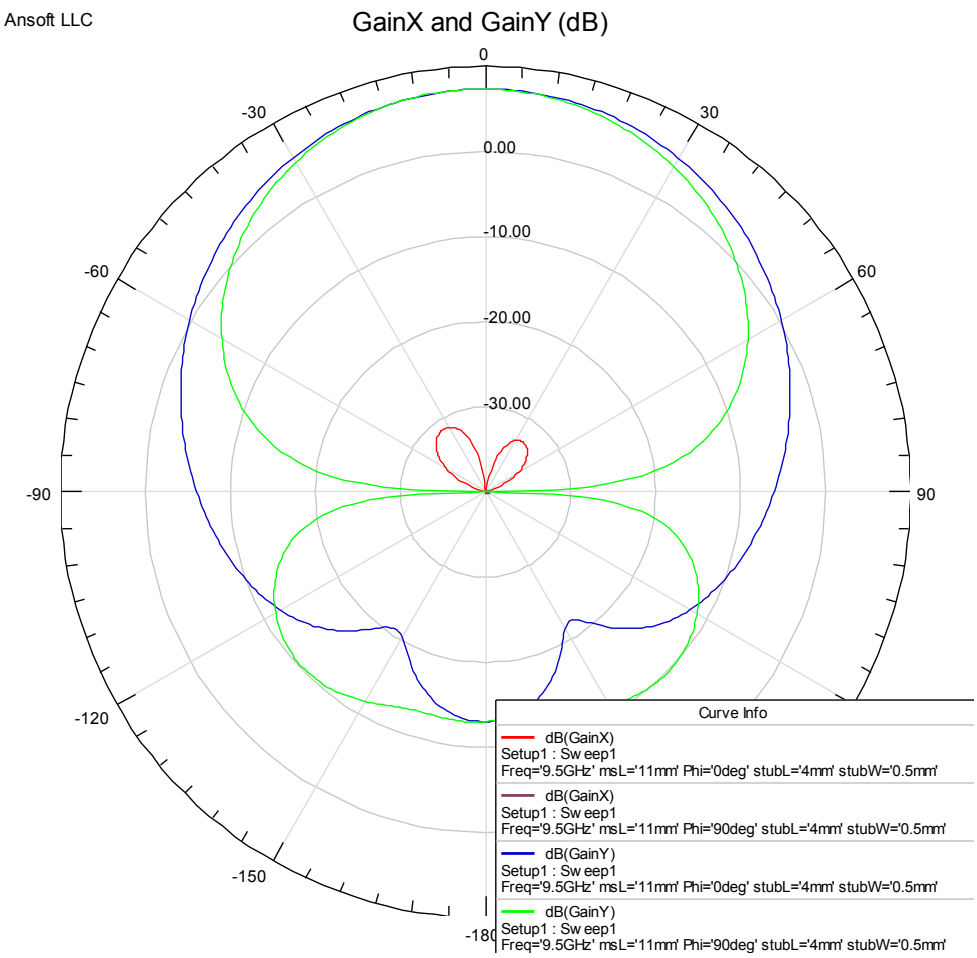

Figure 3.10: Directivity of capacitively coupled X-Band patch in E-Plane and H-Plane.

Further improvement

Improvement in antenna performance is possible with the reduced footprint feed network proposed by Duffy [29]. As shown in Figure 3.11, a split 3/4λ open circuit transformer is used instead of the 1/4λ probe and tuning stub used by Pozar.

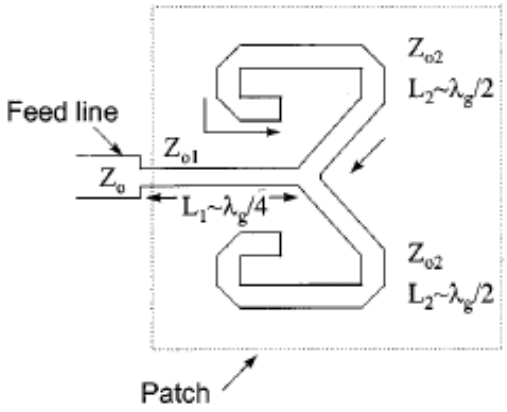

Figure 3.11: Reduced footprint feed network proposed by Duffy [29].

In the paper, Duffy shows an example using an X-Band patch on 1mm substrate ($\varepsilon_r = 2.9$). He notes three observed benefits of the technique: improved bandwidth (relative to baseline quarter wave feed) without increasing substrate height or decreasing dielectric constant, the matching network consumes no additional area beyond that occupied by the patch, and radiation is shielded by the patch and potentially conserved via re-radiation. Although bandwidth and cross-pol performance are adequate without modification, Duffy's approach could reduce the area occupied by the antenna element and matching network in an array environment where space is limited. Though shelved, the idea is kept in mind as the design of a prototype proceeds with the less complicated proximity-coupled feed.

3.3 WiPAA integration

To use the capacitively-coupled patch antenna with the WiPAA we need to consider how the antenna will be implemented in the context of a space-fed array. A space-fed array has radiating elements on two sides, one set on the feed side and one set on the space side. The microstrip line used to feed the proximity-coupled antenna above requires an interconnection to another microstrip line on the opposite side of the ground plane. An RF transition using a metalized via

to connect two 50Ω microstrip lines on opposite sides of a common ground plane is shown in Figure 3.12.

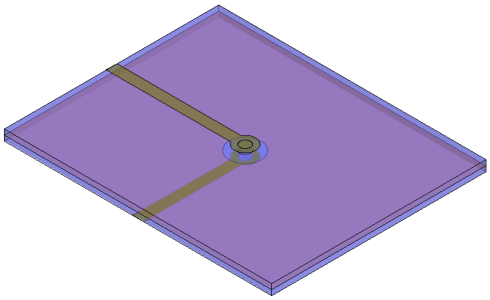

Figure 3.12: Model of feed-side to space-side RF transition.

The simulated negative return loss and negative insertion loss in Figure 3.13 shows a well matched transition, with expected loss ~.1dB.

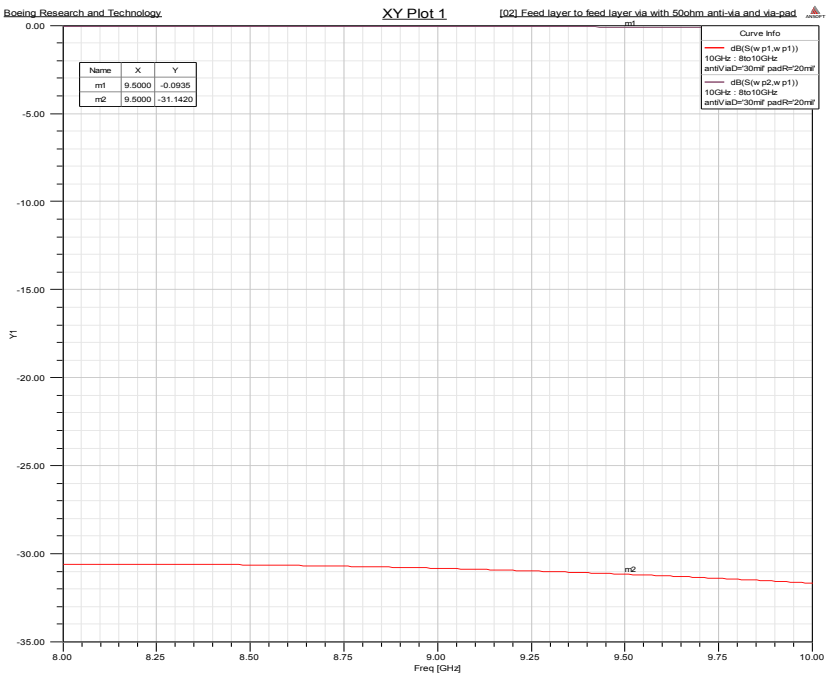

Figure 3.13: Simulated |S21| and |S11| for feed-side to space-side RF transition.

Chapter 4: WIRELESS POWER AND COMMAND SIGNAL HARVESTING

4.1 C-Band slot antenna

Compatibility with WiPAA unit cell

To achieve wireless command of element-wise phasing and wireless transfer of power to the RF modules, a second aperture operating in the ISM band at 5.8GHz is used. For many years NASA, Raython, JPL, and others have used RF in the low GHz range to transfer power wirelessly to arrays of rectifying antennas [30]. For the WiPAA system an RF signal located in the ISM band at 5.8 GHz is used. This frequency band is preferred over other ISM bands (915MHz or 2.4GHz) because apertures designed to receive 5.8GHz efficiently tend to be complimentary with the size and spacing of X-Band patch elements (i.e. a wavelength at 5.8GHz is roughly twice the wavelength at 9.5GHz). The apertures for transmitting power to the WiPAA are can be more compact at 5.8GHz than at 2.4GHz and efficient operation of rectifying components at 5.8GHz has been demonstrated [31]. Because of the relative size of C-Band antennas to X-Band antennas, a decision is made to include one C-Band antenna for every two X-Band antennas. The resulting WiPAA unit cell consists of a 1x2 array of X-Band antennas and a single C-Band antenna. Figure 4.1 shows a notional WiPAA unit cell with a $\lambda/4$ x $\lambda/4$ C-Band patch antenna.

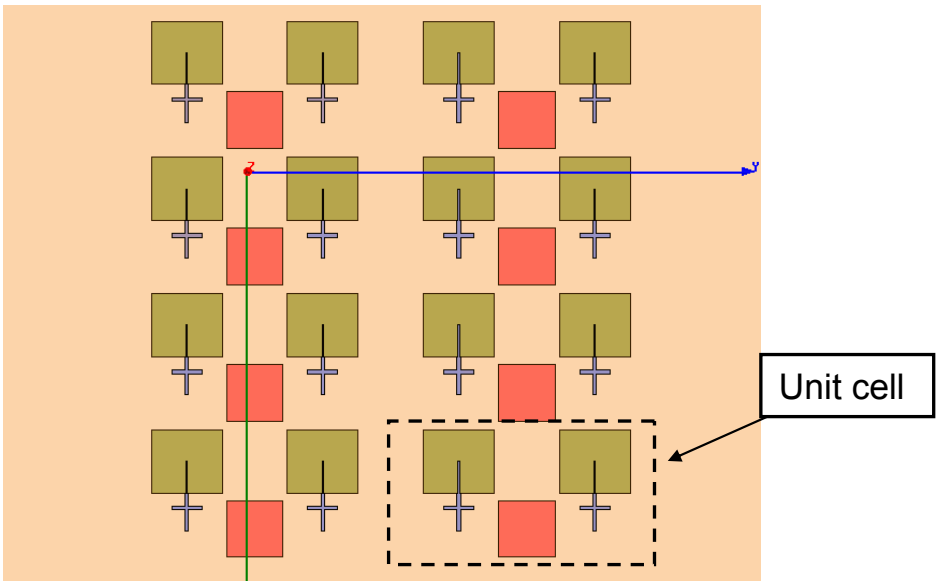

Figure 4.1: WiPAA unit cell with C-Band quarter patch antenna.

Although there are two X-Band elements per unit cell, we would like to maintain (if possible) independent phase control at each X-Band element. The area occupied by the C-Band quarter-patch leaves little useful room for a phase shifter, command/rectifying circuit, and signal distribution. As a result, an alternative antenna is investigated. Because of its compact size, a slotted ground plane under a microstrip feed line is used for the C-Band antenna [32]. Figure 4.2 shows top and side views of a microstrip fed slot antenna at C-Band. Figure 4.3 shows a microstrip fed slot antenna model used for HFSS simulation. This antenna has a longer but narrower footprint that is more suited to placement between X-Band patch elements in the array.

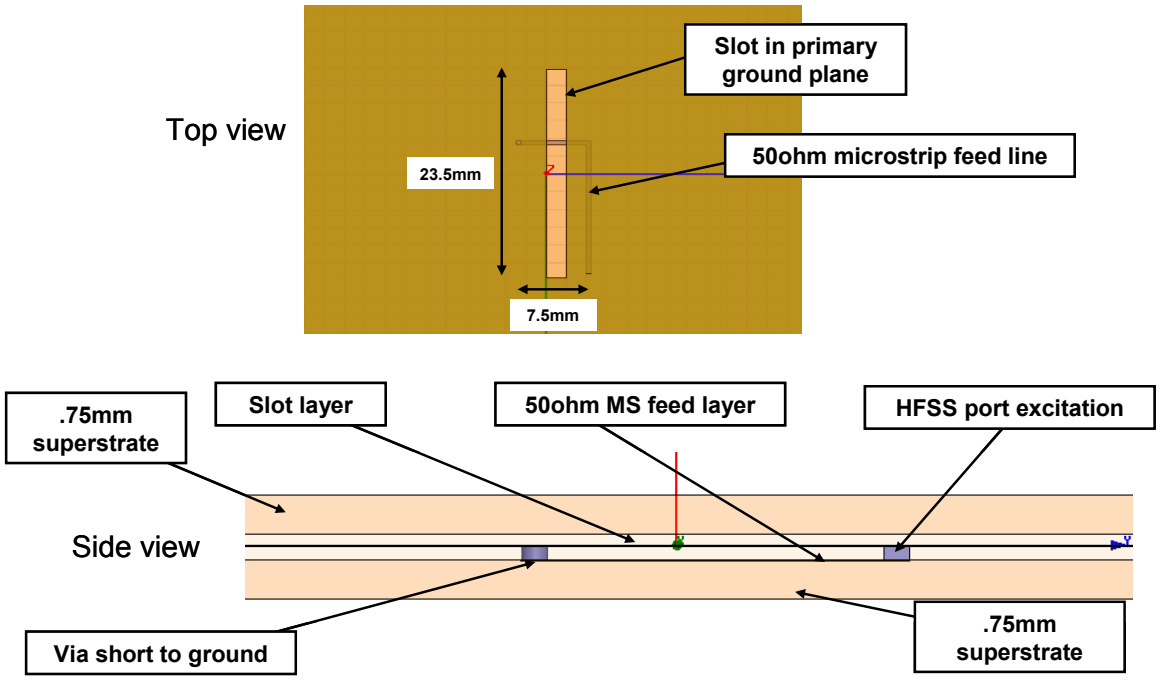

Figure 4.2: C-Band microstrip-fed slot antenna for array command and wireless power harvesting.

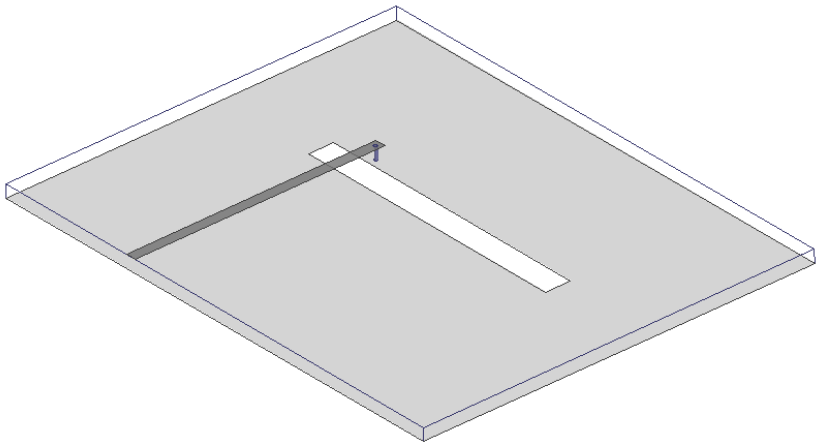

Figure 4.3: A microstrip-fed slot antenna model.

Simulation results

To better understand the performance of the proposed C-Band slot antenna, the topology in Figure 4.2 is simulated in HFSS. Figure 4.3 shows the simulated instantaneous bandwidth (VSWR<2:1) for the C-Band slot antenna is better than 400MHz around the 5.8GHz design frequency. This is many times better than bandwidth for a typical quarter-patch antenna which exhibits fractional bandwidth less than 1%. Though the bandwidth requirement for control of the array is not large the increased bandwidth of the slot antenna adds design robustness in that small tolerance differences across the array will not result in antenna elements operating significantly outside the range of the control signal carrier. If the quarter wave patch was used, its much smaller “notch-like” frequency response may result in this type of tolerance induced signal insensitivity.

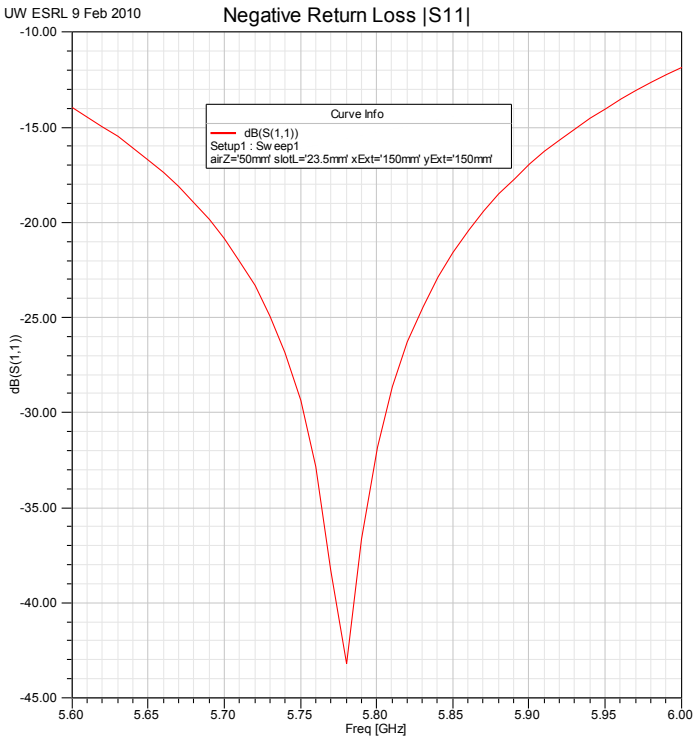

Figure 4.3: Simulated negative return loss for C-Band microstrip-fed slot antenna.

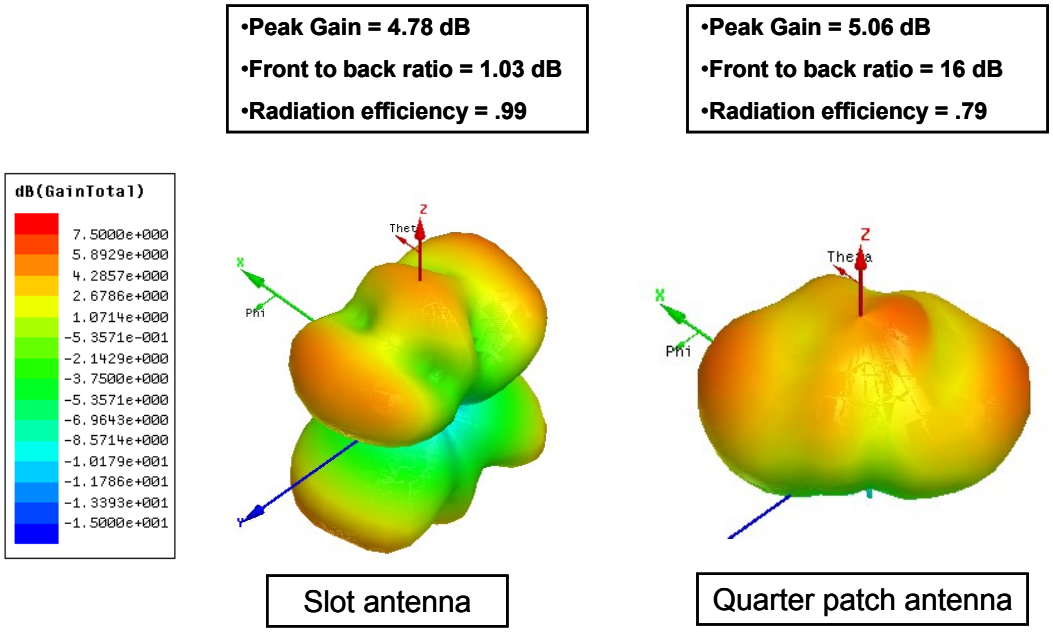

Figure 4.4: Simulated radiation patterns for microstrip-fed slot and quarter-patch antennas.

The radiation patterns in Figure 4.4 highlight the difference between the quarter-patch and slot antenna directivities. While the quarter-patch is nearly omni-directional in only one half space ($-90° < \theta < 90°$) the slot antenna has high gain regions in both half spaces ($-180° < \theta < 180°$). This means that even though the quarter patch confines radiation to one half space it is only slightly more directional (peak directivity 5.06dBi vs. 4.78dBi for slot antenna). As previously mentioned, the instantaneous bandwidth of the slot antenna is much higher than for the quarter-patch antenna (quarter-patch ~ 10MHz or <<1% while slot > 400MHz or 7%). This improves the robustness of the design against tolerance induced fabrication errors and/or changes in carrier frequency during operation. Additionally, the microstrip-fed slot antenna is preferred over the quarter-patch because of its efficient use of the available space. The feed line easily subtends regions near two X-Band patch feeds, as shown in Figure 4.5, facilitating the distribution of C-Band control to RF modules on a single layer.

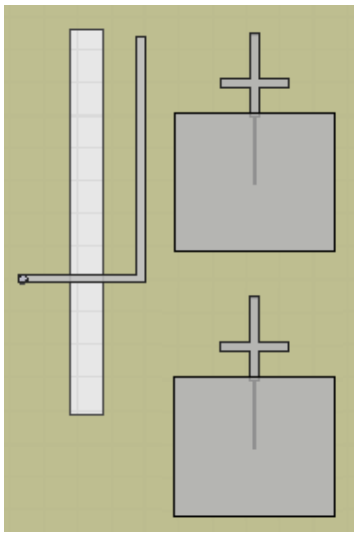

Figure 4.5: WiPAA unit cell comprised of 2 X-Band patch elements and 1 C-Band slot element.

4.2 Co-located radiating element test coupon

To test the antenna designs simulated above and gather a preliminary assessment of the deterioration in performance due to collocation, a prototype antenna, consisting of two WiPAA unit cells, is fabricated and tested. Side by side 1x2 arrays of X-Band patch antennas are fabricated each with a C-Band slot antenna located within the unit cell. Each antenna is fed with a line extended to the board edge and terminated in an edge launch SMA connector.

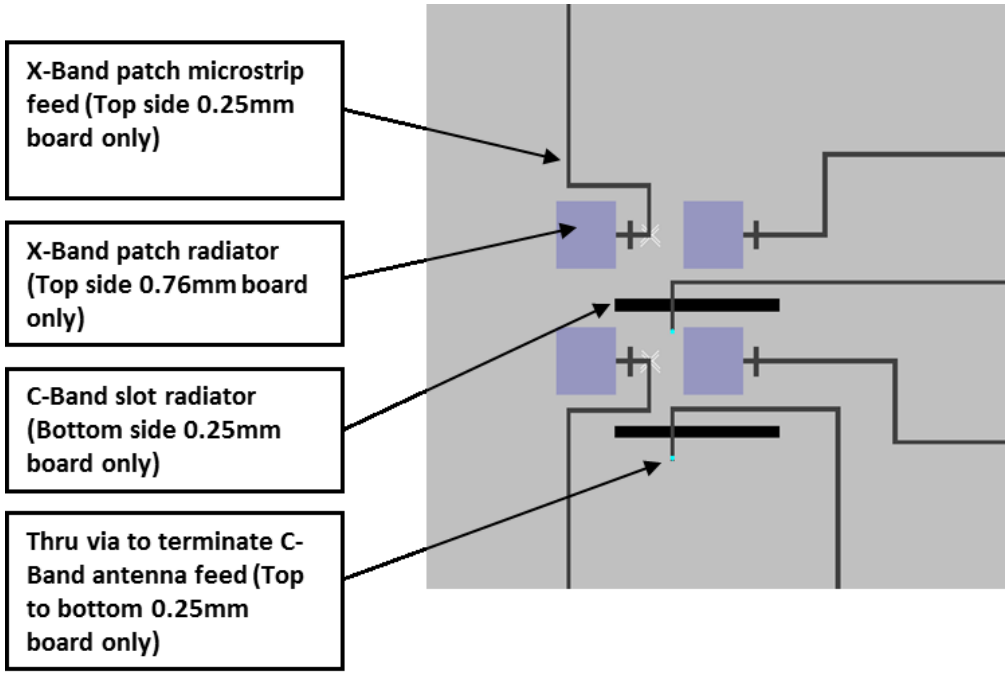

Figure 4.6: CAD drawing of a two WiPAA unit-cell test coupon.

A CAD drawing of the two layer board is shown in Figure 4.6. The drawing shows a WiPAA test coupon with an array of four linearly polarized X-Band patch elements interleaved with two C-Band antennas (microstrip-fed slots in ground plane). Each of the six antenna elements in the test coupon are fed with 50Ω microstrip lines. The board is composed of two dielectric layers: a .76 mm superstrate layer supporting X-Band patch elements and a .25 mm substrate layer with feed

lines, ground plane, and slot antennas. The substrate and superstrate layers are etched separately and held together using a multitude of fasteners around the perimeter of the 2x2 array. A picture of the fabricated substrate layer, including the holes for fasteners, is shown in Figure 4.7.

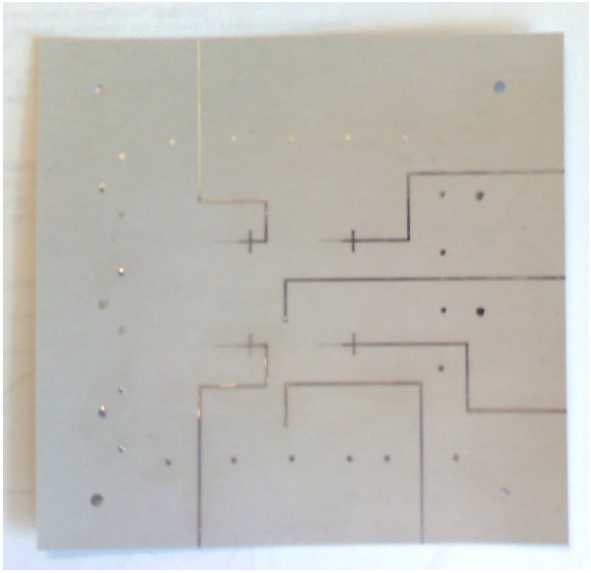

Figure 4.7: Fabricated substrate layer (feed network) for WiPAA test coupon.

Figure 4.8 shows the measured return loss for a single X-Band element in the small test array. The response shows a good match (VSWR<2:1) across a 400 MHz range from 9.4-9.8 GHz. Figure 4.9 shows the measured return loss for a single C-Band element in the small test array. The response shows a good match (VSWR<2:1) across an 800 MHz range from 5.6-6.4 GHz. The measured impedance bandwidth of the slot antenna is much larger than other proposed PCB-based apertures (e.g. quarter-patch antenna). A larger bandwidth can loosen the manufacturing tolerances required to control resonant frequency differences across the array. For this application, susceptibility to noise and/or interference is not a major concern because the control signal is designed to be quite strong (see Section III A) relative to noise and/or stray signals. In

Figure 4.9 we also see a small range of low return loss around 10 GHz. This measured response indicates a potential problem: specifically, if received X-Band RF passes through the C-Band slot and is directly coupled to the space-fed array feed it could create a path for direct coupling from space-side to feed-side, circumventing the element-wise phase delay imposed by the WiPAA. One major design feature limiting direct coupling is the space-side to feed-side polarization diversity. Polarization of X-Band patch elements on space-side is orthogonal to polarization of X-Band patch element on the feed-side. The C-Band slot is only sensitive to electric field polarized linearly in one dimension (vertically in Fig. 4). The polarization of the slot antenna is kept orthogonal to the space-fed array feed polarization which provides isolation from the X-band receive. By including this polarization isolation we can limit the effect of any direct coupling from space-side to feed-side through the C-Band slot antenna.

Figure 4.8: Measured |S11| for X-Band patch antenna element in array of 2 WiPAA unit cells.

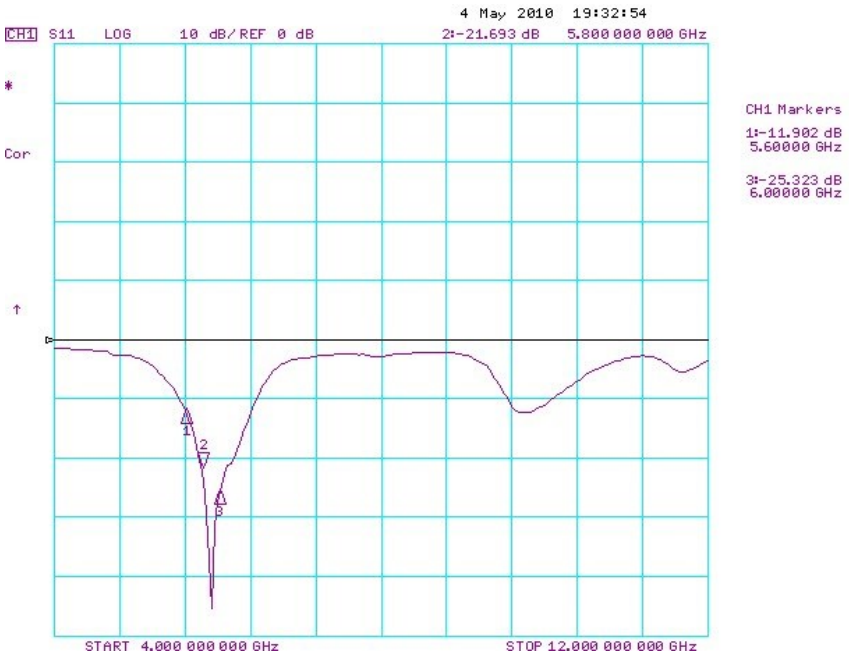

Figure 4.9: Measured |S11| for C-Band slot antenna element in array of 2 WiPAA unit cells.

Figure 4.10 shows the measured radiation pattern in the E-Plane for a single X-Band patch element plotted against the simulated embedded element pattern from a 4-element simulation. The measured element was the x-band patch element on the bottom left of the 4-element array in Figure 4.6. The simulation and the measurement show similar gain deterioration from $\theta = 25° - 60°$. The asymmetery in the pattern is expected because the measured/simulated patch element has neighboring elements on 2 sides and no neighboring elements on the other 2 sides.

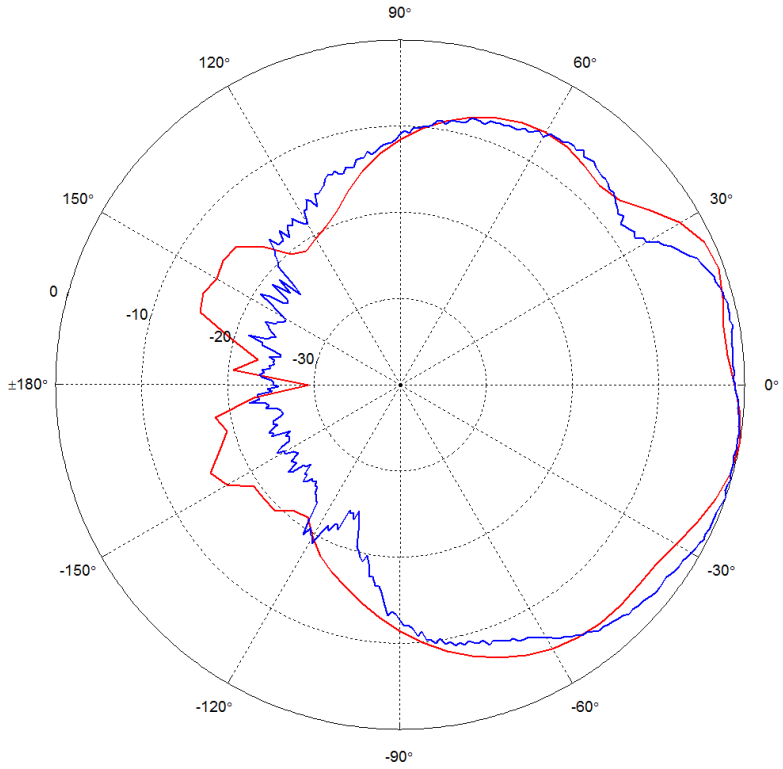

Figure 4.10: Measured E-Plane pattern for X-Band antenna element in array of 2 WiPAA unit cells and simulated E-Plane pattern for reference.

4.3 C-Band rectifier and wireless control circuit

The WiPAA uses a wireless signal to control the element-wise phase shift across the aperture face. Additionally, because there are no electrical connections amongst the unit cells the control signal must also provide the power needed to run the phase control circuitry. At each WiPAA unit cell this circuitry consists of two X-Band phase shifters and a control IC to interpret the control signal and provide the correct bias voltages to each phase shifter. These requirements suggest that a modulated C-Band RF signal will be propagated to the unit cell, received by the C-Band slot antenna, and both DC voltage and digital data stream will be extracted. To accomplish this we need to employ both a RF-DC rectifier and a RF demodulator. For the former, the well-known Dickson topology is chosen for its simplicity and scalability [33].

Charge pump considerations

When a Dickson charge pump is connected to an RF source the result is a rectifier with a DC output that can be higher than the peak incident RF voltage. Increasing the number of stages in the charge pump has the effect of further increasing the DC voltage at the expense of DC current progressively increasing the output impedance of the rectifier. The ideal number of charge pump stages depends on the impedance of the load and will determine the input resistance as seen by the RF source. Figure 4.11 shows a 2-stage Dickson charge pump with RF source on the left and the DC output voltage V_{DC} taken across the output capacitor at the far right.

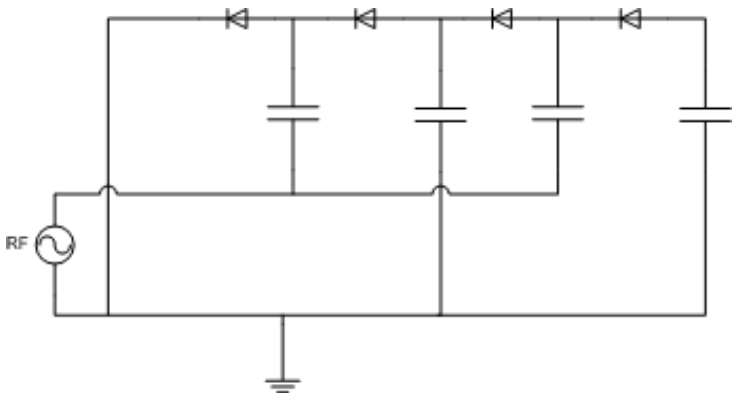

Figure 4.11: A 2-stage Dickson charge pump.

The required output voltage and the load resistance are dictated by the choice of phase shifter and control IC. In the development of the first steerable prototype a 4-bit digital phase shifter from Hittite Microwave is used (HMC543LC4B). This chip provides 0 - 360° phase delay with 22.5° of resolution across a frequency range of 8-12GHz. The phase shifter is controlled with complementary logic of 0/-3V and presents a load of .9MΩ. The control IC is implemented using

an ultra-low power MCU from Texas Instruments (MSP430F2112). This IC can provide up to 24 bits of general purpose I/O (GPIO) with 300μA current consumption at 3V (10kΩ load).

Rectifier simulation and measurement results

Multiple charge pump designs were simulated using Ansoft Designer and a harmonic balance simulation. To compare the voltage outputs and RF to DC conversion efficiency, charge pumps with from 1 to 5 stages were analyzed. Figure 4.12 shows an Ansoft Designer model of a 3-stage charge pump. The simulation includes an enhanced SPICE diode model for each of the Schottky diodes in the charge pump. Both the HSMS-285 zero-bias Schottky detector diode and the HSMS-286 microwave Schottky detector diode from Avago Technologies were used in simulation [34] [35]. The HSMS-285 zero-bias Schottky diodes are useful when DC-bias is not available which is the case in the RF-DC rectifier design shown here. The HSMS-285 diode is typically used as a detector at frequencies below 1.5GHz and at power levels below -20dBm. Though we are not using the device in a detector circuit, our higher input power levels and higher frequency of operation may result in poor performance from the HSMS-285 diode. We also consider the HSMS-286 microwave Schottky detector diode and compare the performance of the two devices in simulation. Although the HSMS-286 is typically used as a DC-biased detector, it is also useful for operation without bias at frequencies above 4GHz and power levels above -20dBm.

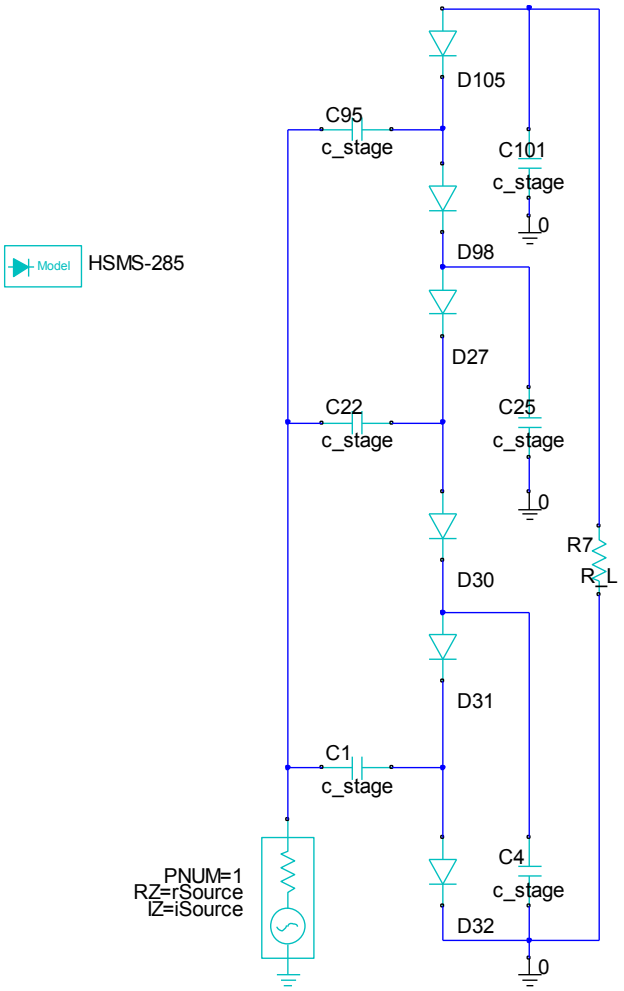

Figure 4.12: Ansoft Designer model of 3-stage Dickson charge pump.

The SPICE parameters for the HSMS-285 used in the simulation are provided in Table 4.1 and the SPICE parameters for the HSMS-286 are provided in Table 4.2. The load resistance (R_L) used in the simulation is 8kΩ which corresponds to the worst case current draw from the TI MSP430F2112 when running with a 1MHz clock and an output voltage of 2.4V. We can use a resistor in place of the microcontroller and forgo the voltage regulator because the most basic implementation of the MCU code does not put the device into any of the available low power

modes and thus the current draw remains relatively constant while the WiPAA system is illuminated with the 5.8GHz power signal.

Table 4.1: Diode SPICE parameters for HSMS-285 used in charge pump simulations.

Name	Description	Value	Unit
I_S	Saturation current	3E-6	A
N	Emission coefficient	1.06	(none)
I_{BV}	Current at breakdown	3E-4	A
B_V	Breakdown voltage	3.8	V
R_S	Series resistance	25	Ω
C_{J0}	Zero bias junction capacitance	0.18	pF
VJ	Junction potential	0.35	V
E_G	Barrier height	0.69	V

Table 4.2: Diode SPICE parameters for HSMS-286 used in charge pump simulations.

Name	Description	Value	Unit
I_S	Saturation current	5E-8	A
N	Emission coefficient	1.08	(none)
I_{BV}	Current at breakdown	1E-5	A
B_V	Breakdown voltage	7	V
R_S	Series resistance	6	Ω
C_{J0}	Zero bias junction capacitance	0.18	pF
VJ	Junction potential	0.65	V
E_G	Barrier height	0.69	V

To compare the two Schottky diodes, the RF input power level is swept from -5dBm to +20dBm in charge pump circuits of from 1-5 stages and the output simulated output voltage is recorded. This is done for identical circuits using either the HSMS-285 or the HSMS-286.

Figure 4.13 shows the DC output voltage (V_{DC}) vs. the RF input power level (P_{in}) for five Dickson charge pumps (from 1-5 stages) when the HSMS-285 zero-bias detector diode is used. Figure 4.14 shows DC output voltage (V_{DC}) vs. the RF input power level (P_{in}) for five Dickson charge pumps (from 1-5 stages) when the HSMS-286 microwave detector diode is used.

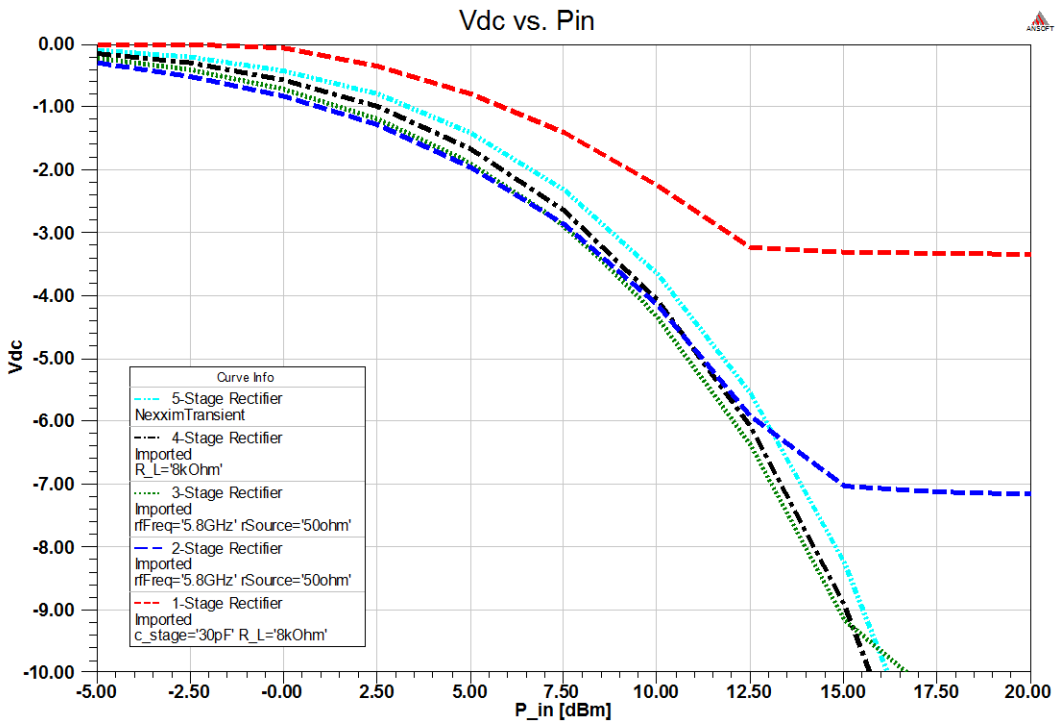

Figure 4.13: V_{DC} vs. P_{in} for 1-5 stage charge pump simulation with HSMS-285.

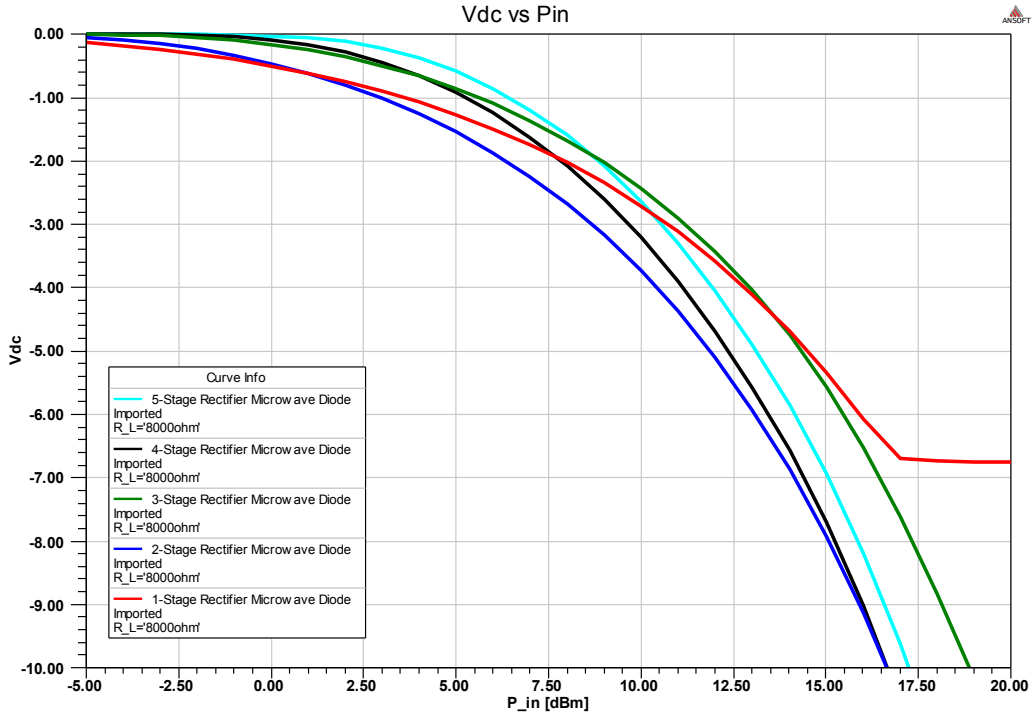

Figure 4.14: V_{DC} vs. P_{in} for 1-5 stage charge pump simulation with HSMS-286.

From the results of the two simulations we can see that the circuit with the HSMS-285 diode achieves $V_{DC} < -3V$ at a lower P_{in} than the circuit with the HSMS-286 diode. We can also see that the 2-stage rectifier and the 3-stage rectifier achieve $V_{DC} < -3V$ at $P_{in} = +7.5dBm$ which is the lowest of any of the simulated cases. Figure 4.14 shows the RF to DC conversion efficiency vs. P_{in} for each of the five Dickson charge pump designs using the HSMS-285 diode.

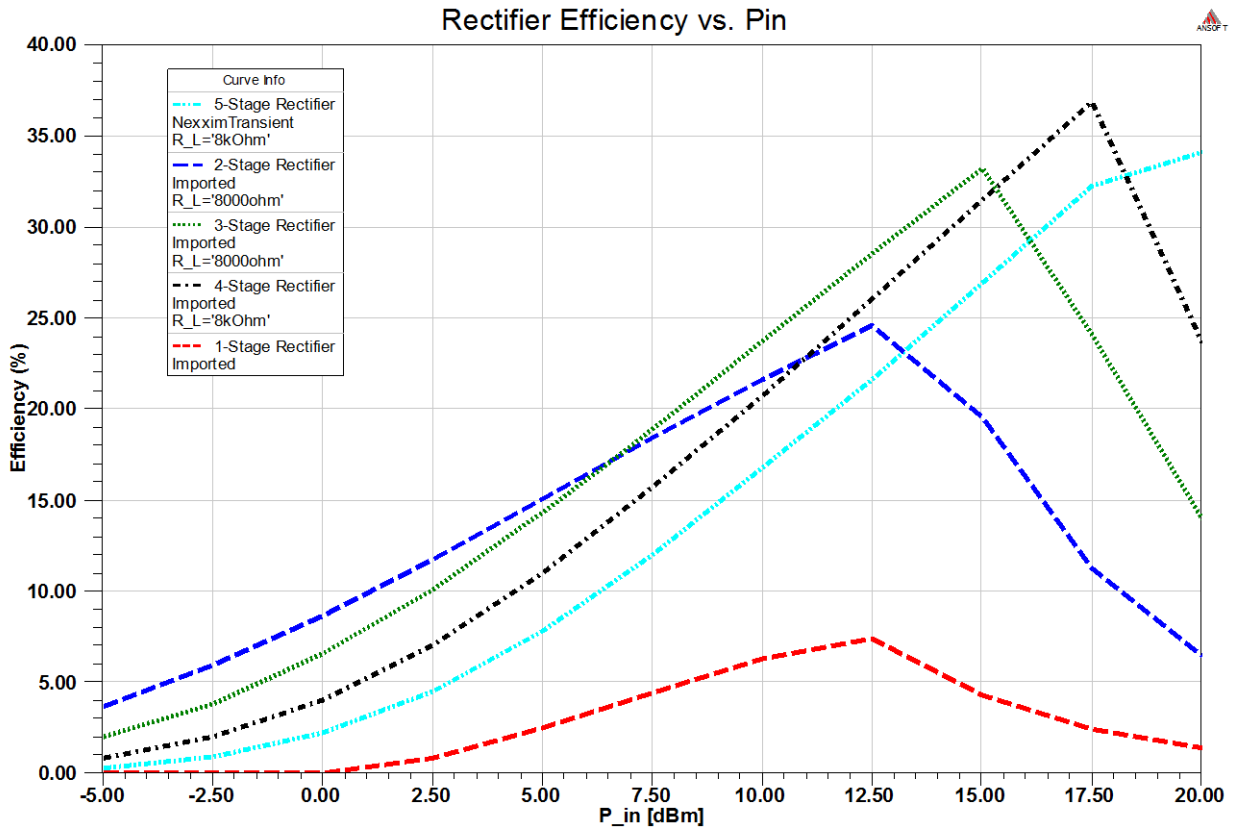

Figure 4.14: Simulated RF to DC conversion efficiency for 1-5 stage charge pumps

The RF to DC conversion efficiency is calculated using a ratio of output power to input power:

$$Efficiency = \frac{V_{DC}^2}{R_L} \times \frac{1}{P_{in}}$$

The simulation shows that a rectifier containing either 2 or 3 charge pump stages is most efficient at producing a $|V_{DC}|$ of approximately 3V. For both designs the RF to DC conversion efficiency is approximately 20% when the output voltage is 3V. We can also see from the simulation that none of the charge pump designs have maximum efficiency at the P_{in} required to produce a $|V_{DC}|$ of 3V. We also note that the charge pump has not been specifically optimized for an RF input frequency of 5.8GHz.

Figure 4.15 shows a fabricated Dickson charge pump rectifier prototype. The test coupon has a 50Ω input, a Dickson charge pump and a 10kΩ resistor to simulate the MCU load. To examine the relationship between number of stages and output voltage the number of stages for the Dickson charge pump was varied from 1 to 5. Figure 4.16 shows the measured V_{DC} versus the RF power level P_{in} for a 5.8GHz CW source. Because of the requirement that phase shifter be driven with 0/-3V logic (relative to RF ground) we show the measured V_{DC} as a negative voltage.

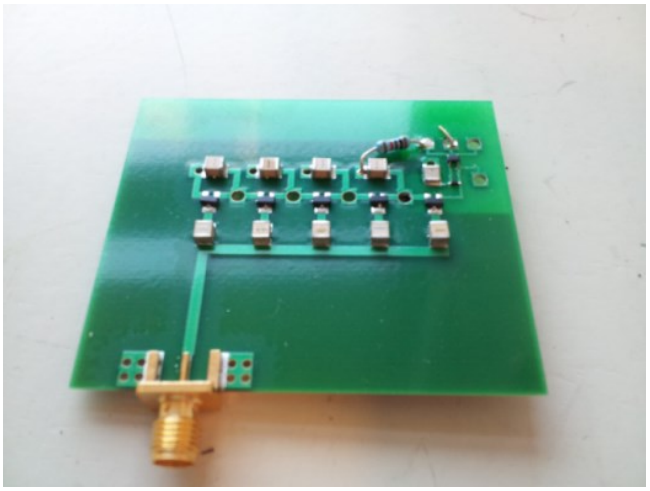

Figure 4.15: 1-5 stage rectifier test coupon.

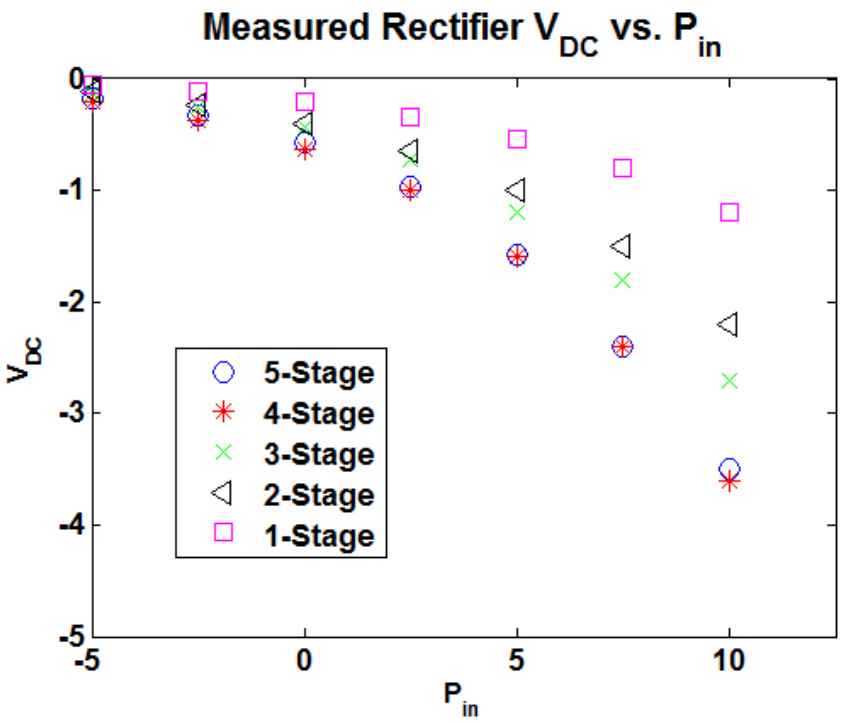

Figure 4.16: Measured rectifier performance with 10kΩ load using a 5.8GHz CW source.

To increase the RF to DC conversion efficiency of the rectifier circuit a matching circuit is added to the rectifier input. In the previous simulations 50Ω source impedance was assumed however the input impedance of the rectifier with 8kΩ load is higher than 50Ω. Reactive matching can reduce the input impedance of the rectifier near resonance and result in improved RF to DC conversion efficiency at 5.8GHz. This also means a 1-stage rectifier can be implemented with good efficiency, reducing the total component count and board area required for the power harvesting circuit.

Figure 4.17 shows a 1-stage rectifier with an LC input matching circuit. The shunt reactance reduces the input impedance of the rectifier circuit when the inductance and capacitance is carefully chosen for the input RF frequency. The values of the matching components are:

$L_{match} = 0.16nH$ and $C_{match} = 4.53pF$. The value of the smoothing capacitors is, as in previous simulations, $C_{stage} = 100pF$.

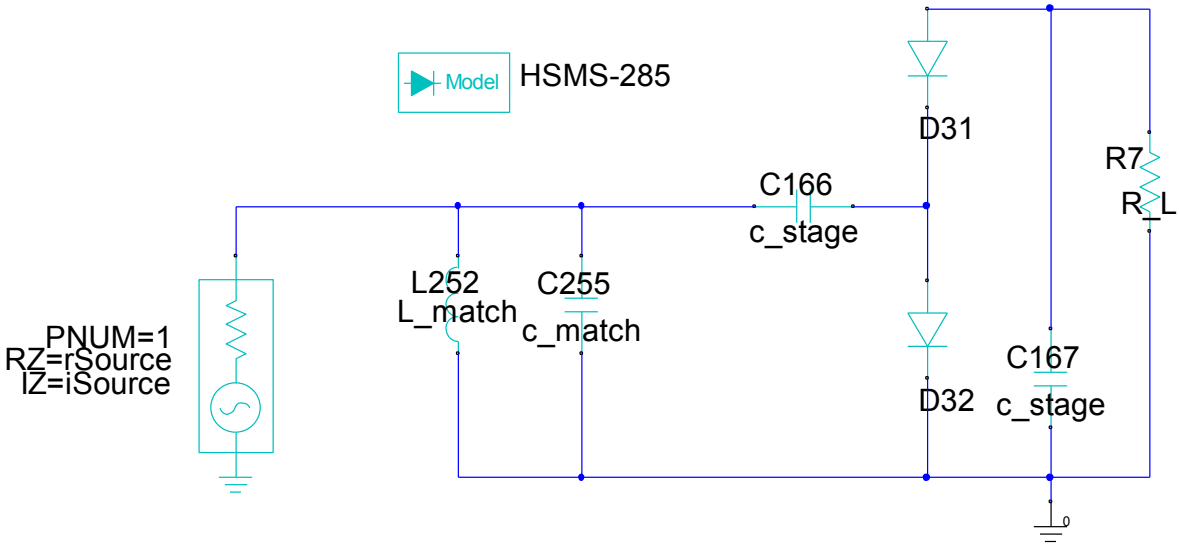

Figure 4.17: 1-stage rectifier with matching circuit.

The circuit in figure 4.17 was simulated with RF input power $P_{in} = 5dBm$, load resistance $R_L = 8000\Omega$, and source impedance of $R_{source} = 500\Omega$. The higher source impedance makes the match less sensitive to frequency differences, improves the overall efficiency, and is realistic given the range of achievable slot antenna output impedances with the chosen topology. The circuit in 4.17 is simulated both with the LC matching circuit (as shown) and without the LC matching circuit (not shown). The frequency is swept from 5.75GHz to 5.85GHz and the RF to DC conversion efficiency of the rectifier with and without LC matching circuit is produced. Figure 4.18 shows the efficiency vs. frequency for both circuits. Whereas only 5% efficiency is shown for the circuit without LC matching, an efficiency of near 50% is shown near 5.8GHz for

the circuit with LC matching. Reactive matching is included in the design of the rectifier for use with the 1-D WiPAA in Chapter 6 as it allows for the use of rectifiers with fewer stages and better RF to DC conversion efficiency.

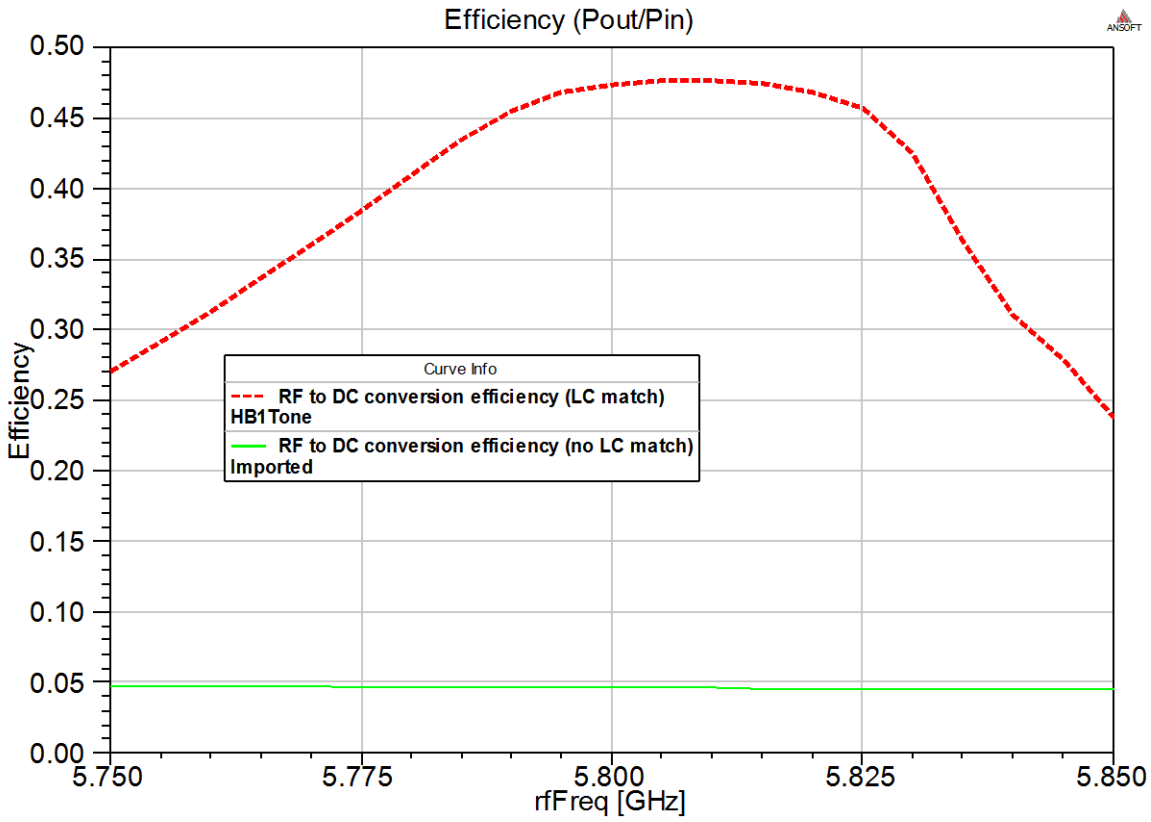

Figure 4.18: RF to DC conversion efficiency of 1-stage rectifier with and without LC matching circuit.

Wireless control circuit

A slight amplitude modulation of the RF power signal can produce a serial data stream and a simple threshold detector can operate as a 1-bit A/D converter. This configuration has been shown effective in a variety of wirelessly powered applications [36]. The control IC is used to interpret the serial data stream encoded with scan angle information and, based on the element

location in the array, command the desired phase shift. Figure 4.19 shows a block diagram of the wireless control system.

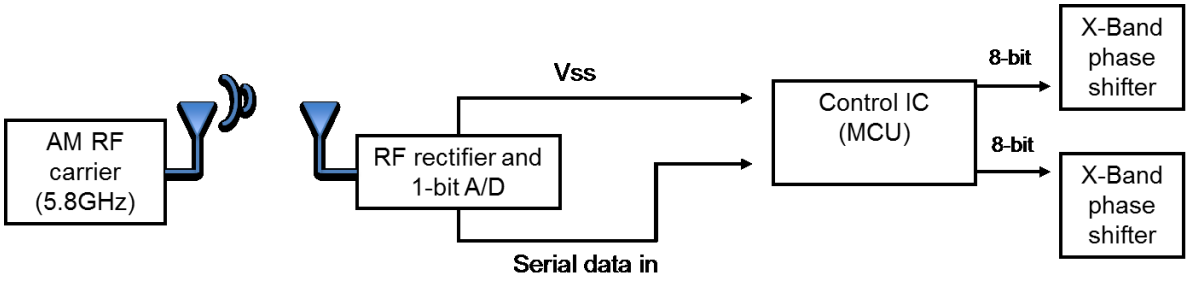

Figure 4.19: Block diagram of example WiPAA control circuit

Chapter 5: A PASSIVE 2D WIPAA

5.1 2D array design

To demonstrate the RF performance of the WiPAA capacitively coupled patch radiators in an array environment an unfocused space-fed array is constructed. Figure 5.1 shows conceptual drawings of a space-fed array using the developed X-Band and C-Band elements. Figure 5.1a shows the array from one side of the ground plane (side 1) while Figure 5.1b shows the array from the opposite side (side 2). Although the goal in this phase is to demonstrate a space-fed array without any onboard electronics, a space is shown on the conceptual drawing where a phased array module may go in future iterations.

The overlaid view in Figure 5.1c shows both sides of the space-fed antenna via additional transparency in the ground plane layer. From this drawing, it is clear that the X-Band patch antenna on side 1 is horizontally polarized while the X-Band patch on side 2 and the C-Band slot are vertically polarized. The orthogonal polarization of space and feed sides provides isolation from direct coupling either through or around the space-fed array. This is particularly useful for testing small and medium sized arrays, as the coupling around the edges of the array is isolated from the receiver via polarization mismatch.

A prototype antenna is constructed to demonstrate fabrication and assembly of the full space-fed array. The prototype antenna is fabricated using a fixed path length from feed-side element to space-side element regardless of the elements position relative to the center of the array. Additionally, the array employs direct coupling from feed-side to space-side without phase or amplitude conditioning electronics. For the highest probability of success, the complexity was kept low, and thus the prototype array was left unfocused (spherical isodelay lines at feed-side

produce spherical isodelay lines at space-side). Figure 5.2 shows a CAD drawing of the 6x6 unit cell WiPAA test article.

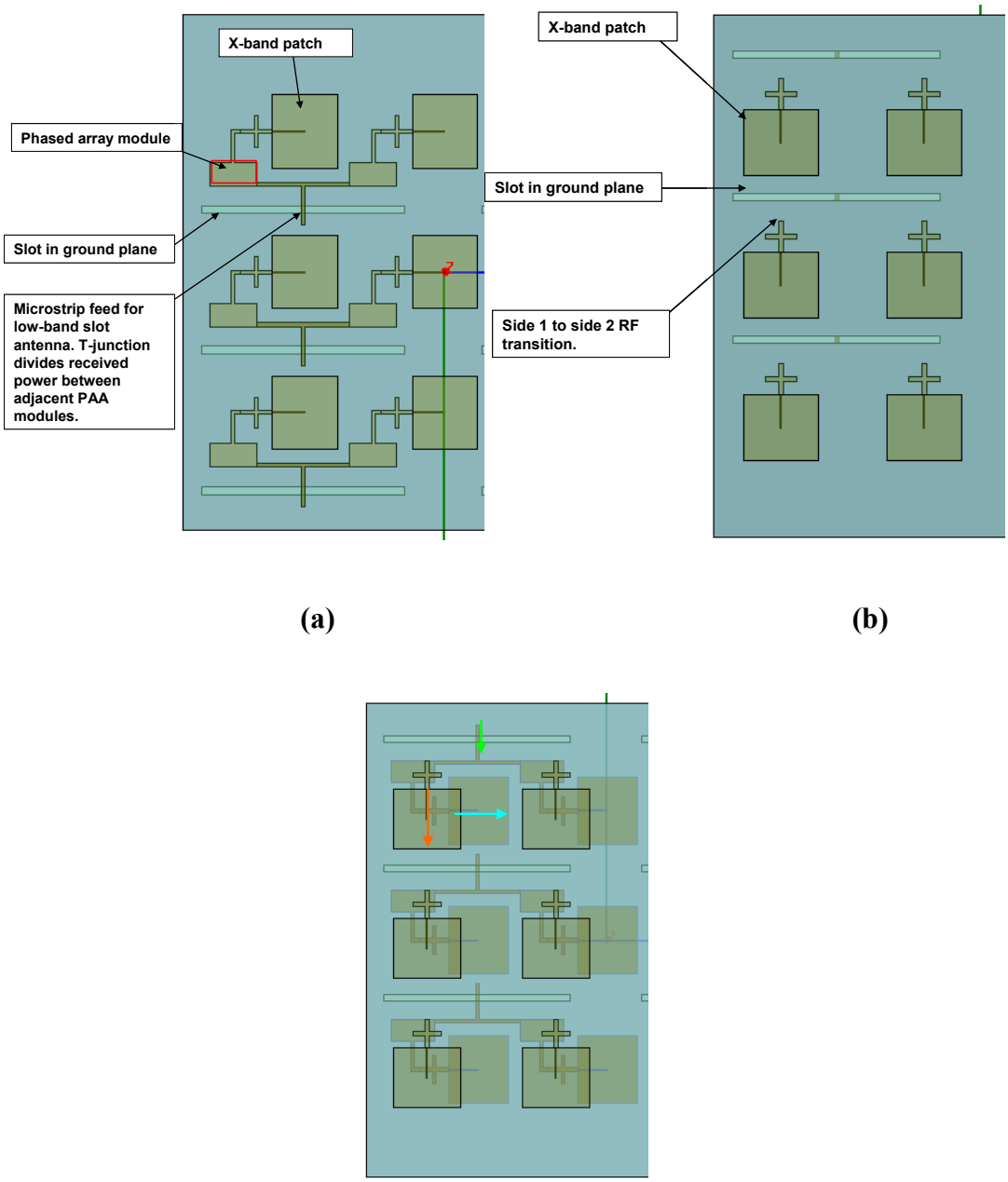

Figure 5.1: Space-fed array of capacitively coupled X-Band patch elements. **(a)** Side 1 **(b)** Side 2 **(c)** Sides 1 and 2 overlaid.

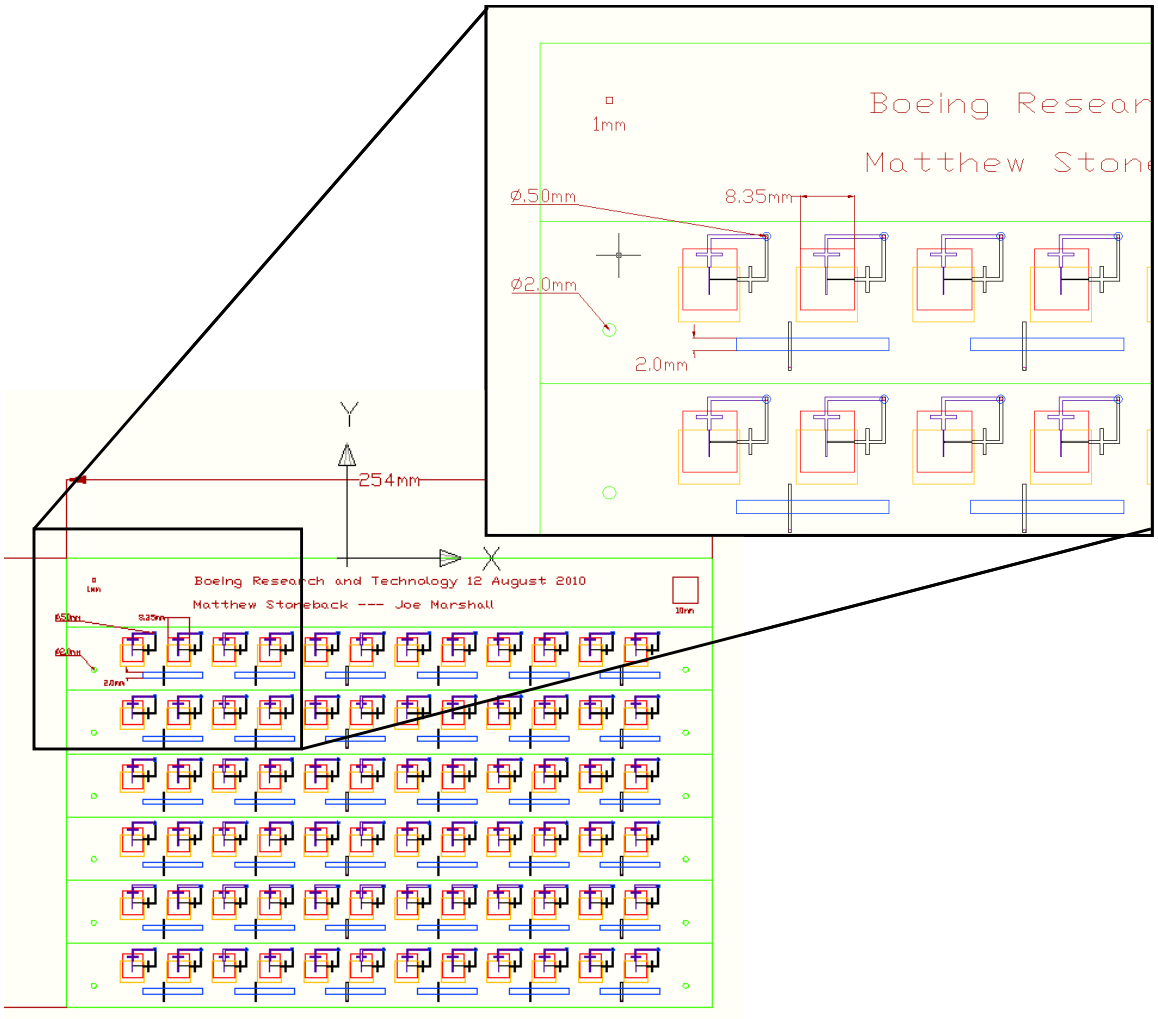

Figure 5.2: CAD drawing of 6x6 unit cell WiPAA test article.

As in the conceptual array above, the feed and space side patch antennas are both linearly polarized and oriented with a rotation of 90° relative to each other. Figure 5.3 shows an exploded view of the WiPAA unit cell. Once the pattern is etched on each constituent board the antenna is assembled in three steps: first the two feed boards are aligned and bonded, next the thru via holes are drilled and plated, and finally the patch superstrate layers are aligned and bonded.

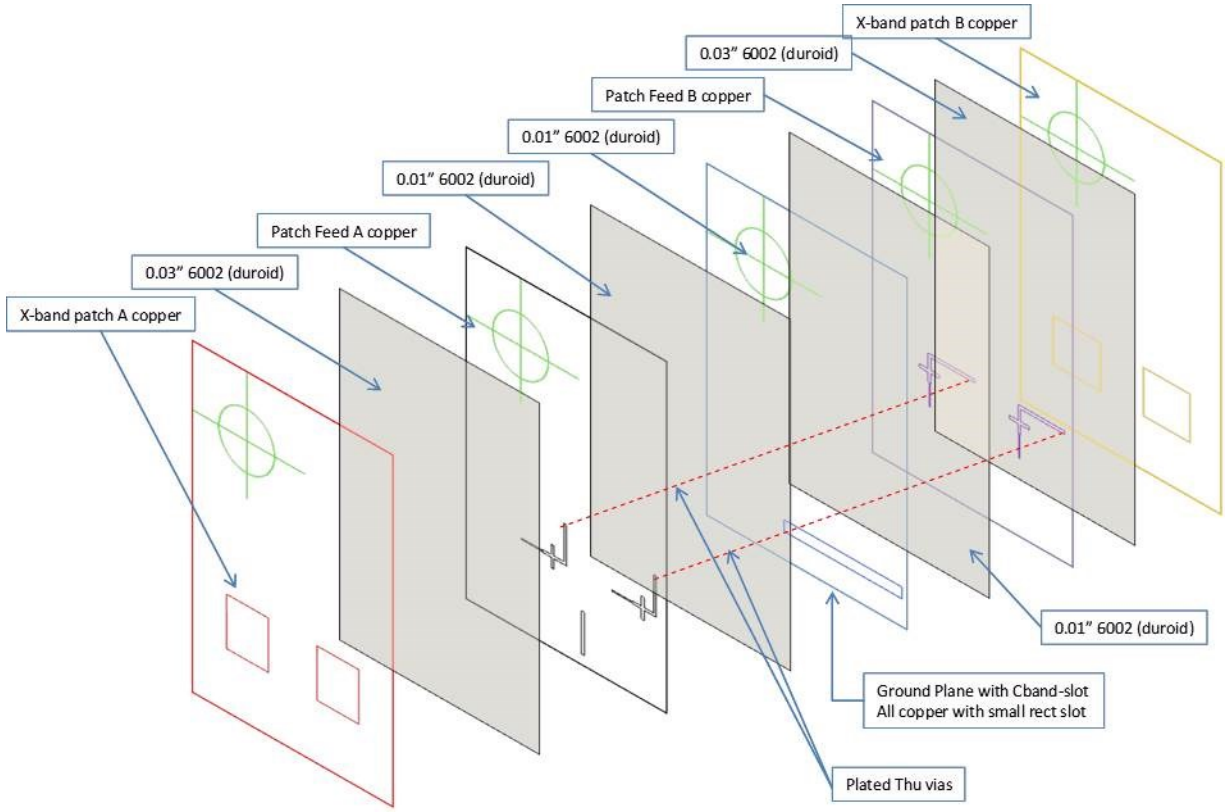

Figure 5.3: Exploded view of WiPAA unit cell showing 5 copper layers separated by 4 sheets of dielectric material.

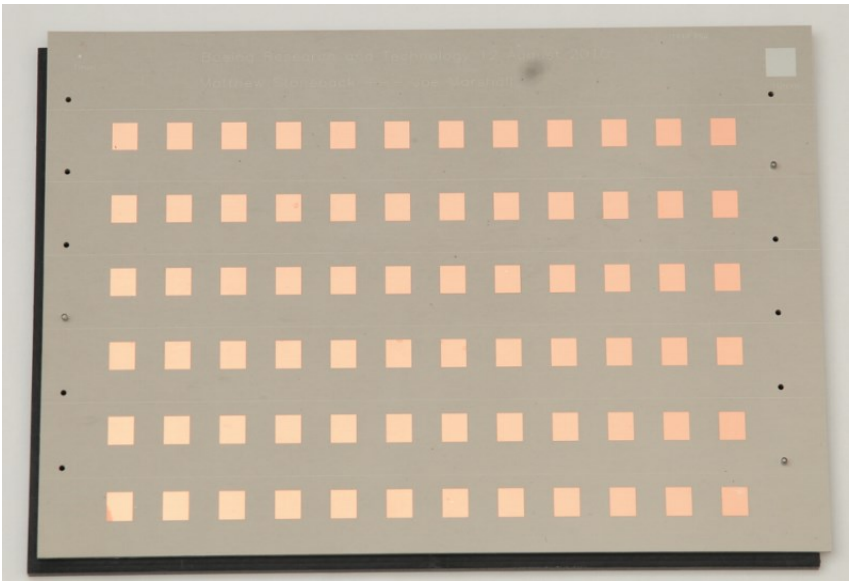

Figure 5.4: Top layer of fabricated WiPAA test article.

5.2 Test procedure

To test the passive WiPAA prototype, a unidirectional measurement system is created using a pyramidal horn as the transmit antenna and ridged waveguide as receive antenna. The absolute propagation loss of the link is measured both with and without the WiPAA in the propagation path. Additionally, the ridged waveguide antenna is rotated 90° in each configuration to capture the gain of vertically polarized transmit to vertically polarized receive (co-polarized) as well as vertically polarized transmit to horizontally polarized receive (cross-polarized). The measurement of the unidirectional link loss without WiPAA in place is used as a baseline to normalize the measurement of the unidirectional loss with the WiPAA in place. In this regard, the primary case of interest is the cross-polarized loss with WiPAA in place relative to the co-polarized loss without WiPAA in place. Ideally, a passive and unfocused space-fed array is not expected to scale gain (amplify) or alter the directivity over angle (focus) of the source antenna, however the finite size of the prototype may be insufficient to capture and reradiate all of the energy produced by the source antenna. To address error due to finite array size, we normalize the measured link gain with WiPAA in place using information about the radiation characteristics of the pyramidal horn source antenna.

Source illumination normalization

The feed side of the prototype space-fed array is illuminated with an X-Band pyramidal horn antenna at a distance sufficient to put the array in the radiating near-field of the source. Figure 5.5 shows a CAD model of the WiPAA at a distance of 9” from the aperture of a pyramidal horn antenna. Accurate measurement of the loss incurred as waves propagate through the WiPAA requires normalization by a factor of the portion of radiated power incident on the array surface.

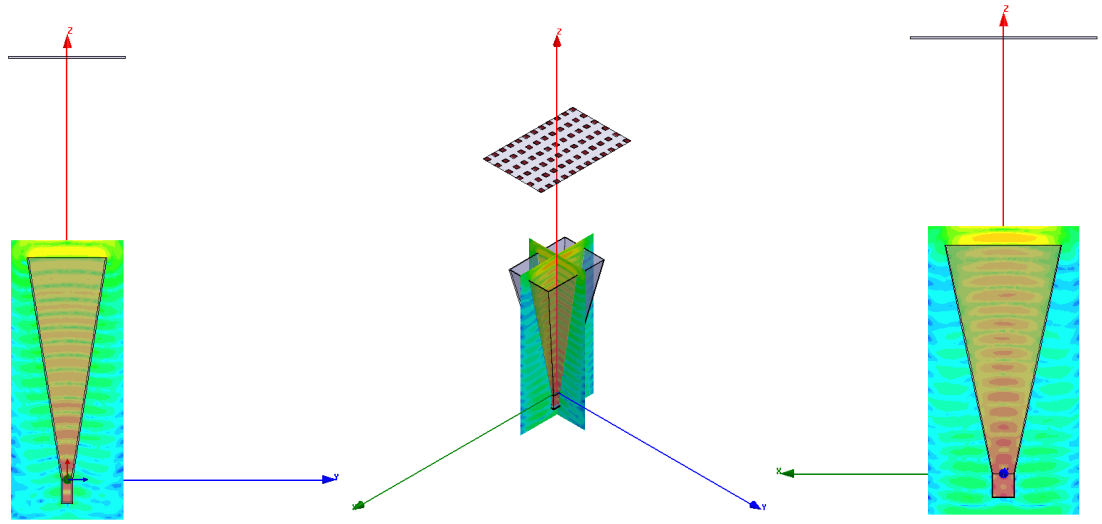

Figure 5.5: Simulated X-Band pyramidal horn antenna feed (WiPAA shown for reference).

Because a model extent of sufficient size to include both feed horn and WiPAA is computationally impractical, a projection technique is used to approximate the power incident on the array surface. First the apex of the horn antenna is found by extending the tapered sidewalls until the intersection point was found. From the apex, a pair of lines was drawn (in both E-plane and H-plane) from the apex to the edges of the WiPAA stood off at a distance of 9” from the horn aperture. In both E and H plane the lines define a cone in which radiated power density from the aperture of the horn will impinge on the surface of the WiPAA. We can equate the radiated power density through a cross section of the cone that resides inside the model extent to the radiated power density through the surface of the WiPAA. Figure 5.6 shows a diagram of the projected surface used to calculate the power incident on the array.

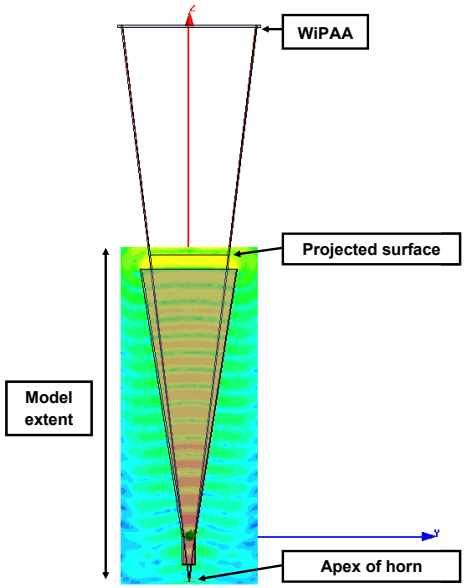

Figure 5.6: Diagram showing relationship of WiPAA face to projected surface used in power calculation.

The power incident on the projected surface is calculated using:

$$P_{inc} = \int_S Re(E \times H^*) \cdot dS$$

To normalize the measurement results we use a source illumination normalization factor defined as:

$$N = \frac{P_{inc}}{P_{rad}}$$

Where P_{rad} is the total power radiated from the pyramidal horn. To normalize absolute gain measurements from a spectrum analyzer, the log scale value should be subtracted from the measured data for cases where the WiPAA is in place. As suggested by Figure 5.6, HFSS is used to simulate the pyramidal horn antenna. To check the method, four different cross sections are

taken along the pyramidal cone extending from the WiPAA edges back to the apex of the horn. Each projected surface lies some distance (D) between the aperture face and the actual WiPAA test location. The source illumination normalization factor is calculated for each: **N = .82, .84, .86, .82** for **D = .1", .5", 5.5", 9"** respectively. The average N is used to normalize the measurement results below $\overline{N}$ **= .835**. In log scale, $\overline{N}_{dB}$ **= -.783dB**.

5.3 Test results

Testing of the passive WiPAA prototype involved four unique configurations of source antenna, receive antenna, and WiPAA test article. They are:

- **Test configuration #1:** Source antenna vertically polarized; receive antenna vertically polarized; no WiPAA in place.
- **Test configuration #2:** Source antenna vertically polarized; receive antenna vertically polarized; WiPAA in place.
- **Test configuration #3:** Source antenna vertically polarized; receive antenna horizontally polarized; no WiPAA in place.
- **Test configuration #4:** Source antenna vertically polarized; receive antenna horizontally polarized; WiPAA in place.

A measurement of test configuration #1 provides a normalizing factor to facilitate transcription of the recorded absolute gain for subsequent tests into relative gain. Test configuration #2 demonstrates the relative isolation of the (horizontally polarized feed side) WiPAA to cross-polarized incident fields. Test configuration #3 demonstrates the relative isolation of the receive antenna to cross-polarized incident fields. Test configuration #4 demonstrates the relative gain of

the WiPAA test article. Specifically, two comparisons can be made: Comparing the absolute gain of test configuration #1 to the absolute gain of test configuration #4 gives a measure of the loss due to the WiPAA hardware and comparing the relative gain of test configuration #3 to the relative gain of test configuration #4 demonstrates that this effect is due to signal propagating through the WiPAA test article and not via direct coupling from source to receiver.

An image of the test setup and the corresponding measurement result is shown below for each of the four configurations. Each plot of measurement results displays absolute (measured) gain and, in the case of test configuration #4, the gain is not normalized using the source illumination normalization factor.

Figure 5.7 shows test configuration #1 which consists of vertically polarized source and vertically polarized receive antenna with no WiPAA in place. The synthesizer output power is set to 0dBm. Figure 5.8 shows the measured signal strength at the receive antenna from 5GHz to 12GHz. The response is relatively flat and between -38.5dBm and -35.5dBm from 7.8GHz to 12GHz. A sharply declining gain is observed as the frequency is decreased from 6.7GHz towards 5GHz. This is due to the waveguide cutoff (6.5GHz) of the WR-90 feed of the source antenna. The absolute gain at the 9.5GHz WiPAA center frequency is -35.85dB.

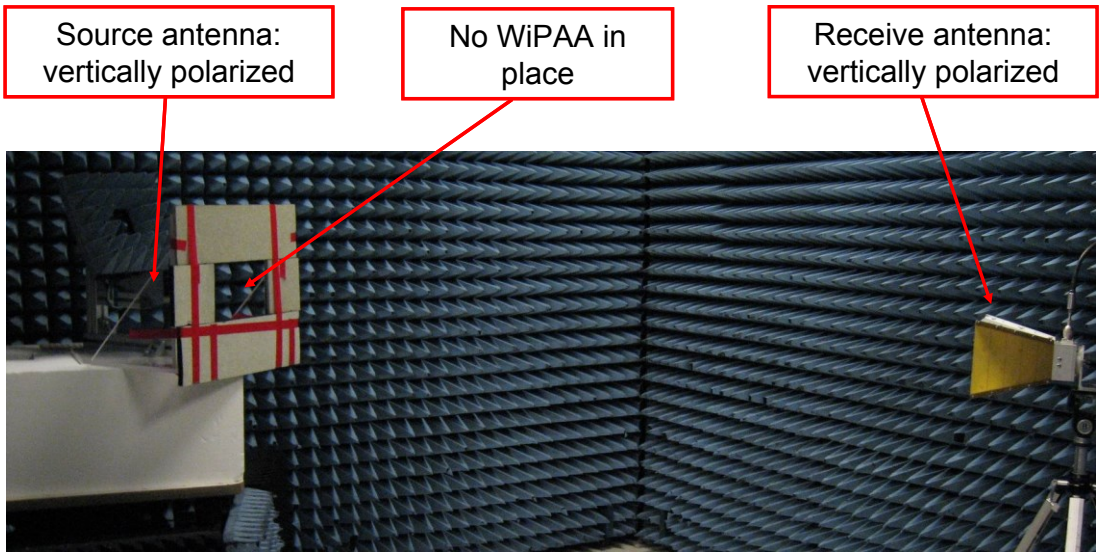

Figure 5.7: Test configuration #1: Vertically polarized source, vertically polarized receive, and no WiPAA in place.

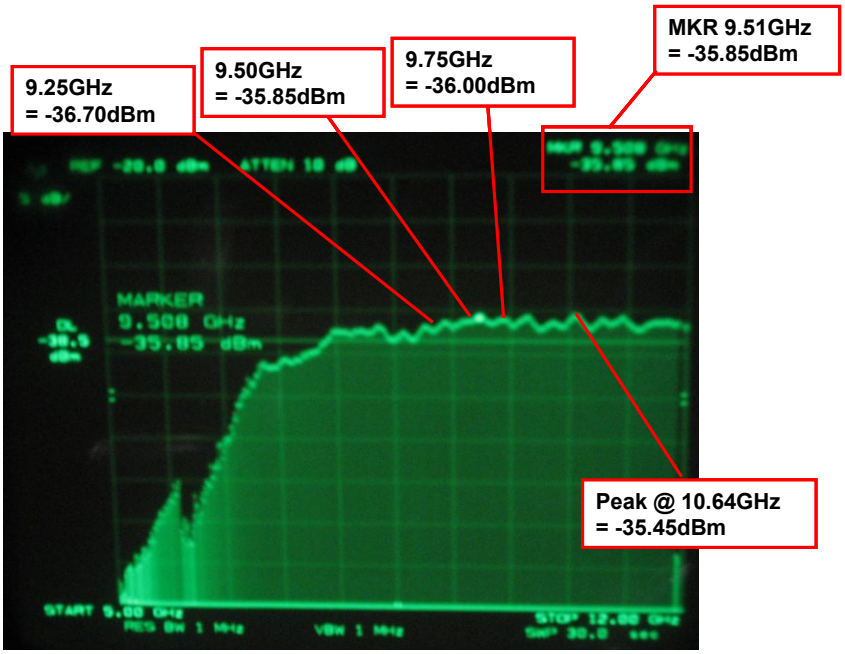

Figure 5.8: Spectrum analyzer measurement for test configuration #1: Vertically polarized source, vertically polarized receive, and WiPAA in place.

Figure 5.9 shows test configuration #2 which consists of vertically polarized source and vertically polarized receive antenna with WiPAA in place. The synthesizer output power is set to 0dBm. Figure 5.10 shows the measured signal strength at the receive antenna from 5GHz to 12GHz. The response is heavily attenuated (-15 to -30dB) relative to configuration #1 with no WiPAA in the range 7GHz to 12GHz. A peak gain is observed at 6.65GHz where the edge of the slot antenna band meets the steeply declining gain response of the pyramidal horn source antenna. The absolute gain at the 9.5GHz WiPAA center frequency is -54.05dB.

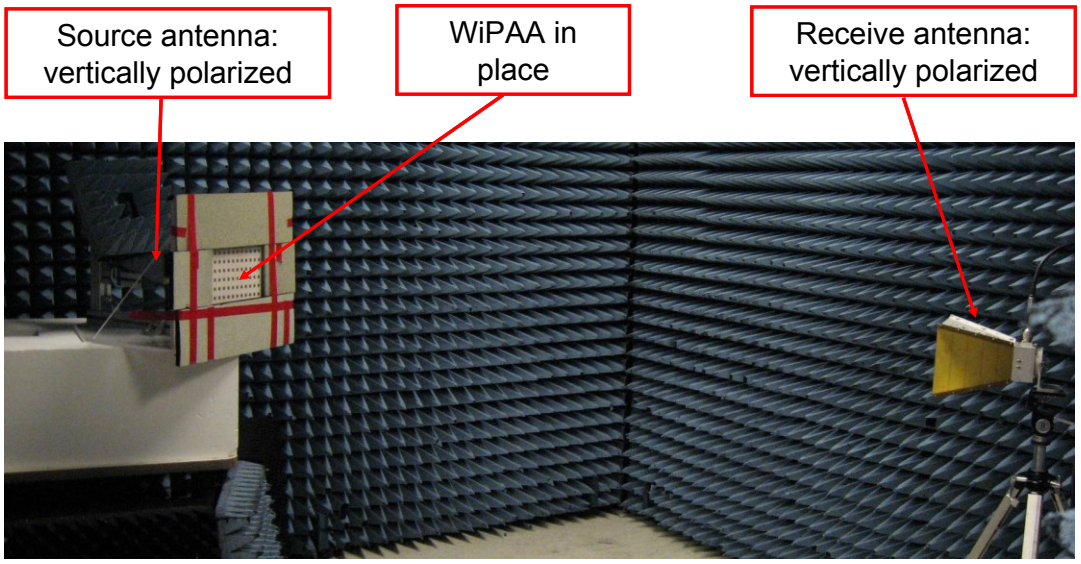

Figure 5.9: Test configuration #2: Vertically polarized source, vertically polarized receive, and WiPAA in place.

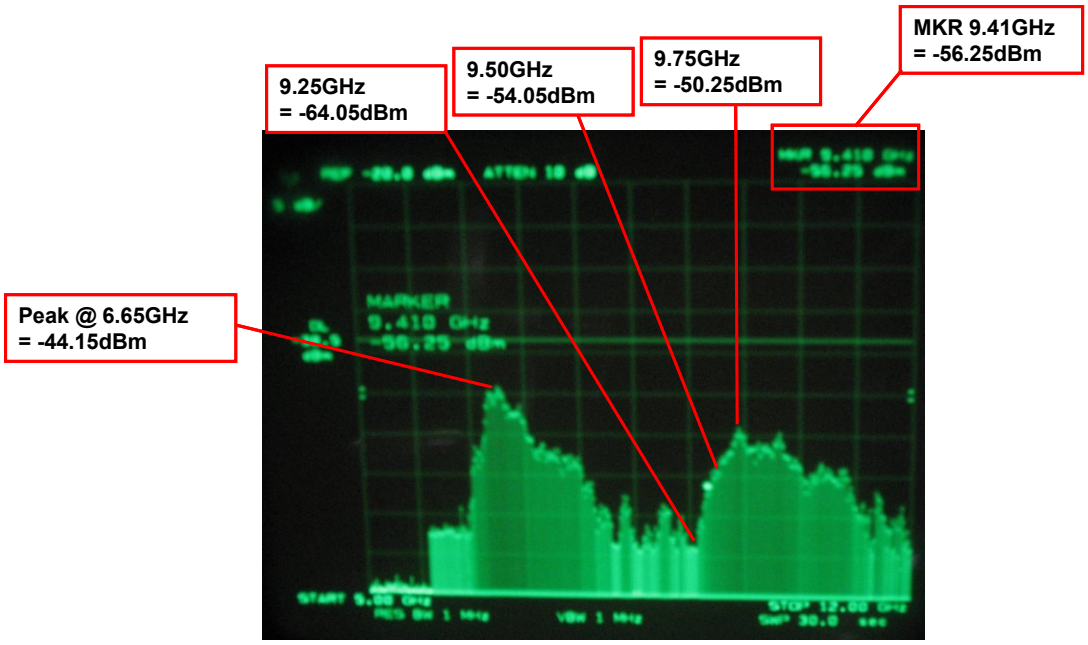

Figure 5.10: Spectrum analyzer measurement for test configuration #2: Vertically polarized source, vertically polarized receive, and WiPAA in place.

Figure 5.11 shows test configuration #3 which consists of vertically polarized source and horizontally polarized receive antenna with no WiPAA in place. The synthesizer output power is set to 0dBm. Figure 5.12 shows the measured signal strength at the receive antenna from 5GHz to 12GHz. A high level of polarization isolation is observed across the band. The response is heavily attenuated and in noise from 5GHz to 12GHz. The absolute gain at the 9.5GHz WiPAA center frequency is indistinguishable from noise at ~-60dB.

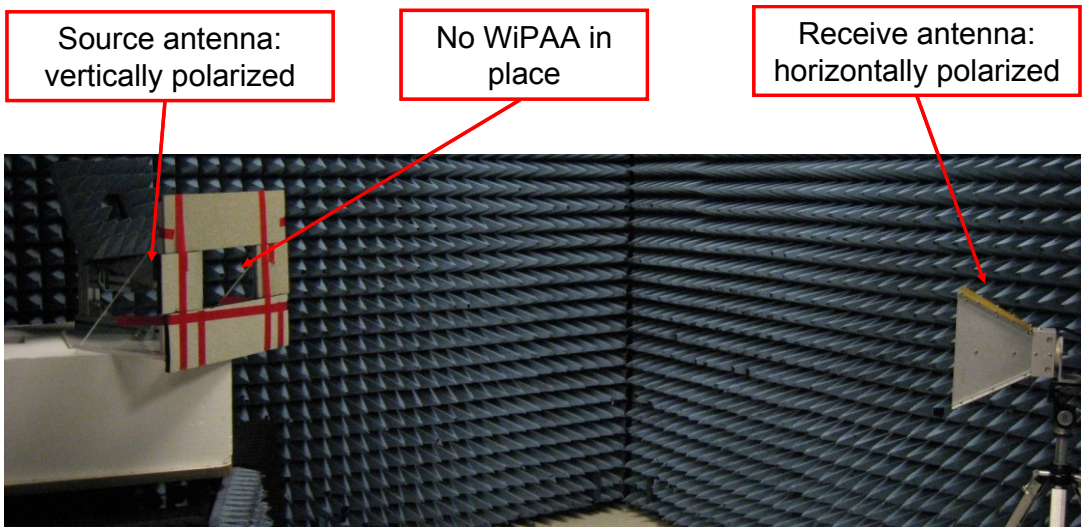

Figure 5.11: Test configuration #3: Vertically polarized source, horizontally polarized receive, and no WiPAA in place.

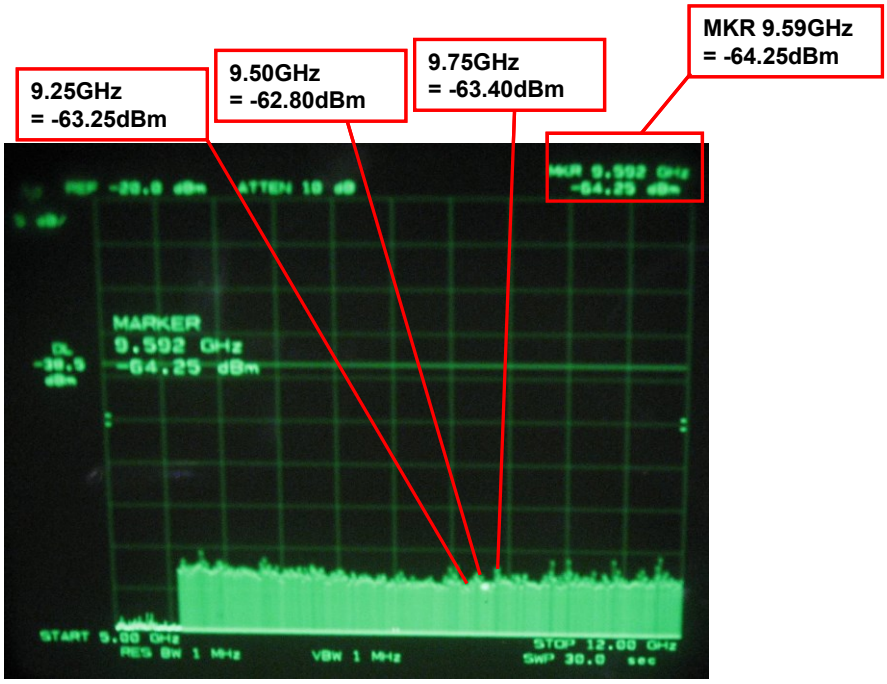

Figure 5.12: Spectrum analyzer measurement for test configuration #3: Vertically polarized source, vertically polarized receive, and WiPAA in place.

Figure 5.13 shows test configuration #4 which consists of vertically polarized source and horizontally polarized receive antenna with WiPAA in place. The synthesizer output power is set to 0dBm. Figure 5.14 shows the measured signal strength at the receive antenna from 5GHz to 12GHz. The presence of the WiPAA creates a bandpass region with peak absolute gain -37.95dB at 9.59GHz and -3dB bandpass region from 9.25 to 9.75GHz. The response is heavily attenuated elsewhere in the measurement range. The absolute gain at the 9.5GHz WiPAA center frequency is -38.45dB.

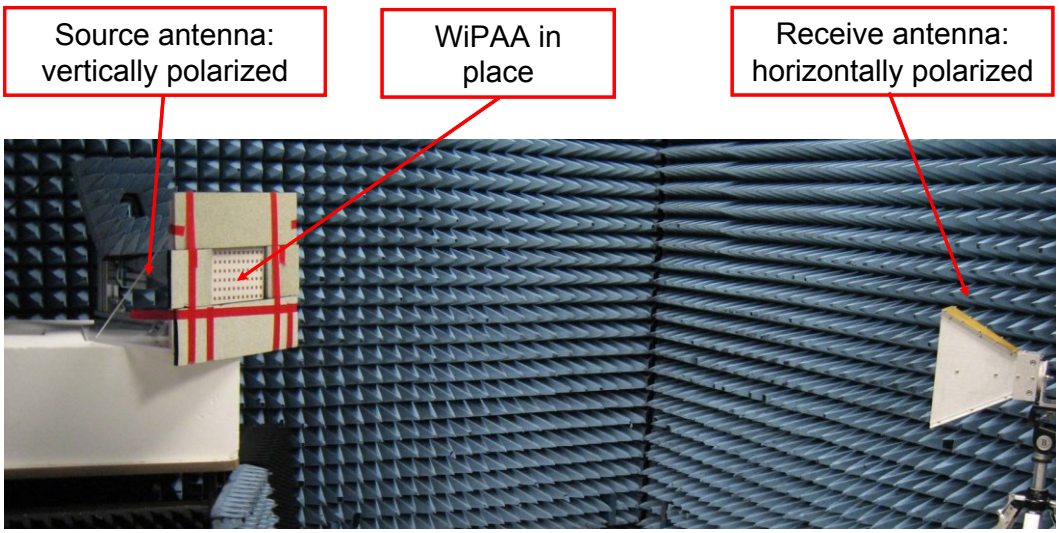

Figure 5.13: Test configuration #4: Vertically polarized source, horizontally polarized receive, and WiPAA in place.

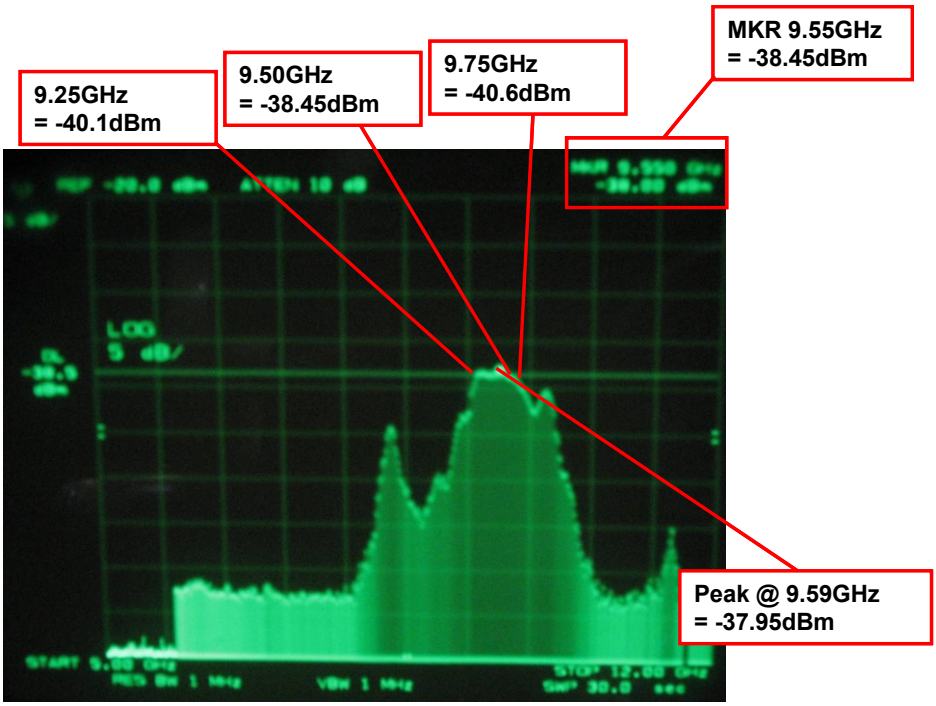

Figure 5.14: Spectrum analyzer measurement for test configuration #4: Vertically polarized source, vertically polarized receive, and WiPAA in place.

Recall that we calculated a source illumination normalization factor of -.78dB. Applying this correction, the absolute gain for test configuration #4 across the target WiPAA band is:

Source normalized absolute gain @ 9.25GHz ➔ -40.10dB – (-.78dB) = **-39.32dB**

Source normalized absolute gain @ 9.50GHz ➔ -38.45dB – (-.78dB) = **-37.67dB**

Source normalized absolute gain @ 9.75GHz ➔ -40.60dB – (-.78dB) = **-39.82dB**

Using the measurement from test configuration #1 we find the relative gain of the WiPAA test article:

WiPAA relative gain @ 9.25GHz ➔ -39.32dB – (-36.70dB) = **-2.62dB**

WiPAA relative gain @ 9.50GHz ➔ -37.67dB – (-35.85dB) = **-1.82dB**

WiPAA relative gain @ 9.75GHz ➔ -39.82dB – (-36.00dB) = **-3.82dB**

Using the sample points at low, mid, and high frequencies of WiPAA band it appears the relative gain varies from -1.82dB to -3.82dB. This implies that, for instance at 9.5GHz, 1.82dB of loss is unaccounted for when WiPAA is used instead of directly coupling source antenna to receiver. This loss may come from misalignment in fabrication and/or mismatch at WiPAA elements as a result of detuning. The difference may also come from a faulty assumption that the physical extent of the surface of the WiPAA panel is roughly equal to the effective aperture of the unfocused array of patch elements. Future tests to better clarify the results may include: x-ray imagery of the array to determine the quality of layer alignment and/or more detailed simulations of the source/array interaction to determine the precise amount of coupling into the WiPAA feed side elements.

Chapter 6: A 4-ELEMENT 1D ELECTRONICALLY SCANNED WIPAA

A 4x1 array is created using the aperture technologies discussed in chapter 3 and with the C-Band rectifier and wireless control protocol discussed in chapter 4. The purpose of this prototype is to demonstrate a steerable space-fed lens antenna that is powered and controlled with a wireless signal. The prototype consists of two adjacent WiPAA unit cells (as defined in Figure 4.5) and contains all of the necessary wireless control circuitry needed to collimate and electronically steer a beam using a wireless signal.

6.1 Design and layout of 4x1 array

In this prototype Rogers 4350 substrate is used rather than the Rogers 6002 substrate because of restrictions with the chosen PCB manufacturer. The small difference in relative dielectric constant (ε_r = 3.4 vs 2.9) may result in a subtle shift of resonant frequency but the concept can still be demonstrated.

The wireless control circuitry used in the 4x1 prototype includes a 1-stage Dickson-style rectifier, threshold detector, and MSP430 MCU. The prototype also includes 4 Hittite X-Band phase shifters in 4mm^2 surface mount packages. Figure 6.1 shows a CAD drawing of the 4x1 array with all layers visible. The wireless control circuitry and X-Band phase shifters are all attached directly to the PCB adjacent to the X-Band antenna feed (purple layer in CAD drawing). The chips are attached using a combination of reflow and hand-solder techniques. Figure 6.2 shows the fabricated 4x1 array with the 4 phase shifter modules attached but without the components for the rectifier attached. The fabricated antenna is shown partially assembled and is missing the patch superstrate layer. The patch superstrate layers, which constitute the top and

bottom layers of the antenna, only cover a portion of the total PCB area. This 'strip' assembly technique is useful because it allows SMD devices to exist on a lower layer without the need for machined rebates in the superstrate. The effect on RF performance from truncated substrate is expected to be minimal because most of RF energy in the radiator is contained in the field distributed immediately below the patch. This negligible effect from substrate truncation was confirmed in simulation. Figure 6.3 shows a close up of 2 elements of the 4x1 array once the patch superstrate layer has been attached.

An assessment of the material densities and thicknesses used can give an estimate of the total mass density of an array constructed in this fashion. The array consists of two layers of Rogers 4350 material (density = 1.86 g/cm^3) and two layers of Rogers 6002 (density = 2.1 g/cm^3). The total volume of 4350 required per square meter of array is $624cm^3$ while the total volume of 6002 required is $368cm^3$ (when dielectric superstrate is just in the region of the patch). The resulting mass density of the array including just the board materials is $1.93kg/m^2$. Using rough estimates for the mass of other key components (copper, components, silkscreen, and adhesive) we expect the total mass density of an array constructed in this fashion to be 3-$5kg/m^2$.

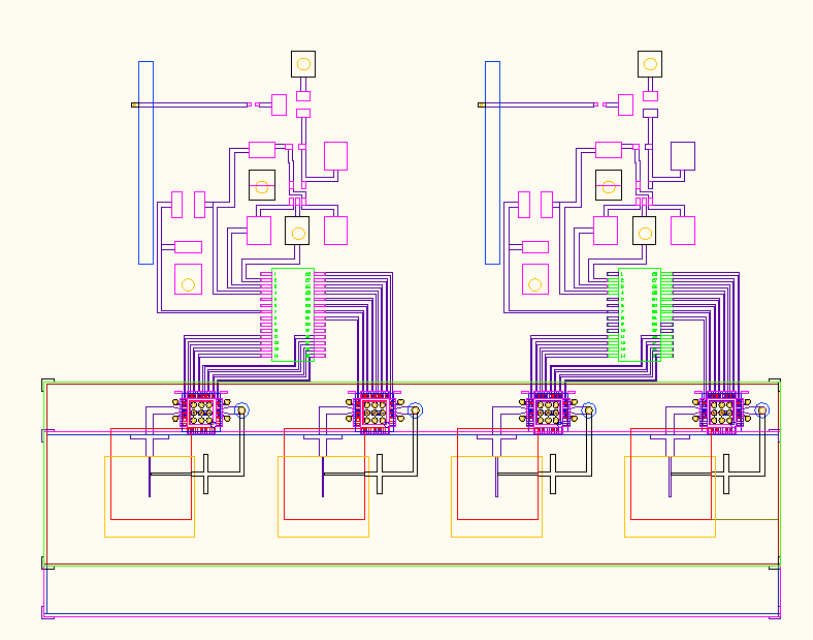

Figure 6.1: CAD drawing of 4x1 prototype antenna.

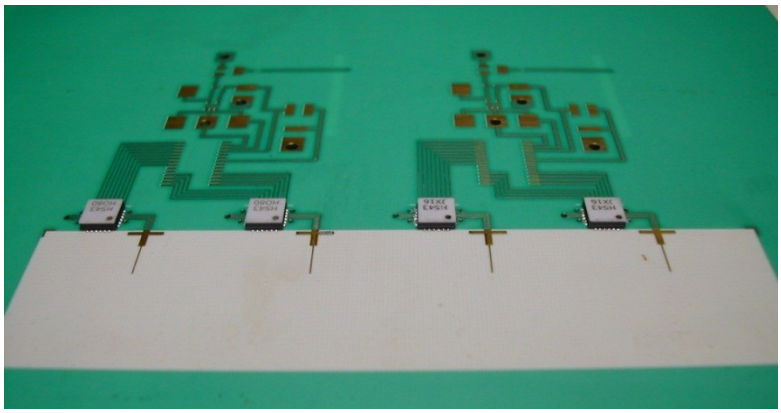

Figure 6.2: Partially assembled 4x1 WiPAA prototype with phase shifters attached

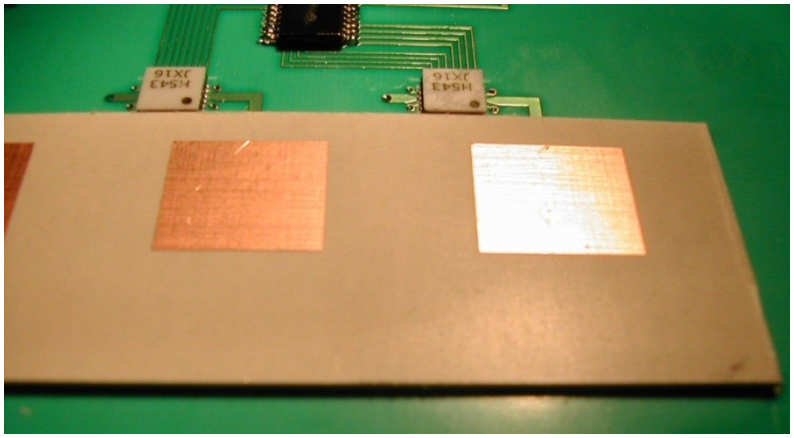

Figure 6.3: Fabricated 4x1 WiPAA prototype with patch superstrate attached

6.2 Communication protocol for beam steering

For this prototype system we are using linear progressive phase delay for beam steering and so a 4-bit word is sufficient to distinguish the 16 unique beam positions. The 4-bit word is bookended with a preamble (101010) and postamble (1011) to ensure successful transmission of the entire word. The received word is given as an input to the MCU which controls each of the two X-Band phase shifters in each WiPAA unit cell via an 8-bit control bus. The 4-bit word is interpreted as a multiple of the phase shifter LSB (in this case 22.5°) at the MCU for each unit cell and the correct position-dependent phase shift is determined.

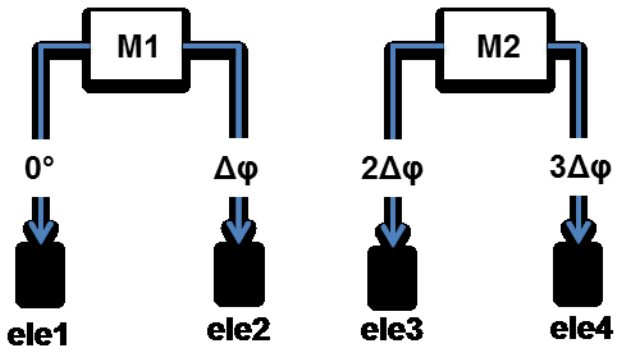

Figure 6.4: Functional diagram showing the relationship between Δφ and the element-wise phase delay.

6.3 Preliminary testing

The 4x1 array is tested in various stages. First the rectifier/demodulator is tested to ensure there is sufficient voltage to power on the MCU and that the A/D converter is producing a readable bit stream. Figure 6.5 shows the smoothed output of the 1-stage rectifier when the array is presented with a modulated RF carrier at 5.8GHz from some distance above the surface. The result is a steady voltage differential of nearly 3V with the RF ground at the highest potential. Figure 6.6 shows the input to the op-amp inverter (operating as a threshold detector). Figure 6.7 shows the output of the threshold detector when presented with the signals in Figures 6.5 and 6.6; this data stream is fed into the MCU. The test data confirms that the bits are of sufficient magnitude to convey the digital data to the MCU and we can proceed with the test confident that the MCU is receiving data.

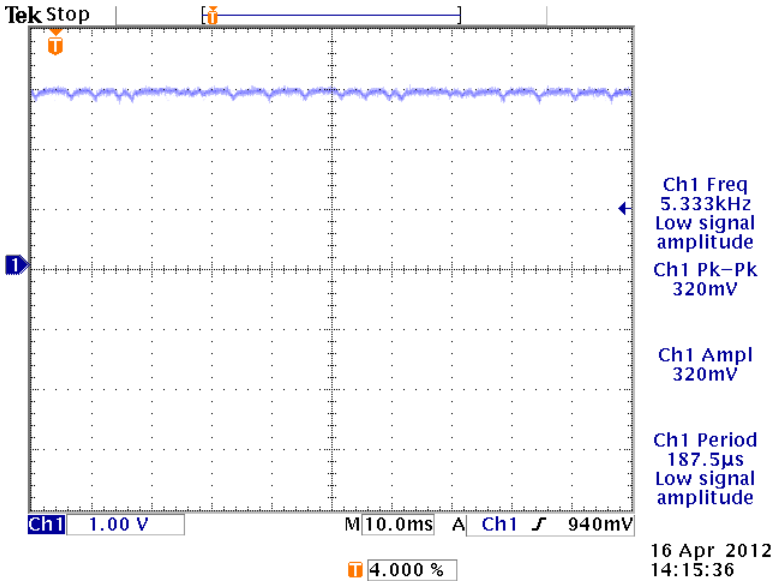

Figure 6.5: Smoothed output of 1-stage rectifier when illuminated with AM 5.8GHz source.

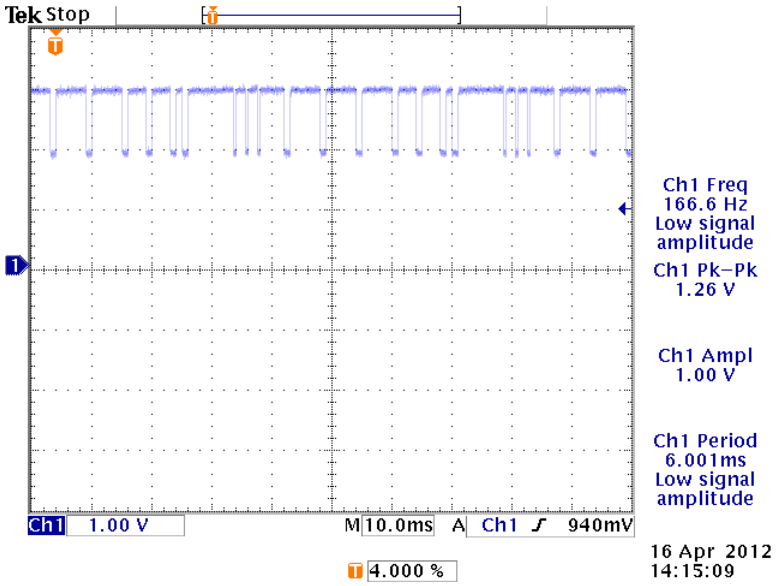

Figure 6.6: Non-smoothed output of 1-stage rectifier when illuminated with AM 5.8GHz source.

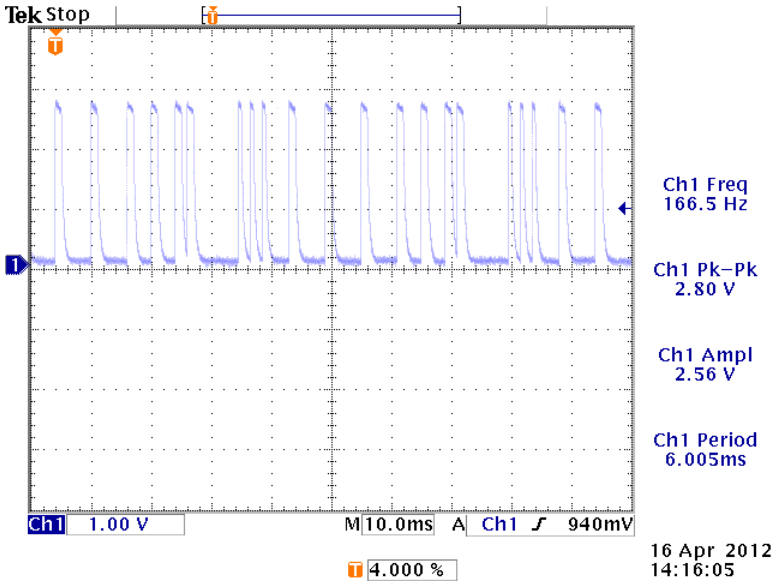

Figure 6.7: Output of threshold detector when presented with the two signals in Figures 6.5 and 6.6.

6.4 Beam steering test and analysis

Because of initial problems with the antenna measurements the patterns were taken with the 5.8GHz rectifier by-passed and a direct data signal into the MSP430. It was later determined that the problem was in the code on the MSP430 and the data will be repeated once the wireless circuitry is re-enabled. Figure 6.8 shows the pattern test configuration from the space side looking towards the array. The 4x1 antenna is embedded in absorber to minimize leakage of feed side signal around the edges of the array. This improves the effective signal to noise ratio of the measurement and produces more accurate data.

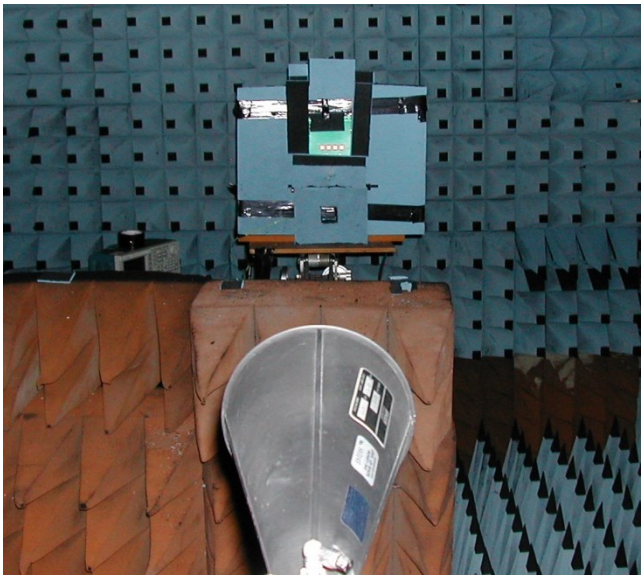

Figure 6.8: Array pattern test configuration as seen from space side.

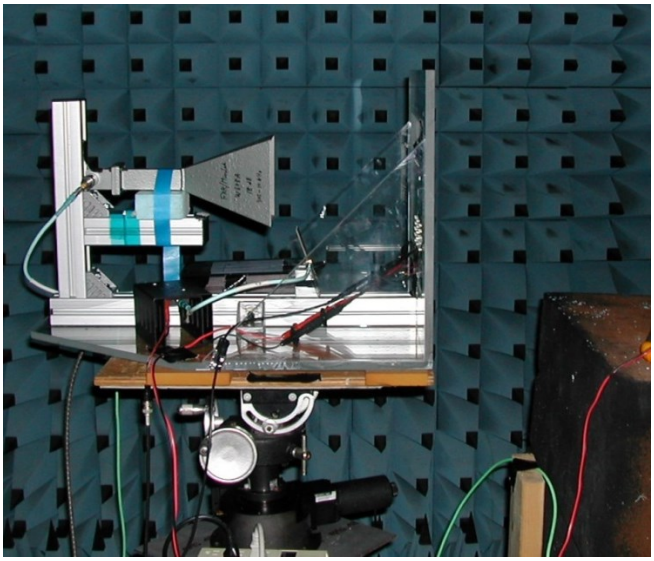

Figure 6.9: Feed side of WiPAA test fixture

Figure 6.9 shows the feed side of the WiPAA test fixture with the absorber removed. The X-Band feed antenna is a pyramidal horn separated some distance from the face of the feed side WiPAA patch elements. In testing this distance is usually small (4-8”) to minimize leakage around the test coupon and to maximize conveyed through the array to the space side receive antenna.

Figure 6.10 shows measured and simulated radiation patterns for the 4x1 space-fed array with 0° phase delay at each element. This is achieved by propagating the 4-bit word “0000” to each MCU on the test PCB. It is important to note that in this and subsequent plots both measured and simulated plots are normalized to the peak gain.

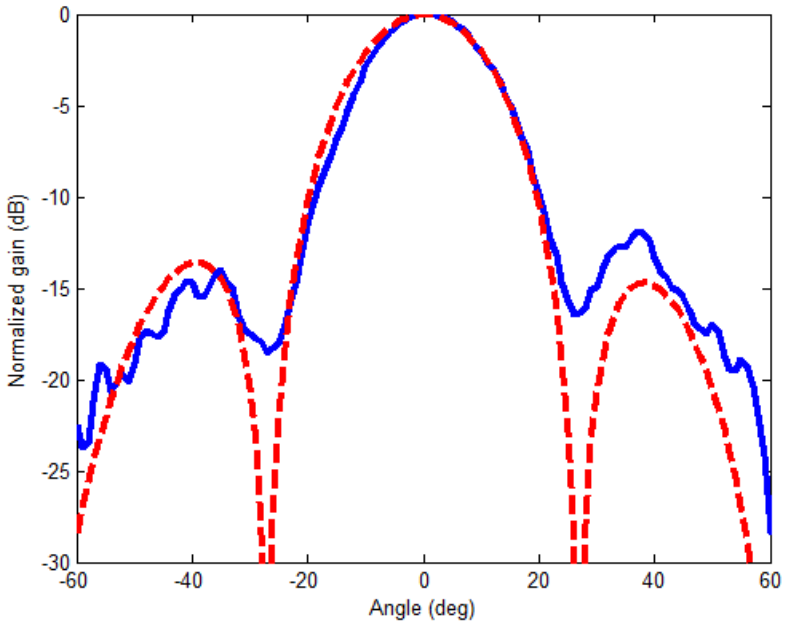

Figure 6.10: Measured vs. Simulated for $\Delta\varphi = 0°$ linear progressive phase shift.

Figure 6.11 shows measured and simulated radiation patterns for the 4x1 space-fed array with 22.5° linear progressive phase delay across the 4 elements of the array. This is achieved by propagating the 4-bit word “0001” to each MCU on the test PCB.

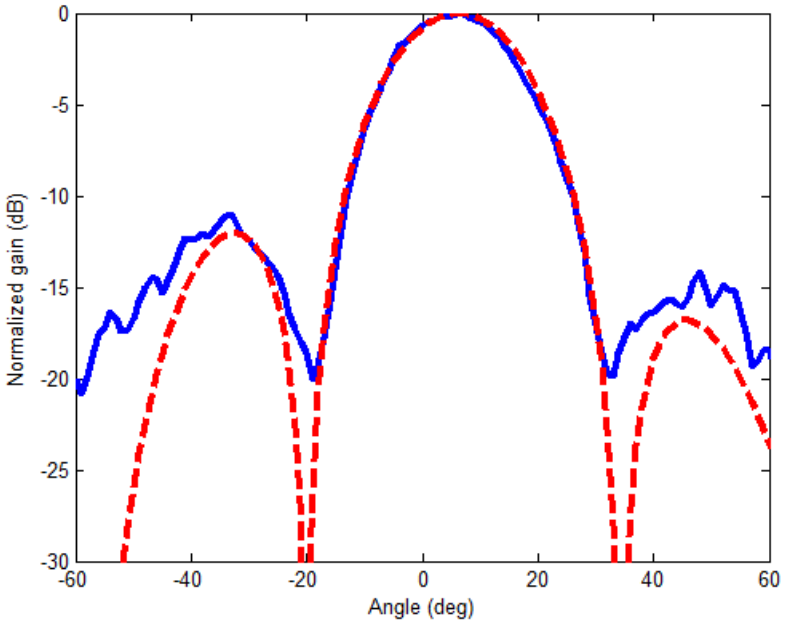

Figure 6.11: Measured vs. Simulated for Δφ = -22.5° linear progressive phase shift.

Figure 6.12 shows measured and simulated radiation patterns for the 4x1 space-fed array with 45° linear progressive phase delay across the 4 elements of the array. This is achieved by propagating the 4-bit word “0010” to each MCU on the test PCB.

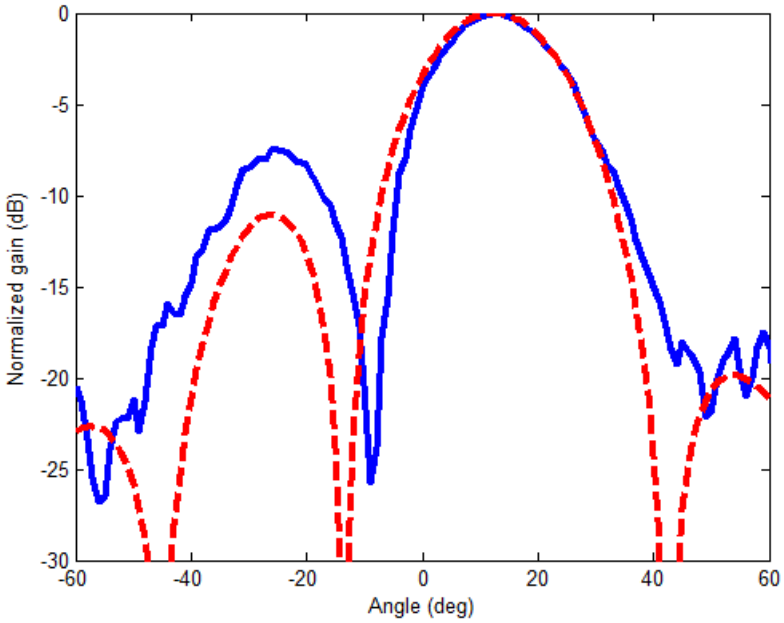

Figure 6.12: Measured vs. Simulated for $\Delta\varphi = -45°$ linear progressive phase shift.

Figure 6.13 shows measured and simulated radiation patterns for the 4x1 space-fed array with 67.5° linear progressive phase delay across the 4 elements of the array. This is achieved by propagating the 4-bit word "0011" to each MCU on the test PCB.

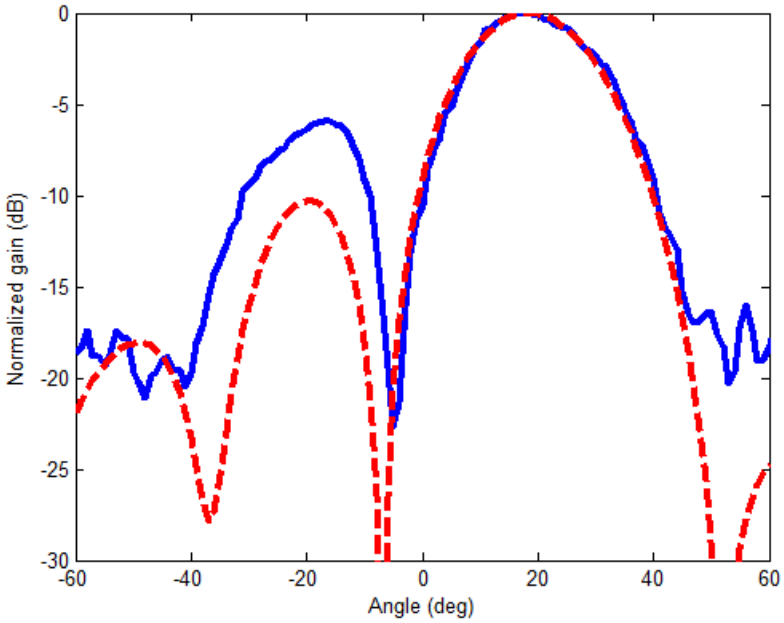

Figure 6.13: Measured vs. Simulated for $\Delta\varphi$ = -67.5° linear progressive phase shift.

Figure 6.14 shows measured and simulated radiation patterns for the 4x1 space-fed array with -22.5° linear progressive phase delay across the 4 elements of the array. This is achieved by propagating the 4-bit word "0011" to each MCU on the test PCB.

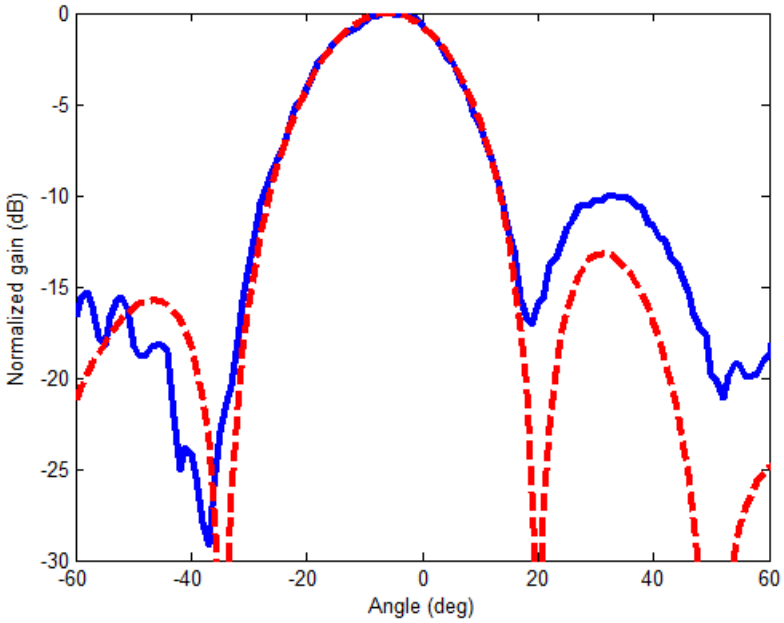

Figure 6.14: Measured vs. Simulated for $\Delta\varphi = 22.5°$ linear progressive phase shift.

In Figures 6.12 – 6.14 we observe higher than expected side-lobe levels. Although we cannot directly confirm the phase values at each element in each state we expect that one or more phase errors are manifested in the results. An error of this type has multiple possible sources: error in net phase delay produced by the phase shifters, manufacturing differences in the feed structures, or deflection of the array surface out of plane. In practical array systems phase errors are common and the impact is minimized with calibration procedures. Despite the observed errors, the results show clearly beam mobility resulting in a unique beam position for each state.

Chapter 7: CONCLUSIONS AND FUTURE WORK

7.1 WiPAA project summary

A prototype space-fed phased array antenna operating at X-Band was developed and demonstrated. The aperture is constructed in a way that minimizes the total number of PCB layers and has a mass density in the range of 3-5kg/m^3 which is much lower than many alternative PAA construction techniques. Using additional apertures and a microcontroller a 5.8 GHz signal was used to wirelessly power and command the operation of the phased array. The results show that a phased array antenna can be successfully steered in this manner. The transmit power required to turn on and control the phased array was relatively large making the design suitable for applications where enabling large area apertures is more important that absolute power consumption of the system. One example of such an application is a very large array to focus energy from a solar power satellite. In any space-based system there are significant trade-offs between the size, weight, and power consumption of an antenna. While this project address improvements in the size and weight of large-area antennas implementation of this technology may come at the expense of total power consumption. Future work will focus on reducing the board area of the RF rectifier and demodulator so that a 2D phased array antenna can be constructed. Future work will also focus on utilizing the wireless nature of the PAA unit cells to enable unique construction techniques that can create a large scale folding arrays.

7.2 Future development of WiPAA technology

Reduction of component footprint

The development of smaller more integrated electronics is the next logical step in maturing WiPAA technology and is necessary in implementing a grating lobe free scanning 2D array. The

area available per unit cell for circuitry (using the current WiPAA topology) is approximately 18mm^2 (6mm x 3mm). If the topology proposed by Duffy is successfully implemented, this area could be increased to roughly 60mm^2 (6mm x 10mm) [29]. X-Band phase shifters are currently available in two small integrated circuit package sizes from supplier Hittite Microwave Corp 1mm x 2.5mm x .1mm and 3.25mm x 1.9mm x .1mm. The MSP430F2112 microcontroller used in the 4x1 prototype array is available in a 9.8mm x 6.6mm x 1.2mm surface mount packages or a 5.8mm x 5.8mm x .8mm QFN package. It is clear that if two phase shifters and one MSP430F2112 (in QFN package) are used in each WiPAA unit cell the available area is nearly used up. The level of integration will ultimately need to be high to implement the phase shifters, MCU, wireless receiver, and wireless power harvesting circuitry on a single layer.

The prospect of assembling WiPAA unit cell electronics in an area less than 18mm^2 (current technology) and 60mm^2 (upper limit on available unit cell area) using the smallest components available and both sides of the PCB for chip attach needs to be examined. This study would likely include analysis of a more compact X-Band probe feed as well as simulations assessing the impact of component nearness to radiating elements. Once the X-Band antenna design is chosen the remaining surface area can used for component placement. Additionally, a study on the available receiver/control IC (MCU) technologies is needed. This study would seek the smallest commercially available component with the requisite functionality.

Detailed simulation and analysis of 2D WiPAA

The ultimate aim of WiPAA technology is a scanning space-fed 2D array without electrical interconnects between elements. The elimination of electrical interconnects allows for the creation of a large area aperture that can be folded or disassembled for storage or transportation.

To demonstrate the distinct benefit of WiPAA technology a detailed design of a 2D scanning array needs to be performed. This effort would include a detailed CAD drawing sufficient to create a working scanning space-fed array. One idea to realize a bendable structure is to add a thin layer of flexible plastic (PVF, LCP, PTFE, or similar) in between the two interior PCB layers (distribution layers) to function as a backing sheet. The remaining PCB layers (distribution and patch layers) would be scored/routed along the rows and/or columns so the entire sheet could be compacted, for instance by rolling around a cylinder of some appropriate diameter.

The simulations of the capacitively coupled element used in the prototype WiPAA did not include potential effects from neighboring elements. To ensure good RF performance, detailed simulations of a WiPAA unit cell should be performed. The simulation should include the infinite array boundary condition to ensure optimal performance of the element in the array environment. The scan performance of the antenna can be simulated by varying the phase delay across the problem boundaries along orthogonal lattice vectors. This simulation can be done using Ansoft HFSS and a 3D CAD model of the WiPAA unit cell.

Wireless power transfer efficiency study

The 4x1 prototype WiPAA antenna demonstrated major limitation of the concept. In the test environment the antenna requires around 1mW of received power to generate enough voltage to turn on the MCU. It was difficult to attain a consistent measure of maximum allowable separation between source and receiver because of near-field effects and the presence of absorber but in practice this distance was often quite small (~5” or so) even though the transmitted power was quite high (2W RF at the source antenna). Before the WiPAA is considered for use in space-based systems the maximum wireless power transfer efficiency should be determined and if it is

found to be insufficient alternative methods of conveying power to the unit cell electronics should be considered.

Part II. Temperature rise in objects due to optical focused beam through atmospheric turbulence near ground and ocean surface

Chapter 8: INTRODUCTION

8.1 History of study of laser propagation through atmosphere and laser heating of objects

When a high power optical beam is propagated through atmospheric turbulence and is incident on an object, power is transferred, causing the temperature of the object to rise. Recent demonstrations by the Navy show a multi-kilowatt beam igniting the engine housing of a small boat from over 1 km distance in a maritime environment [37]. Interest in this technology motivates the investigation of turbulence effects on beam wave propagation and its impact on target heating. Laser beam propagation through the atmosphere in the presence of turbulence has been studied extensively [38] [39]. The US Navy has developed HELCAP (High Energy Code for Atmospheric Propagation), a 3D code to model high energy laser propagation, and published many papers based on the results [40] [41] [42]. The basic problem of laser induced heating of a variety of solid objects has been studied [43] [44] [45]. Many of the studies of laser heating to this time have been performed in the context of laser machining and without regard to a large volume of turbulent media between transmitter and solid object. While these studies give useful results for the laser power and dwell times common in laser machining these parameters do not generally translate well to the problem of a laser beam propagated over a large distance through the atmosphere. In these cases spot sizes are generally larger and dwell times generally longer. This paper provides a prediction of temperature rise due to a high power optical emitter operating over a large distance in a variety of plausible atmospheric conditions. To predict heating of solid objects due to the incident laser, beam wave propagation, optical absorption, and heat diffusion are simultaneously considered. For a beam wave in turbulence, a statistical model

is used to obtain the second moment which is the long term average intensity. For short pulse durations, on the order of 10 ms or less, the fourth order moment is also obtained. A beam of sufficiently high power density causes heating of the atmosphere and non-linear propagation, or thermal blooming, of the beam. The threshold transmit power beyond which thermal blooming has a discernible effect on the characteristics of the optical beam are readily estimated for each considered scenario. A discussion of possible implications of exceeding this threshold follows. For transmit powers below the threshold, thermal blooming effects are disregarded. The beam wave is incident on the object and power is absorbed causing a net heating of the material. To quantify the absorbed power the optical absorptivity of the object must be determined. We assume optical absorption in the form of intrinsic bulk absorption. For metallic objects a Drude model is used to find the complex dielectric constant of the object at the desired optical frequency. For non-metals, published optical absorptance values are used. The net temperature rise at the object surface is calculated using a thermal diffusion model, appropriate boundary conditions, and the bulk thermal characteristics of the target material. A flow chart of the process is provided in Figure 8.1.

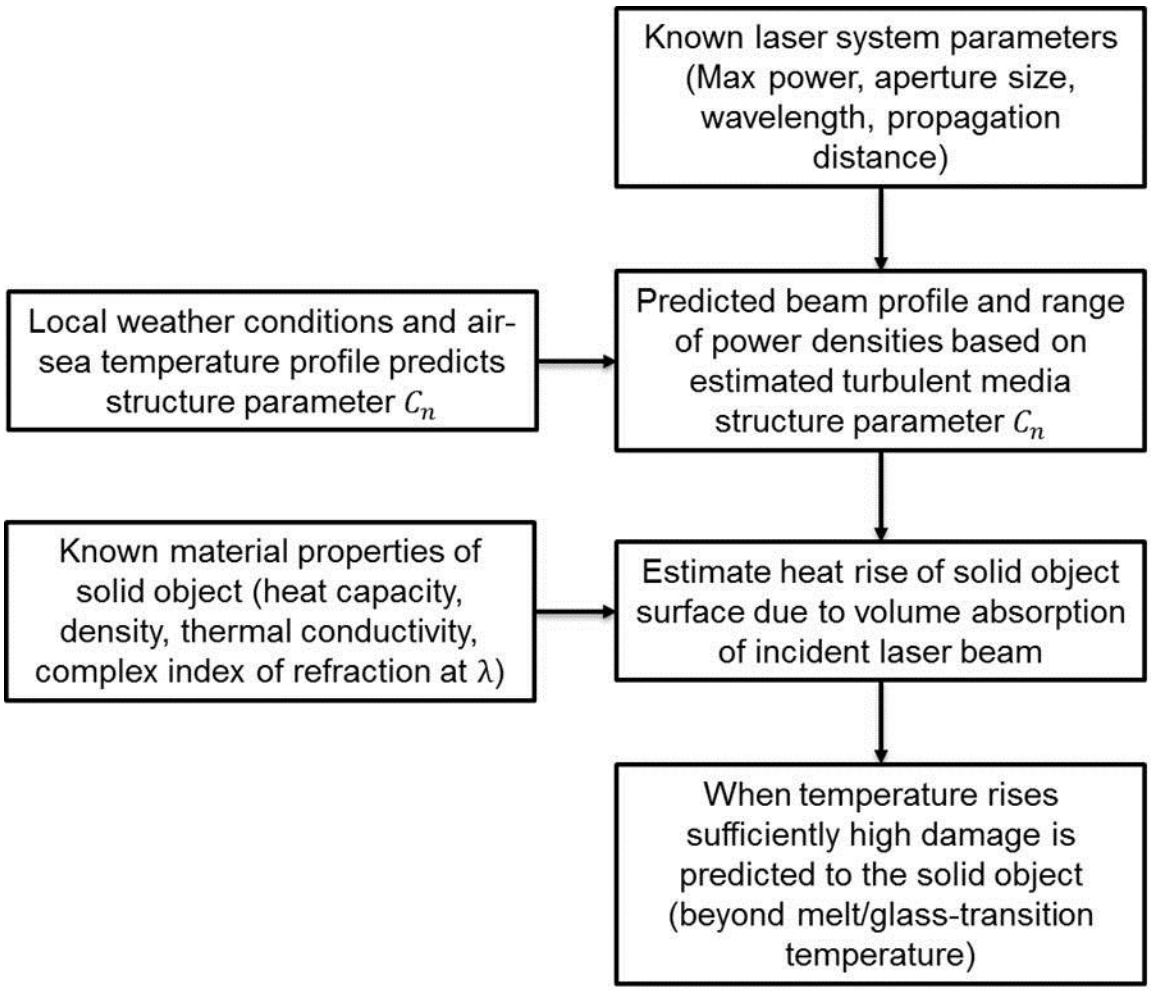

Figure 8.1: Flow chart of laser heating of solid object through turbulence calculation.

Chapter 9: LASER BEAM IN ATMOSPHERE

9.1 Focused beam through turbulence

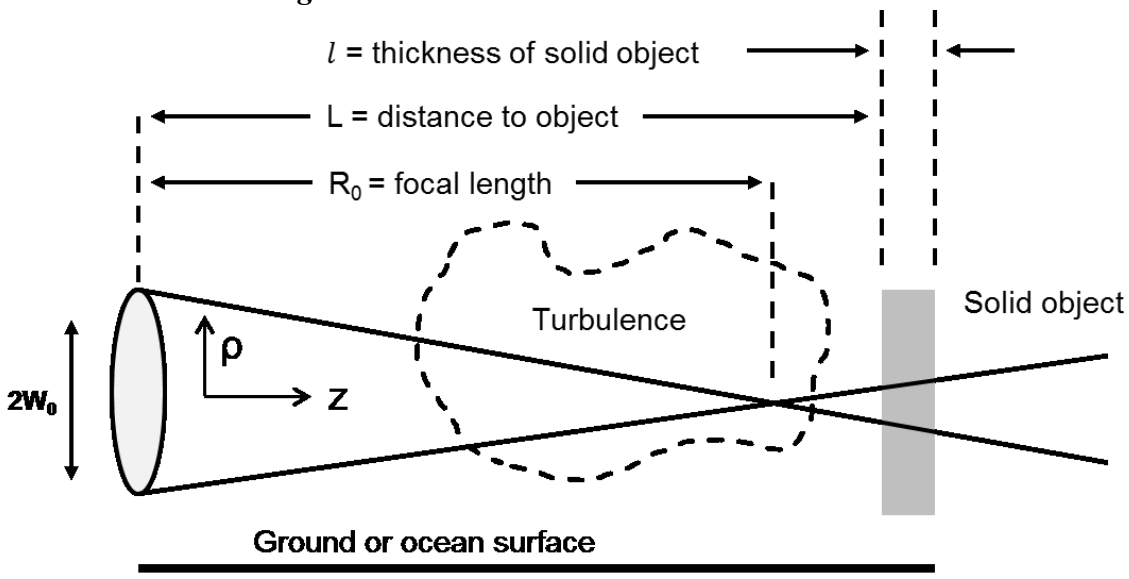

Figure 9.1: Focused optical beam and solid object target

The expression for an optical focused beam in free space as shown in Figure 9.1 is given by [46].

$$U_0(\rho,z)=\frac{A_0}{(1+i\xi z)}exp\left[ikz-\left(\frac{k\xi}{2}\right)\frac{\rho^2}{(1+i\xi z)}\right] \tag{1}$$

Where ξ is given by:

$$\xi=\xi_1+i\xi_2=\frac{1}{z_0}+i\frac{1}{R_0} \tag{2}$$

z_0 is called the "Rayleigh range" and gives an approximate dividing distance such that the field is considered in the "near field" for $z < z_0$. The Rayleigh range is a function of wavenumber k and aperture radius W_0:

$$z_0 = \frac{kW_0^2}{2} \tag{3}$$

R_0 is the focal distance. The field at $z = 0$ has Gaussian amplitude and a focused phase front. Fig. 1 shows the focused beam in atmospheric turbulence and a target. We define the total input power at $z = 0$, and amplitude constant A_0 as:

$$P_t = \left(\frac{\pi}{2} W_0^2 \right) A_0^2 \tag{4}$$

$$A_0^2 = \frac{|E|^2}{2\eta_0} \tag{5}$$

The intensity distribution of a focused beam in the turbulence has been obtained and in the range $z_i \gg z \gg z_c$, where z_i and z_c depend on the inner scale l_0 and outer scale L_0 of the turbulence:

$$z_i = \left(0.39 C_n^2 k^2 l_0^{5/3}\right)^{-1} \tag{6}$$

$$z_c = \left(0.39 C_n^2 k^2 L_0^{5/3}\right)^{-1} \tag{7}$$

The intensity distribution is given by [46] [47]:

$$I\left(\rho_c, z\right) = A_0^2 \frac{2W_0^2}{W^2} \exp(-\alpha_E z) \int_0^\infty t J_0\left(t\rho'\right) exp\left[-t^2 - \left(\frac{1}{2}\right) D_s t^{5/3}\right] dt \tag{8}$$

Where $\rho' = \frac{\left(2\sqrt{2}\right)\rho_c}{W}$, α_E is the atmospheric attenuation constant, and where the structure function D_s and beam size W are given by:

$$D_s = 6.2 C_n^2 k^{1/3} z^{8/5} W^{-5/3} \tag{9}$$

$$W^2 = W_0^2\left[\left(\xi_1 z\right)^2 + \left(1-\xi_2 z\right)^2\right] \tag{10}$$

The atmospheric attenuation constant α_E accounts for the absorption and scattering properties of the medium. Values for α_E are widely known and reduction of laser transmittance due to atmospheric attenuation for distances $<1km$ in relatively clear air is minimal [48]. In the numerical calculations that follow $\alpha_E = 0$ is assumed unless otherwise specified.

The index of refraction structure constant C_n^2 has been found in the range 10^{-17} (very weak) to 10^{-12} (very strong) over land and 10^{-16} (weak) to 10^{-13} (strong) over the open ocean [47] [49]. The coherent intensity of the beam wave is given by [46]:

$$\left|U\right|^2 = \frac{W_0^2}{W^2} exp\left(-\frac{2\rho^2}{W^2} - 2a_0 z\right) \tag{11}$$

Where the constant of attenuation due to turbulence α_0 is:

$$\alpha_0 = 0.39 C_n^2 k^2 L_0^{5/3} \tag{12}$$

These expressions can be used to model the intensity of an optical beam through turbulence at the location of a distant target.

9.2 Special consideration for short-term intensity

For a short term on the order of 10 *ms* or less, the peak intensity is approximately close to the speckle intensity. In this context, speckle refers to the amplitude variations in the laser spot caused by constructive/destructive interference from incident rays of varying phase. When the laser dwell time is sufficiently short the interference pattern is essentially static and the use of the average intensity to determine peak intensity is not appropriate. The fourth order intensity I^2 can be approximately given by the following, using "circular complex Gaussian assumption":

$$I^2 \approx 2I^2 - |U|^4 \tag{13}$$

Under this approximation, we get a short-term intensity Eq. (14a) whereas when the time is not short we use the average intensity Eq. (14b).

$$I_{short} \approx \left[2I^2 - |U|^4 \right]^{1/2} \tag{14a}$$

$$I \approx \left[I^2 - |U|^4 \right]^{1/2} \tag{14b}$$

Using Eqs. (14a) & (14b) we can calculate the intensity of the laser beam at the object surface. In the numerical examples, 14a is used for pulse durations less than 10 *ms* and 14b is used for pulse durations greater than or equal to 10 *ms*. This arbitrary choice of a short pulse cutoff results in a small discontinuity in the incident flux at 10 *ms*.

9.3 Thermal blooming in the atmosphere

The air in the atmosphere has some absorption at optical wavelengths. The absorption of power produces a local heating, increasing the pressure and decreasing the density which causes a decrease of the refractive index. The beam intensity profile is initially maximum on the axis but as the heating occurs the refractive index decreases on the beam axis which causes a divergence of the beam from the beam axis. This is referred to as thermal blooming of the beam [50]. Thermal blooming has been studied numerically and analytically using geometric optics, perturbation theory, and extended Huygens-Fresnel methods. If multiple pulses are used, the wind moves the minimum refractive index away from the beam axis and the new pulse will be focused into the upstream direction of the wind and the center of the beam moves toward the axis giving enhancement of the peak power on the axis. The peak power can then become higher than the free space peak power. Numerical examples in [50] show that the peak power can be enhanced by 17%.

If we make a few assumptions about the conditions of operation we can use an order-of-magnitude expression, following the lead of [50], to estimate the onset of thermal blooming effects. We first assume the beam wave is propagated through some transverse flow of velocity v and that the air has some absorption coefficient α that contributes to local heating of the propagation medium. From [50] we can estimate the minimum transmit power level at which thermal blooming effects may be significant:

$$P_{min} \approx \frac{\rho_0 \lambda \gamma \pi v W_0}{\alpha_E L (\gamma - 1)(n_0 - 1)} \tag{15}$$

If we assume the constants are (typical values for sea level air):

γ is the heat capacity ratio; γ = 1.4 for air at 20°C

n_0 is the initial index of refraction; $(n_0 - 1) = 3 \times 10^{-4}$ for air

ρ_0 is the ambient pressure; $\rho_0 = 10^5 \, Nm^{-2}$ at sea level

α_E is the atmospheric extinction coefficient; $\alpha_E = 4 \times 10^{-4} \, m^{-1}$ for tropical air in rural environment [48].

λ is the wavelength of radiation; $\lambda = 10^{-5} \, m$

v is the velocity of the transverse flow; $v = 13.6 ms^{-1}$ about 30 *mph*

W_0 is the radius of the aperture; $W_0 = 0.05m$

L is the propagation distance to the target; $L = 0.5 \times 10^3 \, m$

Then we find that the threshold power is approximately:

$$P_{min} \approx \left(2.9 \times 10^7\right) \frac{\pi v W_0}{L} \approx 120 kW$$

The order of magnitude calculation shows that for the power densities considered in this analysis it requires transmit power in excess of the upper limit of most CO_2 laser systems to encounter

thermal blooming effects. Additionally, this calculation did not consider the effect of atmospheric turbulence which will, in general, further reduce the radiation power density along the path of the beam wave.

Chapter 10: INTERACTION OF LASER AND SOLID OBJECTS

10.1 Absorbed power in the object

An optical beam is incident on the object and power is dissipated into the medium as heat which will raise the temperature. The power transmitted into the object L_a can be calculated:

$$L_a = \frac{\omega \varepsilon_0 \varepsilon'}{2} |E_i|^2 = L_{a0} \exp(-\alpha_2 z_2) \tag{16}$$

The dielectric constant of the object is $\varepsilon(\omega) = \varepsilon^{'} + i\varepsilon^{"}$ and the attenuation in the object is given by:

$$\alpha_2 = 2Im(k_2) \tag{17}$$

where $k_2 = \omega\sqrt{\mu\varepsilon}$. The transmitted electric field into the object at a distance z_2 from the incident surface is given by:

$$E_t(z_2) = TE_i \exp(ik_2 z_2) \tag{18}$$

where T is the transmission coefficient. If we consider a metallic object, the dielectric constant at optical wavelengths is given by a Drude model:

$$\varepsilon(\omega) = 1 - \frac{\omega_p^2}{\omega\left(\omega + i\frac{1}{\tau}\right)} \tag{19}$$

where ω_p is the plasma frequency and τ is the relaxation time. For copper, the plasma frequency and relaxation time were determined in [51] [52] [53]. Using the most recent number, the value of ε is computed:

$$\varepsilon_{copper} = -8.04 \times 10^3 + i1.85 \times 10^3 \tag{20a}$$

For many non-metals, the optical constants in the mid-infrared have been directly observed. The relative permittivity of water at $10.6\mu m$ has been determined [54]:

$$\varepsilon_{water} = 1.21 + i0.02 \tag{20b}$$

The complex index of refraction of polyimide at $10.6\mu m$ has been published; from this the relative permittivity is computed [55]:

$$\varepsilon_{PI} = 3.23 + i0.18 \tag{20c}$$

Glass-fiber reinforced plastic (GFRP) is a mixture of glass fibers in a thermally cured plastic resin (e.g. polyesters) background material. Properties of GFRP including volume fraction of glass fiber, melting temperature of resin, and typical thermal properties are described in [56]. The complex index of refraction of silica glass at $10.6\mu m$ has been published; from this the relative permittivity is computed [57]:

$$\varepsilon_{glass} = 3.75 + i2.0 \tag{20d}$$

The complex index of refraction of polyethylene at $10.6\mu m$ has been published; from this the relative permittivity is computed [58]:

$$\varepsilon_{PE} = 2.25 + i0.0025 \tag{20e}$$

The dielectric properties of composite materials such as GRFP have been studied extensively at microwave frequencies using different mixing formulas [59]. At $10.6\mu m$, the size of glass inclusions in polymer resin background material are usually much larger than the wavelength and these mixing formulas may not be applicable. Therefore, in this paper, we use a simple average of Eqs. (20d) and (20e) to obtain a rough estimate of the GFRP permittivity.

10.2 Heat diffusion in solid objects

The absorbed power is given by Eq. (16), which will be the heat source for the temperature rise. The diffusion equation for the temperature is given by:

$$\frac{\partial T}{\partial t} = D\nabla^2 T + \frac{L_a}{\rho C_s} \tag{21}$$

Where T is the temperature, ρ (kg/m^3) is the density, C_s ($J/kg°C$) is the specific heat of the solid, and D (m^2/s) is the thermal diffusivity. The thermal properties for the 4 materials under consideration are summarized in Table 10.1.

Table 10.1: Thermal properties of various laser targets

Material	$\rho\ (\frac{kg}{m^3})$	$C_s\ (\frac{J}{kg°C})$	$D\ (\frac{m^2}{s})$	$\tau_\delta\ (s)$	$\frac{\tau_l}{3}(s)$
Copper	8.92×10^3	0.39×10^3	1.12×10^{-4}	7.6×10^{-13}	2.9×10^{-5}
Water	1.00×10^3	4.18×10^3	1.44×10^{-7}	6.0×10^{-2}	2.3
Polyimide [60]	1.42×10^3	1.09×10^3	7.75×10^{-8}	9.0×10^{-4}	1.1×10^2
Glass/resin composite [56]	1.90×10^3	1.00×10^3	3.20×10^{-7}	2.8×10^{-5}	1.1×10^2

Equation (21) needs to be solved with boundary conditions. A commonly used approximate boundary condition is the Neumann condition:

$$\frac{\partial T}{\partial n} = 0 \tag{22}$$

This is equivalent to zero heat flow across the boundary. This boundary condition is appropriate when the heat transfer from the solid object to the surrounding media is low (i.e. a relatively good thermal conductor in still air). The thermal time constant τ_δ for a skin depth δ_s determines the approximate time required for heat generated by the conversion of laser energy in the skin depth region to diffuse a distance greater than the thickness of the skin depth region.

$$\delta_s = \frac{1}{\alpha_2} \tag{23a}$$

$$\tau_\delta = \frac{\delta_s^2}{D} \tag{23b}$$

If the laser is incident on the target for a short time relative to the skin depth of the material the heat diffusion will be approximately given by [61]:

When t is in the range $\left(t \le \tau_\delta\right)$:

$$\Delta T(0,t) \approx \frac{L_a t}{\rho C_s} \tag{24}$$

Assuming heat has diffused out of the skin depth region, for relatively short times the heat will have not yet diffused far enough to reach the back surface of the metallic object located at $z_2 = l$. This time is determined by the thermal time constant:

$$\tau_l = \frac{l^2}{D} \tag{25}$$

In this time interval heat diffuses as it would in a semi-infinite metallic object and a Neumann boundary condition is assumed at $z_2 = 0$ only. With this assumption, the temperature rise, ΔT, at $z_2 = 0$ is given by [61].

When t is in the range $\left(\tau_\delta \ll t \leq \frac{\tau_l}{3}\right)$:

$$\Delta T(0,t) \approx \left(\frac{2\delta_s L_a}{\rho C_s l}\right)\left(\frac{\tau_l t}{\pi}\right)^{1/2} \tag{26}$$

For relatively long times the heat will have diffused through the thickness of the object and a Neumann boundary condition assumed at both $z_2 = 0$ and $z_2 = l$. With these assumptions, the temperature rise, ΔT, at $z_2 = 0$ is given by [61].

When t is in the range $\left(\frac{\tau_l}{3} \leq t\right)$:

$$\Delta T(0,t) \approx \left(\frac{\delta_s L_a}{\rho C_s l}\right)\left(t + \frac{\tau_l}{3}\right) \tag{27}$$

Chapter 11: NUMERICAL EXAMPLES

11.1 Attenuation due to turbulence

We consider a beam focused on a solid copper object of thickness $l = 0.1\ mm$. Figure 11.1 shows the predicted minimum laser dwell time required to heat the surface of the copper target to the melting point of copper using 10.6 μm radiation through a focused 5 *cm* aperture at 0.5 *km*. Although in practice it may be difficult to focus a laser at a distance of 0.5 *km* we use the focused case to illustrate the worst-case degradation due to turbulence. The effect of turbulence on a collimated beam is less pronounced and thus the result will be closer to the free-space solution. The transmit power is varied from 10-100 *kW* and various cases of atmospheric turbulence are considered: free space (no turbulence), turbulence $C_n^2 = 10^{-14}$, turbulence $C_n^2 = 10^{-13}$, turbulence $C_n^2 = 10^{-12}$. For the thickness of copper and time range considered, eq. (27) is used exclusively as heat has diffused a distance much greater than the thickness of the copper target.

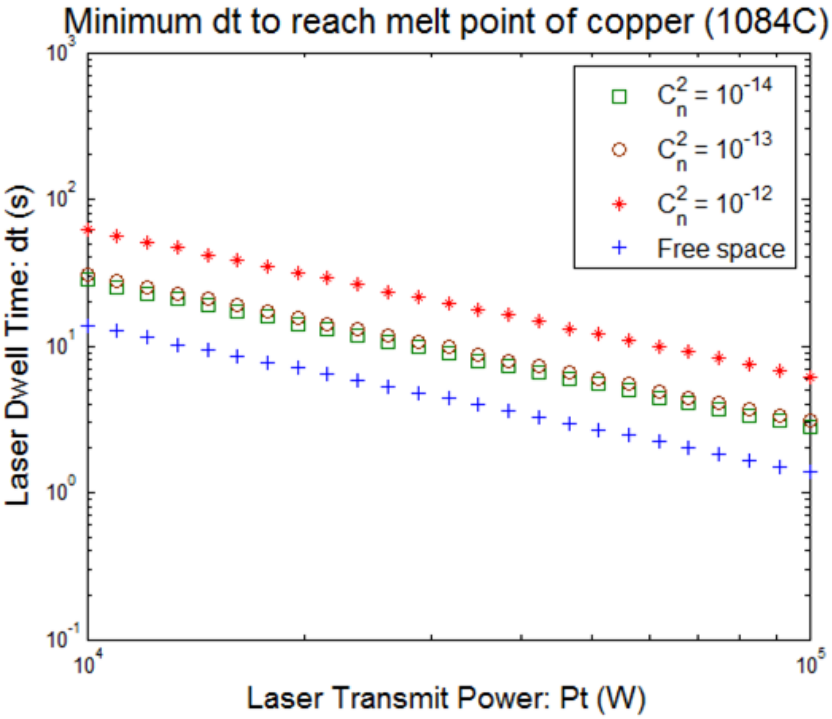

Figure 11.1: ΔT vs. *Pt* at λ = 10.6 *μm*; L = 0.5 *km*; A_0 = 5 *cm* (focused); P_t = 10-100 *kW*; copper thickness *l* = 0.1 *mm*.

The plot in Figure 11.1 can be used to predict the laser dwell time required to realize the onset of melting for a laser system of known transmit power. This result considers only when the absorbed power is sufficient to cause a sustained rise in temperature in excess of the melt temperature it applies generally to either pulsed or continuous wave (CW) operation provided that the average power is held constant (e.g. 10-100 *kW*). In pulsed operation the beam will have a higher power density and thus may cause a momentary spike in local temperature above the melt temp but during the off portion of the duty cycle the heat will diffuse out of the area and the temperature will decrease. Over many pulses the average temperature will rise at the same rate as a CW laser of equal average power.

Figure 11.2 shows the predicted minimum laser dwell time required to heat the surface of a l = 10 *mm* sample of Kapton (polyimide) target the glass transition temperature (400°C) using 10.6 μm radiation through a focused 5 *cm* aperture at 0.5 *km*. The transmit power is varied from 10-100 *kW* and various cases of atmospheric turbulence are considered: free space (no turbulence), turbulence $C_n^2 = 10^{-14}$, turbulence $C_n^2 = 10^{-13}$, turbulence $C_n^2 = 10^{-12}$. The discontinuity at $dt = 10^{-2} s$ is due to the inclusion of the fourth-order moment for short pulse durations as described in section 9.2. For the thickness of polyimide and time range considered, eq. (24) is used for $t < 9\times10^{-4} s$ and eq. (26) is used for $t > 9\times10^{-4} s$.

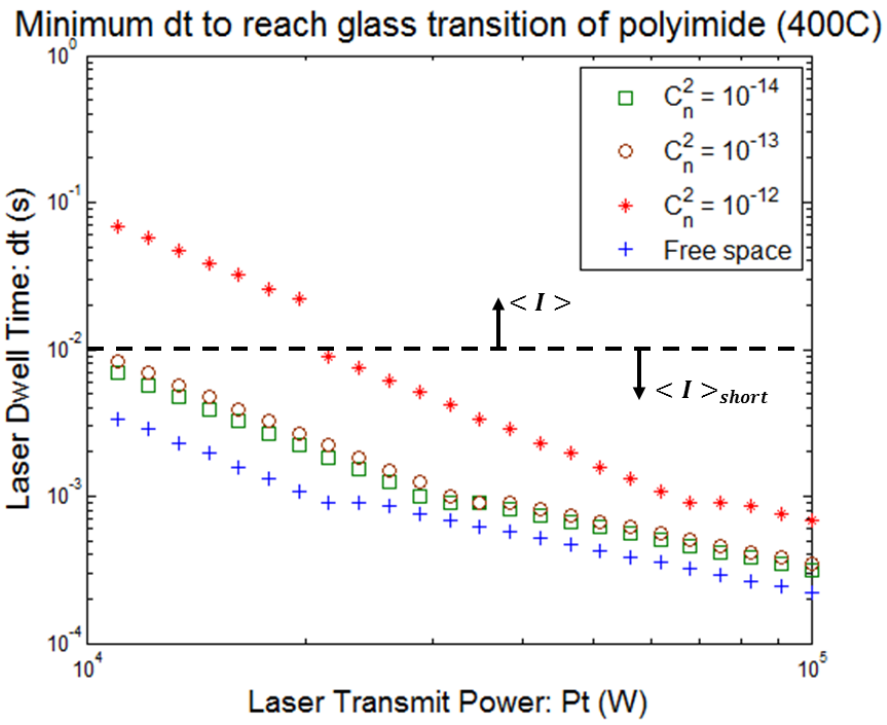

Figure 11.2: ΔT vs. *Pt* at λ = 10.6 μm; L = 0.5 *km*; A_0 = 5 *cm* (focused); P_t = 10-100 *kW*; Kapton thickness l = 10 *mm*.

Figure 11.3 shows the predicted minimum laser dwell time required to heat the surface of a l = 1 *mm* sample of water to its boiling point (100°C) using 10.6 μm radiation through a focused 5 *cm*

aperture at 0.5 *km*. The transmit power is varied from 10-100 *kW* and various cases of atmospheric turbulence are considered: free space (no turbulence), turbulence $C_n^2 = 10^{-14}$, turbulence $C_n^2 = 10^{-13}$, turbulence $C_n^2 = 10^{-12}$. For the thickness of water and power ranges range considered, eq. (24) is used exclusively as $\tau_\delta = 0.06s$ which is greater than the maximum required laser dwell time to heat water to its boiling point.

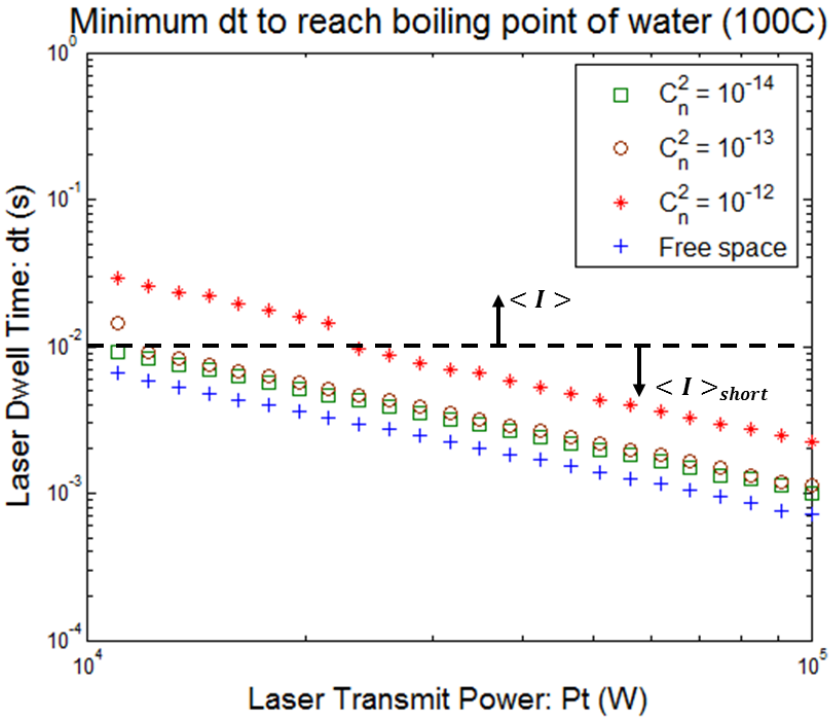

Figure 11.3: ΔT vs. *Pt* at λ = 10.6 *μm*; L = 0.5 *km*; A_0 = 5 *cm* (focused); P_t = 10-100 *kW*; Water thickness *l* = 1 *mm*.

Figure 11.4 shows the predicted minimum laser dwell time required to heat the surface of a *l* = 10 *mm* sample of GFRP to the melting point of polyester resin using 10.6 *μm* radiation through a focused 5 *cm* aperture at 0.5 *km*. The transmit power is varied from 10-100 *kW* and various cases of atmospheric turbulence are considered: free space (no turbulence), turbulence $C_n^2 = 10^{-14}$, turbulence $C_n^2 = 10^{-13}$, turbulence $C_n^2 = 10^{-12}$. For the thickness of GFRP and power ranges range

considered, equation (26) is used exclusively as the required laser dwell times fall between $\tau_\delta = 2.8\times10^{-5}\,s$ and $\frac{\tau_l}{3} = 1.1\times10^{2}\,s$.

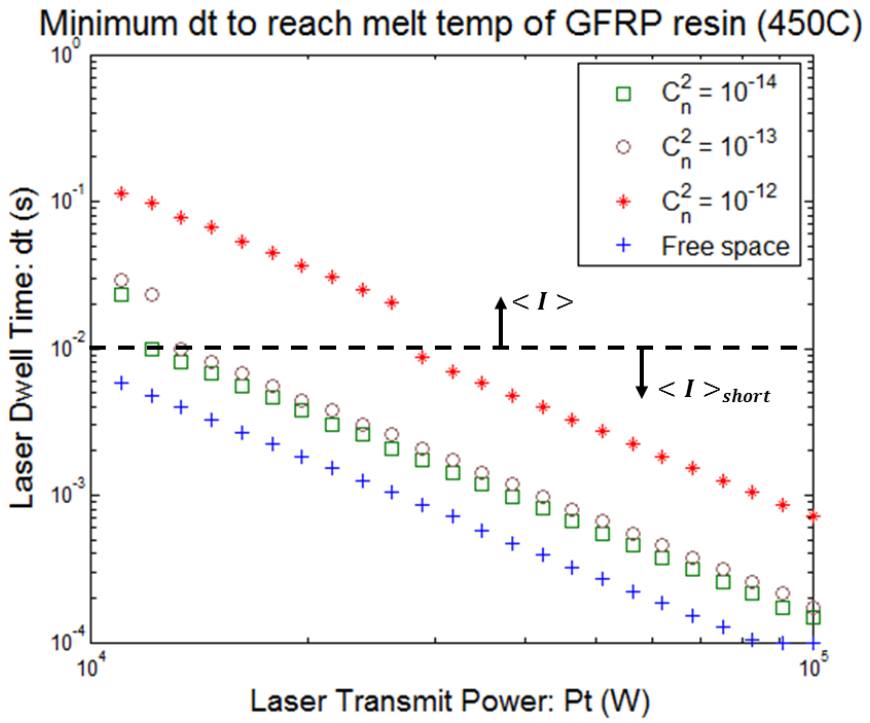

Figure 11.4: ΔT vs. *Pt* at λ = 10.6 *μm*; L = 0.5 *km*; A_0 = 5 *cm* (focused); P_t = 10-100 *kW*; GFRP thickness *l* = 10 *mm*.

11.2 Attenuation due to turbulence and atmospheric extinction

The combined effect of atmospheric scattering and attenuation on a laser beam propagated through the atmosphere to a solid object target is a reduction in transmittance which can, under the right conditions, become similar to or even greater in magnitude than the interference caused by atmospheric turbulence. Like the attenuation caused by atmospheric turbulence, the total extinction seen in a volume of atmosphere increases with the greater separation between the laser source and the target. This is easily deduced from eq. (8) which contains the exponential

attenuation term $\exp(-\alpha_E z)$. The product of extinction coefficient and linear distance is commonly called optical thickness: $\tau_E = \alpha_E z$. An order-of-magnitude approximation is that the effect of atmospheric extinction should be considered when optical thickness τ_E ‰l. For a distance of 0.5km this corresponds to α_E ‰2km^{-1}. Figure 7 shows the effect of atmospheric extinction in this range on the laser dwell time required to heat a copper target to its melting point. Considering the free space (no turbulence) case we can observe an increase in minimum laser dwell time when $\alpha_E = 2km^{-1}$ which is in the range of the increase required in moderate turbulence. If optical thickness τ_E □ the increase in laser dwell time will be minimal and if τ_E □ the effect of atmospheric extinction will dominate and the relative effect of turbulence will be small.

Figure 7 shows the effect of $\alpha_E = 2km^{-1}$ on laser propagation over 500m. In real-world conditions this value of atmospheric extinction is not typical when visibility is relatively good. According to [48], for visibility ranging from hazy to clear (5km - 40km) atmospheric extinction remains below $\alpha_E = 0.33km^{-1}$ in a rural non-maritime environment. According to [26], the atmospheric extinction coefficient for a maritime environment at 99% relative humidity is $\alpha_E = 0.45km^{-1}$. In the presence of fog, however, when visibility can be reduced to 50-1000m atmospheric extinction in the range $\alpha_E = 1-100km^{-1}$ can be expected. This is shown in a number of fog model calculations in [62] [63].

Chapter 12: CONCLUSIONS AND FUTURE WORK

12.1 Project summary

This project concerns the study of an optical beam propagated through turbulence and incident on various targets, generating heat and causing a temperature rise. The propagation of a beam wave in the atmosphere is discussed including the fourth order moment and the effect of thermal blooming. Transmitted power of $10-100\,kW$ is absorbed in the target and converted into heat causing the temperature to rise. Numerical examples are given for $10.6\,\mu m$, free-space and turbulence, aperture size $W_0 = 5\,cm$, copper target thickness of $0.1\,mm$, Kapton target thickness of $0.1\,mm$, water thickness of $1\,mm$, and GFRP thickness of $10\,mm$ In each case the beam is focused at $0.5\,km$ and the minimum laser dwell time required to heat the sample to its melting/boiling point is predicted. The effect of atmospheric extinction through absorption and scattering is discussed and it is determined that the attenuation due to atmospheric extinction should be included in a dwell time calculation when τ_E ‰l. A plot is presented which shows the predicted difference in required dwell time for a focused laser through the atmosphere in zero and moderate turbulence with $\tau_E = 0$ and $\tau_E = 1$.

12.2 Future work and model verification

Future work in this area will be focused on expanding the application of the temperature rise estimation technique to cover a more diverse array of environments and conditions and verifying the accuracy of the computational model using either simulation or experimental results. For certain situations including high-power density lasers, low transverse flow velocity (low wind), and highly absorptive atmospheres thermal blooming may also become important and its inclusion in the laser power transfer model will need to be investigated.

Part III. A steerable 60GHz array antenna using a continuously variable dielectric phase shifter

Chapter 13: INTRODUCTION

13.1 History of 60GHz communication and technologies

The unlicensed spectrum around 60GHz is becoming increasingly interesting for wireless communication applications because of the potential to realize high throughput data links. The 60GHz band allows up to 7GHz of spectral bandwidth making it ideal for high data rate commercial communications systems [64]. There are standards in place for 60GHz communication including WiGig which has support for phased array antenna beamforming [65]. Phased array antennas are a natural fit for many applications in this design space because of the increased spatial diversity and range obtained through directional communication. Recently, a number of phased array modules and system-in-package arrays for 60GHz have been created [66] [67] [68]. Good electrical performance of CMOS devices at 60GHz has been shown however the module assembly is generally quite complex motivating a simpler beam steering solution.

A 60GHz reconfigurable dielectric phase shifter has the potential to make low cost V-band phased array antennas realizable by eliminating the need for solid state or MEMS devices. The phase shifting concept is based on previous work at lower frequencies [69] [70]. For this effort, a 60GHz reconfigurable dielectric phase shifter is examined. The reconfigurable dielectric phase shifter relies on the ability to obtain a specific effective permittivity on a length of transmission

line using movable dielectric slabs. To maintain sufficient range in effective permittivity when using widely available ceramic composites as dielectric slab materials, the phase shifting transmission line was designed on low-permittivity Rogers Duroid 5880 (ε_r = 2.2). The relationship between ceramic slab to transmission line separation and effective permittivity is characterized and used to predict relative phase delay. Instances of both continuous and discrete slab to transmission line separation are considered. Measurements are obtained using a mm-wave module for VNA. A 3x8 element 60GHz patch array, to pair with the reconfigurable dielectric phase shifter, is designed and simulated. A functional phased array system with dielectric slab phase shifters is demonstrated.

Chapter 14: A DIELECTRIC SLAB PHASE SHIFTER

14.1 Principles of operation

A reconfigurable dielectric phase shifter is essentially a movable or variable superstrate for a section of transmission line. Figure 14.1 shows a diagram of the reconfigurable dielectric phase shifter including coplanar waveguide (CPW) transmission line on substrate of thickness h and dielectric superstrate separated by distance d from the top surface of the CPW. The position of the superstrate (value of d) influences both the characteristic impedance and the propagation constant of the CPW in the region immediately below the dielectric slab.

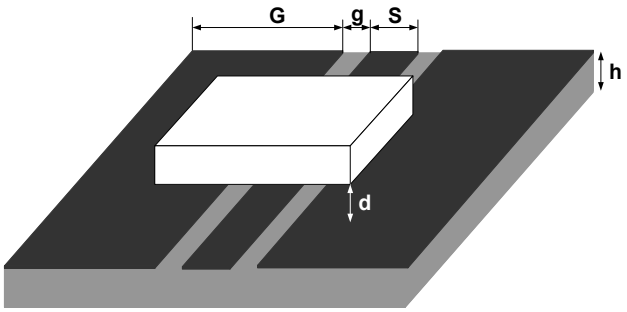

Figure 14.1: Diagram of movable dielectric slab over coplanar waveguide transmission line.

As the dielectric slab to coplanar waveguide separation is decreased ($d \rightarrow 0$) the effective dielectric constant of the transmission line begins to change. Using transmission line theory we can determine the two primary effects on the transmission path [70]. The relative phase delay θ incurred by a section of transmission line with index of refraction n_d influenced by a dielectric slab of length l at position d above a section of coplanar waveguide with nominal index of refraction n_b is given by Eqn. (1).

$$\theta = (n_d - n_b)k_0 l \tag{1}$$

We also expect the characteristic impedance (Z_1) of the l length slab altered section to scale linearly with the index of refraction of that section. The characteristic impedance of the slab section should be less than or equal to the characteristic impedance of the slab-free sections (Z_0). Equation (2) shows this relationship.

$$Z_1 = \frac{n_d}{n_b} Z_0 \tag{2}$$

One approach to introduce relative phase delay using the above guidelines is to eliminate the problem of mismatched impedance by ensuring reflections from the slab boundaries cancel. This is done by ensuring the slab section is an integer multiple of a guided wavelength. To do this the slab section must satisfy the relationship in Eqn. (3).

$$n_d k_0 l = N\pi \tag{3}$$

Both the phase shift requirement and impedance match requirement can be satisfied for a discrete set of points corresponding to slab heights d and discrete cases of phase shift can be realized (dependent on the choice of N). This is a discrete approach to phase shifter design as it provides only a limited set of realizable phase shift values for each slab type and geometry.

An alternate approach is to let the slab length l be relatively large, for instance 4λ. This will allow significant relative phase delay to be realized for relatively small differences $n_d - n_b$ (for instance θ ranges from 0 to 360 for $n_d - n_b$ from 0 to .25). By keeping the difference in index of refraction small we keep the change in characteristic impedance of the slab section small. If the difference in characteristic impedance between the slab section and the rest of the coplanar waveguide transmission line is small enough it may be ignored. By eliminating the impedance

match requirement, we can realize a continuous set of relative phase delay cases by simply satisfying the phase shift requirement. This is a continuous approach to phase shifter design as it provides, in theory, a continuous range of phase delay from 0 to some maximum phase delay which is dictated by the slab type and length of the slab.

A CPW transmission line is designed for 100Ω characteristic impedance when d is large (effectively no slab). The center conductor dimension S = 0.35mm and the gap size is g = .25mm. To maintain the maximum array column spacing sufficient to avoid grating lobes at scan the total width of the coplanar waveguide transmission line is constrained to 6.25mm which requires a ground conductor width of G = 2.7mm. The propagation constant of the transmission line is found to be β = 1558 rad/m and the relative effective dielectric permittivity is found to be ε_{eff} = 1.53. This transmission line is used to examine both discrete and continuous phase shifting techniques.

14.2 Examination of dielectric slab phase shifting at 60GHz

To examine the dielectric slab phase shifting technique at 60GHz a V-Band measurement system is constructed in which sections of CPW transmission line can be measured. Figure 14.2 shows the transmission line measurement system which consists of a 50-75GHz source coupled to one end of a CPW transmission line upon which a dielectric slab can be positioned and a 50-75GHz receive module connected to the other end. The mm-wave modules multiplies RF in the range 12.5-18.3GHz by 4 and harmonic mixers with LO of 12.5-18.3GHz are used for detecting IF (8.33MHz).

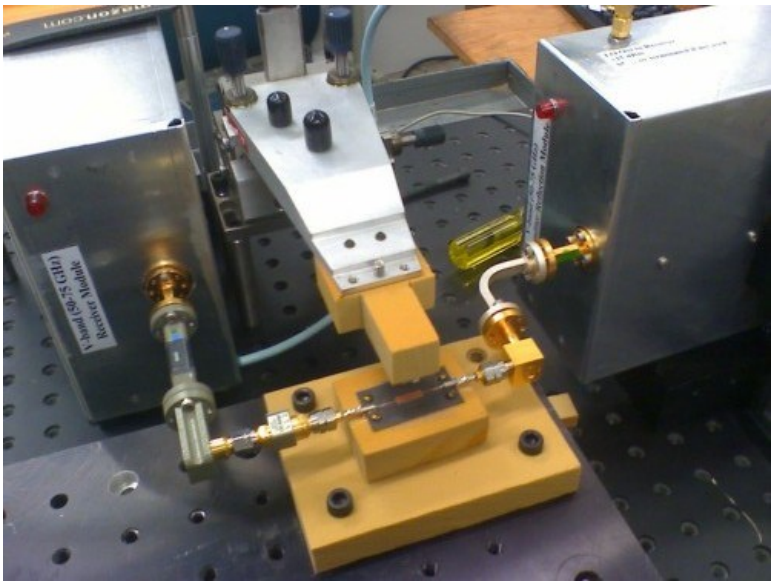

Figure 14.2: V-Band transmission line measurement system.

The measurement system is calibrated using a THRU response calibration for S_{21}. This calibration is done with no dielectric slab present and is sufficient to provide relative phase shift for cases when the dielectric slab is introduced.

To test the phase shift range of the dielectric slab technique a total of 5 different slabs are used. The slab material properties and lengths are shown in table 14.1.

Table 14.1: Measured dielectric slab samples

Sample number	Material	ε_r	Slab length	Max $\Delta\theta$ (at d = 0)	Insertion loss at d=0
1	Rogers 6002	2.94	4.9mm	70°	2.4dB
2	Rogers 6002	2.94	8mm	110°	2.9dB
3	Isola IS620	3.72	8mm	135°	1.5dB
4	Rogers 3006	6.15	10mm	220°	2dB
5	Rogers 6010	10.2	8mm	255°	9.5dB

Also shown in table 14.1 is the maximum measured phase delay for each slab. This is the phase delay, relative to no slab, that is exhibited when the dielectric slab is placed in direct contact with the CPW transmission line ($d = 0$). A z-axis positioner with micrometer accuracy is used to increase the dielectric slab separation d in small increments and the relative phase delay is measured. Figure 14.3 shows the relative phase delay vs. slab height for the 4.9mm Rogers 6002 slab. Figure 14.3 also shows the result of an HFSS simulation using the same transmission line dimensions and dielectric slab material properties.

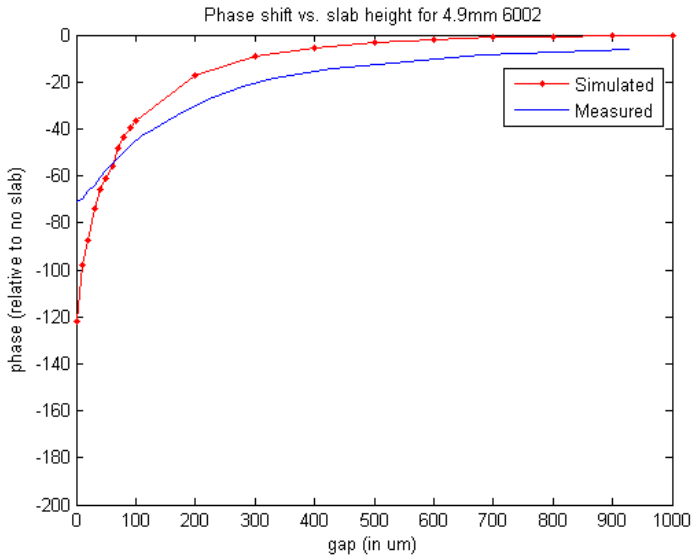

Figure 14.3: Phase shift vs. slab height for 4.9mm Rogers 6002 slab.

The measured phase delay is not in perfect agreement with the simulation, particularly for very small values of d (very small gap). This is likely because it is, in practice, difficult to achieve an ideal slab/CPW interface. Imperfections in the positioner, transmission line, or slab surface can all lead to air gaps between the slab and CPW which will reduce the effective dielectric constant and relative phase delay of the phase shifter.

Figure 14.4 shows the measured and simulated relative phase delay for the 8mm Isola IS620 slab. This slab is longer and has a higher dielectric permittivity than the 4.9mm Rogers 6002 slab and as a result exhibits increased relative phase delay over the range of slab separations tested. The slab has a maximum relative phase delay that is almost double the relative phase delay of the Rogers 6002 slab. This is useful because the more range a phase shifter provides (in general) the wider the field of view of the phased array antenna will be. As was the case with the 4.9mm Rogers 6002, the simulation overestimates relative phase delay in the very small gap region ($d < 50\mu m$).

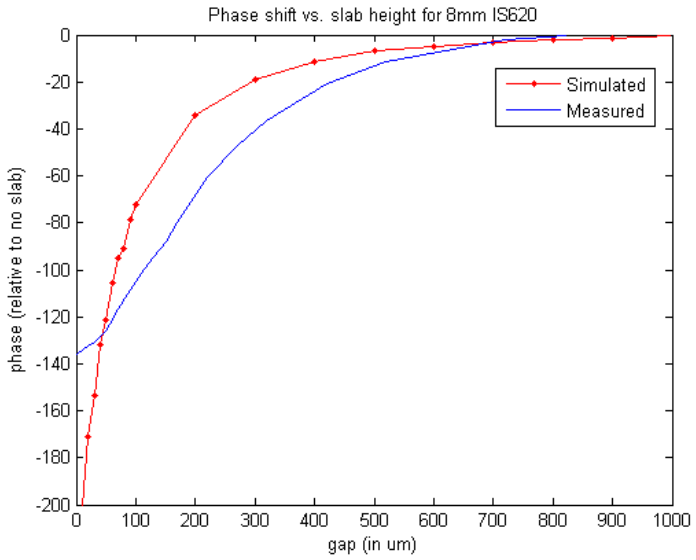

Figure 14.4: Phase shift vs. slab height for 8mm Isola IS620 slab.

Figure 14.5 shows the measured and simulated relative phase delay for the 10mm Rogers 3006 slab. This slab is longer than both the 4.9mm Rogers 6002 slab and the 8mm Isola IS620 slab. It also has a higher dielectric permittivity than both of the previous slabs. As a result the maximum relative phase delay of 220° is the largest of the three slab materials. A test was done using an

8mm Rogers 6010 slab but the measured insertion loss was much too high for the slab to be useful as a phase shifter.

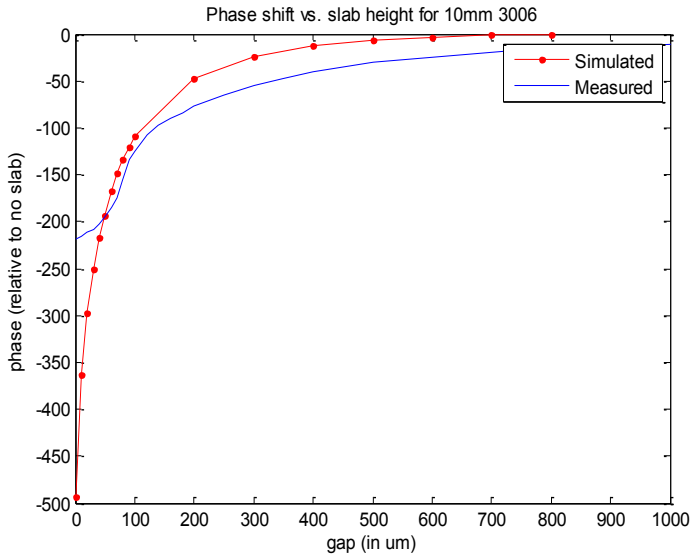

Figure 14.5: Phase shift vs. slab height for 10mm Rogers 3006 slab.

Chapter 15: A 3x8 60GHZ PHASED ARRAY ANTENNA WITH DIELECTRIC SLAB PHASE SHIFTER

15.1 Design and layout of array

To demonstrate the beam steering capability of the dielectric slab phase shifter a 3x8 60GHz array antenna is constructed with CPW feed lines. The CPW feed lines feed the series-fed arrays which constitute the columns of the array. First, a 1x8 series-fed array with 100Ω input impedance is designed and simulated in HFSS. Next, a 3-way power divider with 50Ω input and equal amplitude 100Ω output is designed and simulated. In the case of the array without CPW feed lines a triangular divider design is used [71]. Finally, the series-fed array and power divider are combined to form the 3x8 array.

Figure 15.1 shows the two fabricated 60GHz arrays. Figure 15.1a shows the fabricated fixed beam 3x8 array used to characterize the 60GHz antenna radiation pattern independent of the reconfigurable dielectric phase shifter. Figure 15.1b shows the fabricated 3x8 array with integrated reconfigurable dielectric phase shifter. In the case of Figure 15.1a each output from the 3-way power divider feeds a 1x8 series fed patch array. In the case of Figure 15.1b, the outputs of the power divider feed 3 independent CPW transmission lines. A dielectric slab phase shifter is used on transmission lines feeding columns 1 and 3 of the array and a transmission line with fixed delay (no slab) is used for column 2 of the array. The outputs of the CPW lines are then used to feed columns of 1x8 series fed arrays.

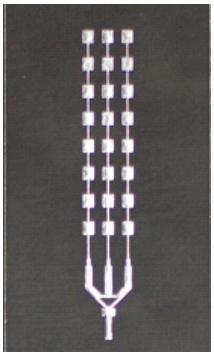

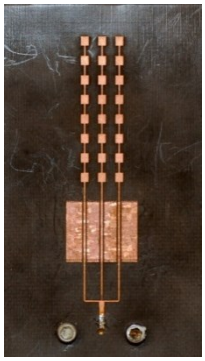

(a) **(b)**

Figure 15.1: (a) 3x8 60GHz patch array without CPW; (b) 3x8 60GHz patch array with CPW.

The use of preset delay simplifies the design and testing of the array by utilizing properties of symmetry and fixing the center column. In this design the preset delay is 110° which allows the array to steer more than +-30deg in the H-plane.

15.2 Test results

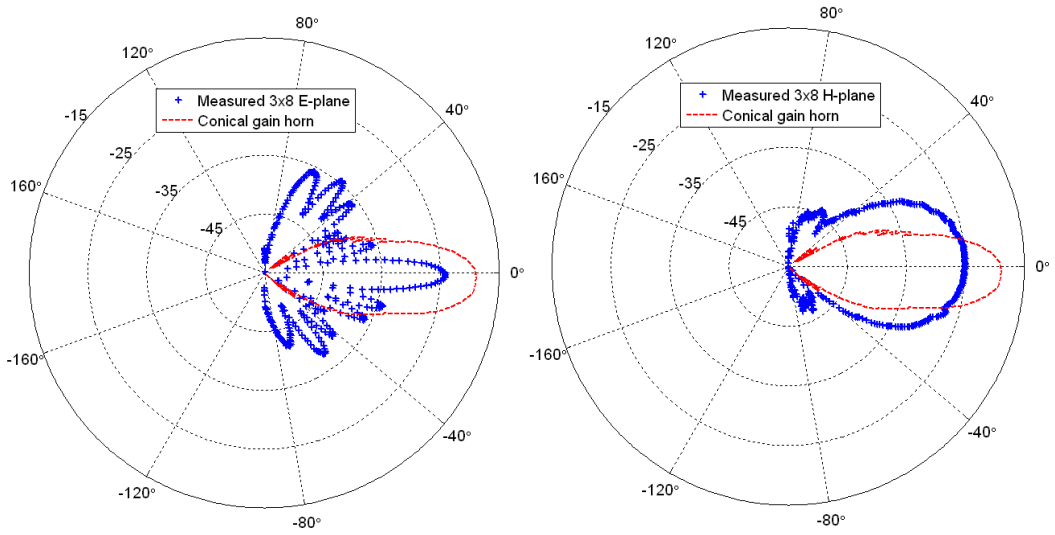

(a) **(b)**

Figure 15.2: (a) Measured E-plane radiation pattern of 3x8 array of Figure 15.1a plotted with V-band conical gain horn. (b) Measured H-plane radiation pattern of 3x8 array of Figure 15.1a plotted with V-band conical gain horn.

To assess the performance of the 60GHz array design in Figure 15.1a, the radiation pattern is measured in both E-plane and H-plane. In each case the pattern is compared with the measured pattern of a V-band conical gain horn. The expected peak gain of the fixed beam 3x8 patch array is 20dB and the expected peak gain of the V-band conical gain horn is 22dB. The observed difference in peak gain is 6dB and we expect that this is partially due to the waveguide to coax transition which was needed for the 3x8 patch array but not used in measuring the waveguide fed

conical gain horn and partially due to additional mismatch loss in the coax to microstrip transition on the 3x8 patch array.

Figure 15.3 shows the measured radiation patterns for the antenna in Figure 15.1b with 0° relative phase delay between each column. This is accomplished by applying 110° phase delay to columns 1 and 3 using the 8mm Rogers 6002 slab with a separation of $d = 0$. The radiation pattern is plotted with the simulated radiation pattern which is generated by simulating the 3x8 array in HFSS with equal phase at each of 3 column feeds.

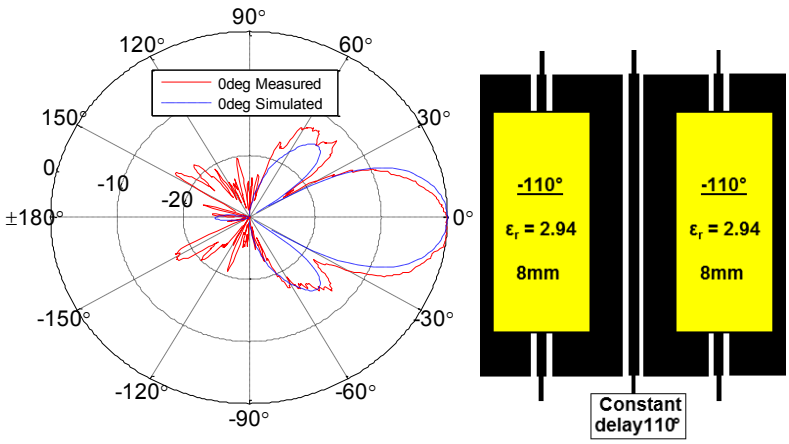

Figure 15.3: Measured radiation pattern of 3x8 array with 0° relative phase delay between each column

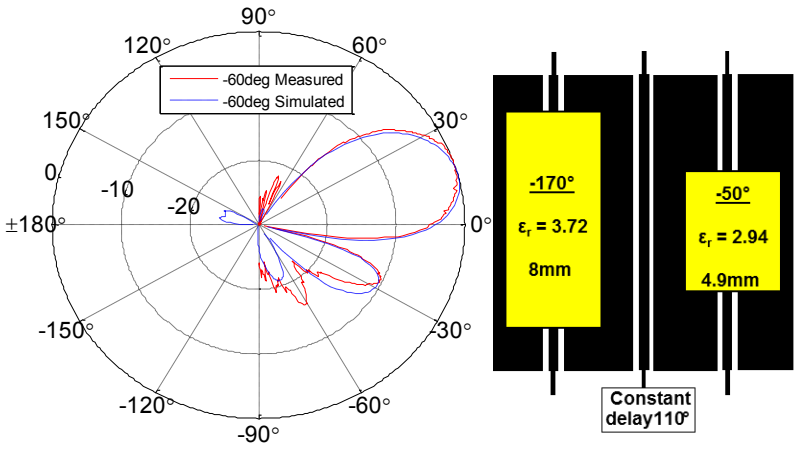

Fig. 15.4: Measured radiation pattern of 3x8 array with -60° relative phase delay between each column

Figure 15.4 shows the measured radiation patterns for the antenna in Figure 15.1b with -60° relative phase delay between each column. This is accomplished by applying 170° phase delay to column 1 using the 8mm Isola IS620 slab with a separation of $d = 0$ and applying 50° phase delay to column 3 using the 4.9mm Rogers 6002 slab with separation of $d = 100\mu m$. In practice a separation of $d = 100\mu m$is most easily achieved using a single sheet of $100\mu m$thick plastic to physically support the slab above the CPW. Although the maximum measured phase delay of the 8mm IS620 slab was 135° in the VNA measurement test we found that by applying additional force once the slab was in contact with the CPW produced additional phase delay. The value of 170° phase delay was achieved in situ by carefully varying the force of the slab on the CPW. The radiation pattern is plotted with the simulated radiation pattern which is generated by simulating the 3x8 array in HFSS with 60° uniform progressive phase delay across 3 column feeds.

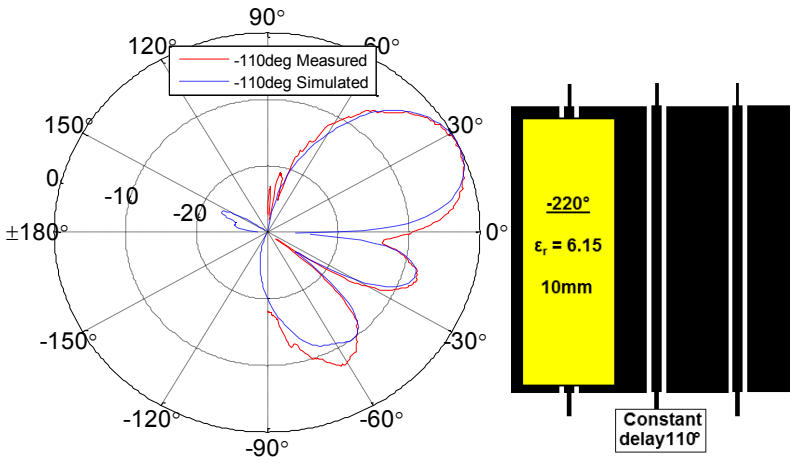

Figure 15.5: Measured radiation pattern of 3x8 array with -110° relative phase delay between each column

Figure 15.5 shows the measured radiation patterns for the antenna in Figure 15.1b with -110° relative phase delay between each column. This is accomplished by applying 220° phase delay to column 1 using the 10mm Rogers 3006 slab with a separation of $d = 0$. The radiation pattern is plotted with the simulated radiation pattern which is generated by simulating the 3x8 array in HFSS with 60° uniform progressive phase delay across 3 column feeds.

Chapter 16

Chapter 16: CONCLUSIONS AND FUTURE WORK

16.1 Project summary

A steerable antenna for use at 60GHz band was developed using a reconfigurable dielectric phase shifter and 1x8 series fed patch arrays. A mm-wave VNA system is used to measure the relative phase delay and insertion loss of various dielectric materials placed near to a section of CPW transmission line. The results suggest various lengths of dielectric materials in the range $\varepsilon_r = 3 - 6$ can provide up to 220° phase delay with less than 3dB insertion loss. An antenna was fabricated on Rogers Duroid 5880 for use with a dielectric slab phase shifting technique. Using slabs of Rogers 6002, Isola IS620, and Rogers 3006 the array is steered off axis approximately 30°.

16.2 Future of 60GHz array technology

Future work on 60GHz dielectric phase shifting for phased arrays will need to focus on increasing the field of view of the phase array and on a means to accurately and dynamically position the dielectric slabs over the CPW transmission line. Increasing the field of view likely means increasing the length of slab sections beyond the maximum tested (10mm) so that additional phase shift can be realized while minimizing insertion loss. Ideas for mechanical positioning of dielectric slabs include the use of linear actuators with high resolution stepper motors, voice-coil positioners, or piezo linear motors. To achieve the beam steering performance cited above the required resolution is in the range of microns; well above the positioning

resolution of all three technologies. The primary factors determining which positioning technology to use are cost and required positioning speed.

CONCLUSIONS

Three papers on topics in electromagnetics were presented. Part I explored a method of enabling large area phased array antennas using a wirelessly controlled and powered space-fed phased array. The WiPAA project demonstrated that an array of physically and electrically disconnected apertures can operate collectively as a phased array antenna and a wireless signal can be used to control and point a collimated beam. Prototype hardware was developed at X-Band to demonstrate various characteristics of the technology including: an electromagnetically coupled patch antenna, collocated X-Band and C-Band apertures, and a wirelessly controlled steerable space-fed 4x1 array. Part II presented a new method for estimating the temperature rise in solid object targets when illuminated by a laser beam propagated through turbulent atmosphere. A statistical model is used to determine the average intensity of a laser beam propagated through a range of turbulent environments representative of the atmospheric turbulence that exists near the ground and near the ocean's surface. A diffusion model is used to determine the temperature rise in a solid object's surface over time when illuminated by a laser light source. These two models are combined to produce an estimation of the minimum dwell time required to heat an object to its melting point given a specific set of laser parameters. Several numerical examples are given which contain parameters relevant to operators of modern day CO_2 laser systems. Part III contains the results of a study on dielectric slabs for phase shifting at 60GHz. Building on previous work by Junho Cha and others, we extend the concept of using movable dielectric slabs to selectively alter the phase of transmission lines to 60GHz, an area targeted by future high data rate wireless communications applications. We successfully demonstrated low loss phase shift using a number of different dielectric materials and concluded that in many cases a usefully large continuous range of phase values is achievable using relatively low ε_r and relatively long slab

lengths. We demonstrated a 3x8 steerable phased array antenna using the reconfigurable dielectric slab phase shifter. The results show that the beam pointing ability and relatively low loss of the technique make it an attractive alternative to integrated circuit based phasing for low cost 60GHz phased array antennas.

REFERENCES

[1] J. E. Winter and N. C. Anderson, "Distributed aperture implementation on the techsat 21 satellites," in *2003 IEEE Aerospace Conference*, Big Sky, MT, 2003.

[2] J. S. Herd and A. J. Fenn, "Design considerations for space-based radar phased arrays," in *Microwave Symposium Digest, 2005 MTT-S International*, Long Beach, CA, 2005.

[3] American Institute of Aeronautics and Astronautics, "Solar Power Satellites: An AIAA Position Paper," AIAA, Reston, VA, 1978.

[4] W. C. Brown, "Power/Energy: Solar Power Satellites: Microwaves deliver the power: Kilometer-diameter antennas would be used in super system to transmit power to ground-based rectifying antennas," *Spectrum, IEEE, vol. 16, no. 6,* pp. 36-43, June 1979.

[5] US Congress Office of Technology Assessment, "Solar Power Satellites," OTA, Washington, DC, 1981.

[6] W. C. Brown, "Rectenna Technology Program: Ultra Light 2.45 GHz Rectenna and 29 GHz Rectenna.," NASA Contractor Report 179558. Raytheon Company, Waltham, MA, 1987.

[7] University of Alaska, "PowerSat: A Technology Demonstration of a Solar Power Satellite," NASA-CR-197210, Fairbanks, AK, 1994.

[8] G. A. Landis, "Reinventing the Solar Power Satellite," Glenn Research Center, NASA/TM-2004-212743, Cleveland, OH, 2004.

[9] C. H. Hightower, S. H. Wong, A. R. Perkons and C. I. Igwe, "A Space-Fed Phased Array for Surveillance From Space," *IEEE AES Systems Magazine,* pp. 13-17, May 1991.

[10] T. Clark and E. Jaska, "Million element ISIS array," in *2010 IEEE International Symposium on Phased Array Systems and Technology*, Boston, MA, 2010.

[11] J. Guerci and E. Jaska, "ISAT- innovative space-based-radar antenna technology," in *2003 IEEE International Symposium on Phased Array Systems and Technology*, Boston, MA, 2003.

[12] R. J. Mailloux, Phased Array Antenna Handbook, Boston, MA: Artech House, 2005.

[13] A. R. Miccioli, "Antenna Array System". United States of America Patent 3,305,867, 21 Feb 1967.

[14] R. Q. Lee, Z. Popovic, S. Rondineau and F. A. Miranda, "Steerable space fed lens array for low-cost adaptive ground station applicaitons," in *2007 IEEE Antennas and Propagation*

Society International Symposium , Honolulu, HI, 2007.

[15] R. J. Mailloux, "Antenna array architecture," *Proceedings of the IEEE,* vol. 80, no. 1, pp. 163-172, 1992.

[16] D. J. Sego, "System and Methods for Radar and Communications Applications". United States of America Patent 7,782,255, 24 Aug 2010.

[17] H. Ahn, B. Tomasic and S. Liu, "Digital Beamforming in a large conformal Phased Array Antenna for satellite operations support - Architecture, design, and development," in *IEEE International Symposium on Phased Array Systems and Technology (ARRAY)*, Boston, MA, 2010.

[18] I. Chiba, Y. Konishi and T. Nishino, "Progress of phased array systems in Japan," in *IEEE International Symposium on Phased Array Systems and Technology (ARRAY)*, Boston, MA, 2010.

[19] W. Chappell and C. Fulton, "Digital Array Radar panel development," in *IEEE International Symposium on Phased Array Systems and Technology (ARRAY)*, Boston, MA, 2010.

[20] NASA: LBJ Space Center, "SP-R-002A: Vacuum Stability Requirements of Polymeric Material for Spacecraft Application," NASA, Houston, TX, 1974.

[21] Taconic, "RF-35TC datasheet," [Online]. Available: http://www.taconic-add.com/pdf/rf35tc.pdf. [Accessed 22 April 2013].

[22] Rogers Corp., "RT/duroid 6002 datasheet," 13 April 2011. [Online]. Available: http://www.rogerscorp.com/documents/609/acm/RT-duroid-6002-laminate-data-sheet.pdf. [Accessed 22 April 2013].

[23] Arlon, "CLTE-AT datasheet," 2012. [Online]. Available: http://www.arlon-med.com/CLTE-AT.pdf. [Accessed 22 April 2013].

[24] G. DeJean, R. Bairavasubramanian, D. Thompson, G. E. Ponchak, M. M. Tentzeris and J. Papapolymerou, "Liquid Crystal polymer (LCP): a new organic material for the development of multilayer dual-frequency/dual-polarization flexible antenna arrays," *IEEE Antennas and Wireless Propagation Letters,* vol. 4, pp. 22-26, 2005.

[25] D. Thompson, O. Tantot, H. Jallageas, G. E. Ponchak, M. M. Tentzeris and J. Papapolymerou, "Characterization of liquid crystal polymer (LCP) material and transmission lines on LCP substrates from 30 to 110 GHz," *IEEE Transactions on Microwave Theory and Techniques,* vol. 52, no. 4, pp. 1343-1352, 2004.

[26] Rogers, "ULTRALAM 3000 Series: Fabrication Guidelines," March 2009. [Online]. Available: http://www.rogerscorp.com/documents/822/acm/Fabrication-Guidelines-

ULTRALAM-3000-LCP-Materials.pdf. [Accessed 22 April 2013].

[27] R. Bancroft, Microstrip and Printed Antenna Design, Noble Publishing, 2004.

[28] D. M. Pozar and B. Kaufman, "Increasing the bandwidth of a microstrip antenna by proximity coupling," *Electronics Letters,* vol. 23, no. 8, pp. 368-369, 1987.

[29] S. M. Duffy, "An enhanced bandwidth design technique for electromagnetically coupled microstrip antennas," *IEEE Transactions on Antennas and Propagation,* vol. 48, no. 2, pp. 161-164, 2000.

[30] W. C. Brown, "The History of Power Transmission by Radio Waves," *IEEE Transactions on Microwave Theory and Techniques,* vol. 32, no. 9, pp. 1230-1242, 1984.

[31] J. O. McSpadden, L. Fan and K. Chang, "Design and experiments of a high-conversion-efficiency 5.8-GHz rectenna," *IEEE Transactions on Microwave Theory and Techniques,* vol. 46, no. 12, pp. 2053-2060, 1998.

[32] Y. Yoshimura, "A Microstripline Slot Antenna (Short Papers)," *IEEE Transactions on Microwave Theory and Techniques,* vol. 20, no. 11, pp. 760-762, 1972.

[33] J. F. Dickson, "On-chip high-voltage generation in MNOS integrated circuits using an improved voltage multiplier technique," *IEEE J. Solid-State Circuits,* vol. 11, pp. 374-378, 1976.

[34] Avago Technologies, "HSMS-285x Series Datasheet," 29 May 2009. [Online]. Available: www.avagotech.com/docs/AV02-1377EN. [Accessed 17 April 2013].

[35] Avago Technologies, "HSMS-286x Surface Mount Microwave Schottky Dectector Diode datasheet," 26 August 2009. [Online]. Available: www.avagotech.com/docs/AV02-1388EN. [Accessed 2013 April 17].

[36] A. P. Sample, D. J. Yeager, P. S. Powledge and J. R. Smith, "Design of passively powered, programmable platform for UHF RFID systems," in *IEEE International Conference on RFID*, Grapevine, TX, 2007.

[37] S. Ackerman, "Video: Navy Laser Sets Ship on Fire," wired.com, 8 April 2011. [Online]. Available: http://www.wired.com/dangerroom/2011/04/video-navy-laser-sets-ship-on-fire/. [Accessed 25 March 2013].

[38] L. Andrews and R. Phillips, in *Laser beam propagation through random media*, Bellingham, WA, SPIE, 2005, pp. 321-395.

[39] A. Ishimaru, in *Wave propagation and scattering in random media*, New York, NY, Academic Press, 1978, pp. 399-452.

[40] P. Sprangle, J. R. Penano and B. Hafizi, "Optimum Wavelength and Power for Efficient Laser Propagation in Various Atmospheric Environments," Report NRL/ME/6790-05-8907, Naval Research Laboratory, Washington, DC, 2005.

[41] P. Sprangle, J. R. Penano and B. Hafizi, "Propagation of intense short laser pulses in the atmosphere," *Phys. Rev. E,* vol. 66, no. 4, p. 046418, 2002.

[42] J. R. Penano, P. Sprangle, B. Hafizi, A. Ting, D. F. Gordon and C. A. Kapetanakos, "Propagation of ultra-short, intense laser pulses in air," *Phys. Plasmas,* vol. 11, no. 5, p. 2865, 2004.

[43] Z. H. Shen, S. Y. Zhang, J. Lu and X. W. Ni, "Mathematical modeling of laser induced heating and melting in solids," *Optics & Laser Technology,* vol. 33, no. 8, pp. 533-537, 2001.

[44] J. H. Betchel, "Heating of solid targets with laser pulses," *J. Appl. Phys.,* vol. 46, no. 4, pp. 1585-1593, 1975.

[45] A. M. Prokhorov, V. I. Konov, I. Ursu and I. N. Mihailescu, in *Laser heating of materials*, New York, NY, Adam Hilger/IOP, 1990, pp. 39-72.

[46] A. Ishimaru, "The Beam Wave Case and Remote Sensing," in *Laser Beam Propagation in the Atmosphere*, New York, NY, Springer-Verlag, 1978, pp. 129-170.

[47] S. F. Clifford, "The Classical Theory of Wave Propagation," in *Laser Beam Propagation in the Atmosphere*, New York, NY, Springer-Verlag, 1978, pp. 9-43.

[48] B. J. Lund, "Laser atmospheric attenuation tables for LTAS," Report AL/OE-TR-1997-0063, USAF, Armstrong Laboratory, 1997.

[49] P. A. Frederickson, K. L. Davidson, C. R. Zeisse and C. S. Bendall, "Estimating the Refractive Index Structure Parameter over the Ocean Using Bulk Methods," *J. Appl. Meteor. ,* vol. 39, no. 10, pp. 1770-1783, 2000.

[50] J. L. Walsh and P. B. Ulrich, "Thermal Blooming in the Atmosphere," in *Laser Beam Propagation in the Atmosphere* , New York, NY, Springer-Verlag, 1978, pp. 223-320.

[51] M. A. Ordal, R. J. Bell, R. W. Alexander, Jr, L. L. Long and M. R. Querry, "Optical properties of fourteen metals in the infrared and far infrared: Al, Co, Cu, Au, Fe, Pb, Mo, Ni, Pd, Pt, Ag, Ti, V, and W," *Appl. Opt. ,* vol. 24, no. 24, pp. 4493-4499, 1985.

[52] X. E. Lin, "Laser pulse heating," in *Proceedings of the 1999 Particle Accelerator Conference, Vol. 2, 1429-1431*, New York, NY, 1999.

[53] S. B. Boyden and Y. Zhang, "Temperture and wavelength-dependent spectral absorptivities of metallic materials in the infrared," *J. Thermophys. Heat Trans.,* vol. 20, no. 1, pp. 9-15,

2006.

[54] S. G. Warren and R. E. Brandt, "Optical constants of ice from the ultraviolet to the microwave: A revised compilation," *J. Geophys. Res.,* vol. 113, p. D14220, 2008.

[55] Z. M. Zhang, G. Lefever-Button and F. R. Powell, "Infrared Refractive Index and Extinction Coefficient of Polyimide Films," *International Journal of Thermophysics,* vol. 19, no. 3, pp. 905-916, 1998.

[56] R. Komanduri, "Machining of Fiber-Reinforced Composites," *Machining Science & Technology,* vol. 1, no. 1, pp. 113-152, 1997.

[57] R. Kitamura , L. Pilon and M. Jonasz, "Optical Constants of Silica Glass from Extreme Ultraviolet to Far Infrared at Near Room Temperature," *Appl. Opt. ,* vol. 46, no. 33, pp. 8118-8133, 2007.

[58] E. D. Palik and G. Ghosh, in *Handbook of optical constants of solids*, New York, NY, Academic Press, 1998, pp. 957-987.

[59] L. Tsang, J. A. Kong and K. H. Ding, in *Scattering of Electromagnetic Waves: Advanced Topics*, New York, NY, Wiley, 2001, pp. 351-353.

[60] DuPont Corporation, "Dupont Kapton Polyimide Film Datasheet," 2011. [Online]. Available: http://www2.dupont.com/Kapton/en_US/assets/downloads/pdf/HN_datasheet.pdf. [Accessed 25 March 2013].

[61] M. Sparks, "Theory of laser heating of solids: metals," *J. Appl. Phys. ,* vol. 47, no. 3, pp. 837-849, 1976.

[62] E. P. Shettle and R. W. Fenn, "Models for the Aerosols of the Lower Atmosphere and the Effects of Humidity Variations on Their Optical Properties," Report AFGL-TR-79-0214, USAF, Air Force Geophysics Laboratory, Hanscom AFB, MA, 1979.

[63] C. Reinhardt, Y. Kuga, J. Ritcey and A. Ishimaru, "Atmospheric channel transfer function estimation from experimental free-space optical communications data," *SPIE Optical Engineering,* vol. 51, no. 3, p. 031205, 2012.

[64] R. C. Daniels, J. N. Murdock, T. S. Rappaport and R. W. Heath, "60 GHz Wireless: Up Close and Personal," *IEEE Microwave Magazine,* vol. 11, no. 7, pp. 44-50, Dec. 2010.

[65] Wireless Gigabit Alliance, "WiGig White Paper: Defining the Future of Multi-Gigabit Wireless Communications," July 2010. [Online]. Available: http://wirelessgigabitalliance.org/specifications/. [Accessed 25 March 2013].

[66] J.-L. Kuo, Y.-F. Lu, T.-Y. Huang, Y.-L. Chang, Y.-K. Hsieh, P.-J. Peng, I.-C. Chang, T.-C. Tsai, K.-Y. Kao, W.-Y. Hsiung, J. Wang, Y. Hsu, K.-Y. Lin, H.-C. Lu, Y.-C. Lin, L.-H. Lu, T.-W. Huang and R.-B. Wu, "60-GHz Four-Element Phased-Array Transmit/Receive System-in-Package Using Phase Compensation Techniques in 65-nm Flip-Chip CMOS Process," *Microwave Theory and Techniques,* vol. 60, no. 3, pp. 743-756, 2010.

[67] S. Pinel, P. Sen, S. Sarkar, B. Perumana, D. Dawn, D. Yeh, F. Barale, M. Leung, E. Juntunen, P. Vadivelu, K. Chuang, P. Melet, G. Iyer and J. Laskar, "60GHz single-chip CMOS digital radios and phased array solutions for gaming and connectivity," *IEEE Journal on Selected Areas in Communication,* vol. 27, no. 8, pp. 1347-1357, 2009.

[68] E. Cohen, M. Ruberto, M. Cohen, O. Degani, S. Ravid and D. Ritter, "A CMOS bidirectional 32-element phased-array transceiver at 60GHz with LTCC antenna," in *IEEE Radio Frequency Integrated Circuits Symposium (RFIC)*, Montreal, ON, 2012.

[69] J. Cha, Y. Kuga and S. Lee, "A Steerable Array Antenna Using Movable Dielectric Slabs on a Coplanar Waveguide," *Microwave and Optical Technology Letters,* vol. 48, no. 11, pp. 2222-2227, 2006.

[70] J. Cha, Y. Kuga, A. Ishimaru and S. Lee, "A 20 GHz Steerable Array Antenna Using 3-bit Dielectric Slab Phase Shifter on a Coplanar Waveguide," *IEEE Transactions on Antennas and Propagation ,* vol. 55, no. 2, pp. 290-297, 2007.

[71] G. Y. Chen, J. S. Sun, S. Y. Huang and Y. D. Chen, "The Novel 3-Way Power Dividers/Combiners Structure and Design," in *IEEE Wireless and Microwave Technology Conference WAMICON*, Clearwater, FL, 2006.

PUBLICATIONS

[1] M. Stoneback, A. Ishimaru, C. Reinhardt, and Y. Kuga, “Temperature rise in objects due to optical focused beam through atmospheric turbulence near ground and ocean surface”, SPIE Optical Engineering; vol. 53, no. 3, March 2013 .

[2] M. A. Stoneback, M. I. Stoneback, and Y. Kuga, “Feasibility Study of a Wirelessly Controlled and Powered Space-Fed Phased Array Antenna”, submitted to IEEE AP-S, January 2013.

[3] M. Stoneback, A. Ishimaru, C. Reinhardt, and Y. Kuga , "Temperature Rise in Objects due to Optical Focused Beam Through Atmospheric Turbulence Near Ground and Ocean Surface," USNC-URSI National Radio Science Meeting, Boulder, CO, 9-12 January 2013.

[4] M.A. Stoneback, M.I. Stoneback, and Y. Kuga "Measurement and Analysis of a Wireless Phased Array Antenna Prototype," IEEE AP-S 2012, Chicago, IL. , 8-14 July 2012

[5] M. Stoneback and Y. Kuga, "Unit Cell Autonomy Via Wireless Control of a Space-Fed Phased Array Antenna," USNC-URSI National Radio Science Meeting, Boulder, CO, 4-7 January 2012.

[6] M. Stoneback, and Y. Kuga; “A Wireless Space-Fed Phased Array Antenna,” AP-S/URSI Meeting 2011, 3-8 July 2011.

[7] F. Zhang, M. Stoneback, and B. Otis; , "A 23 μA RF-powered transmitter for biomedical applications," Radio Frequency Integrated Circuits Symposium (RFIC), 2011 IEEE , vol., no., pp.1-4, 5-7 June 2011

[8] M. Stoneback. C. Wolthausen, and Y. Kuga; "A steerable 60GHz array antenna using a reconfigurable dielectric phase shifter," Antennas and Propagation Society International Symposium (APSURSI), 2010 IEEE , vol., no., pp.1-4, 11-17 July 2010.

[9] M. Stoneback, J. Cha, S. Dahlstet, and Y. Kuga; , "A mechanically steerable quasi-Yagi endfire array using dielectric phase shifters at 5.8GHz," Antennas and Propagation Society International Symposium, IEEE AP-S 2008,San Diego, CA, vol., no., pp.1-4, 5-11 July 2008.